Thesis presented to the Instituto Tecnológico de Aeronáutica, in partial fulfillment of the requirements for the degree of Doctor of Science in the Program of Aeronautical and Mechanical Engineering, field of Materials, Manufacturing and Automation.

Barbara Souza Damasceno

FABRICATION OF GRAPHENE ENHANCED GaN FOR SURFACE ACOUSTIC WAVES SENSOR APPLICATIONS

Prof. Dr. Douglas Marcel Gonçalves Leite
Advisor

Prof. Dr. André Luis de Jesus Pereira
Co-Advisor

Campo Montenegro
São José dos Campos, SP – Brazil
2024

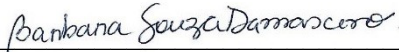## BIBLIOFRAPHIC REFERENCE

DAMASCENO, Barbara Souza. **Fabrication of Graphene Enhanced GaN for Surface Acoustic Waves Sensor Applications**. 2024. 110f. Thesis of Doctor of Science in Aeronautical and Mechanical Engineering – Instituto Tecnológico de Aeronáutica, São José dos Campos.

CESSION OF RIGHTS

FABRICATION OF GRAPHENE ENHANCED GaN FOR SURFACE ACOUSTIC WAVES SENSOR APPLICATIONS

Barbara Souza Damasceno

Thesis Commitee Composition:

Prof. Dr.	Gilberto Petraconi Filho	Chairperson	-	ITA
Prof. Dr.	Douglas Marcel Gonçalves Leite	Advisor	-	ITA
Prof. Dr.	André Luis de Jesus Pereira	Co-advisor	-	ITA
Prof. Dr.	Elizabete Yoshie Kawachi	Internal	-	ITA
Prof. Dr.	Severino Alves Júnior	External	-	UFPE
Prof. Dr.	Wagner Souza Machado	External	-	UFSJ

ITA

I dedicate this work to my support network, including family, friends, and professors for their consistent support and guidance throughout my academic and professional endeavors.

Acknowledgements

I am deeply grateful to my family for their prompt support and everything they have done for me. I thank my nephews for the laughter and hugs that have a special way of making everything better. To Joao, I express my heartfelt gratitude for his constant support and the cheerful hours of distraction he brings into my life.

To Isa, Rah, Gabi, and Vanessa, I extend my sincere thanks for their companionship, enduring friendship, and the countless hours of shared laughter and distraction. To Sibs, I am thankful for her consistent kindness and presence whenever I needed it. To my friends from UFRPE/UACSA, thank you!

I am thankful to my collaborators, including Prof. Gustavo, Prof. Ariana, Joao, and Palomino, for their contributions to our collaborative work on sensor development at USP. I am thankful to Prof. Evelyn for her assistance with synthesis in the lab at ITA.

I want to express my gratitude to Prof. James Tour, Mr. Dustin, Lucas, Will, Jaeho, Kevin, Jacob, Alex, and Rodrigo for the shared moments and guidance at Rice University. To Jing, Tim, and Carlos from the Shared Equipment Authority at Rice University, I extend my thanks for their training in lithography and cleanroom procedures. I am grateful to Marco, Beatriz, and all the Fulbright Scholars who provided happy moments during my time pursuing my Doctorate sandwich program in the USA.

My gratitude extends to Prof. Bacher, Mr. Tilmar, Laura, Yannick, Lonnie, Tobi, and Henrik for warmly welcoming me to Germany, providing support during my adaptation period, and for the friendship we share beyond the lab.

I deeply appreciate the partnerships with my lab colleagues and everyone who has crossed my path, supporting me throughout my academic journey.

To my professors, Douglas, Argemiro, Gilmar, and André, I am grateful for their guidance, patience, and belief in my abilities. I want to acknowledge my former mentor Ana Claudia for her mentorship, friendship, and attention to detail.

I am thankful to CAPES, CNPq, and Fulbright Brazil for funding my research endeavors.

Lastly, I express my deepest gratitude to João Pedro, my first friend at ITA, in memory.

"All sorts of things can happen when you're open to new ideas and playing around with things."

(Stephanie Kwolek)

Abstract

This thesis aims to enable the development of a heterostructure composed of gallium nitride (GaN) thin films and carbon black-derived flash graphene (CBFG) and/or poly(o-methoxyaniline) (POMA), with the intention of utilizing it in sensing applications. This work includes the deposition of GaN thin films through sputtering on Si(100) and glass substrates, the synthesis of CBFG and POMA powders via flash Joule heating (FJH) system and oxidative polymerization, respectively, and the fabrication and optimization of an ink containing CBFG, POMA, or both. In surface acoustic wave (SAW) devices, GaN film can be used as the piezoelectric substrate, and the ink can be applied as the sensing layer in the sensor's active area. The results showed successful deposition of GaN films on Si and glass by sputtering. X-ray diffraction (XRD), Raman spectroscopy measurements, and transmission electron microscopy (TEM) image confirmed that the GaN films are polycrystalline and exhibit wurtzite crystal structure with preferential orientation in the c-direction. The values of H/λ (thickness/wavelength) obtained using the thickness measured by scanning electron microscopy (SEM) (2h $\rightarrow$ H = 329 $\pm$ 17 nm, λ = 1000 nm $\rightarrow$ H/λ = 0.33 | 4h $\rightarrow$ H = 569 $\pm$ 30 nm, λ = 1000 nm $\rightarrow$ H/λ = 0.57 | 6h $\rightarrow$ H = 1162 $\pm$ 36 nm, λ = 1000 nm $\rightarrow$ H/λ = 1.16) showed that the GaN sample grown for 6 hours, even though exhibiting a high root mean square (RMS) roughness measured by atomic force microscopy (AFM), should still demonstrate the best performance in SAW applications. An ohmic contact between the interdigitated transducers (IDTs) and GaN film was observed, which is beneficial for SAW device applications. SAW devices were produced and optimized using the deposited GaN on Si films. Pure turbostratic CBFG was successfully synthesized using the FJH system, as confirmed by XRD, SEM, and TEM images. Porosimetry analysis showed CBFG's surface area around 293 m² g⁻¹. As a result, CBFG proved to be a promising adsorbent for methylene blue (MB) removal, which is an intriguing property for enhancing the sensitivity of the device. POMA was successfully synthesized through oxidative polymerization, as supported by XRD and XPS results. Fourier transform infrared spectroscopy (FTIR) data showed amine and imine units on the polymer chain of POMA, consistent with XPS analysis. SEM images depicted material with a globular morphology, while the porosimetry presented a surface area around 4 m² g⁻¹. Despite its low surface area in comparison to CBFG, POMA remains a potential material for composing a conductive ink due to its chemical surface, and dispersibility, facilitating the ink production process and retaining the electron

conductivity (EC) properties. CBFG and POMA powders were combined in various ratios to form an ink with suitable EC. The highest EC value of 0.768 S m^{-1} was achieved using concentrations of 40.0 mg L^{-1} CBFG, 2.0 mg L^{-1} POMA, and 4.0 mg L^{-1} binder. This result suggests that the ink can be effectively utilized as a sensing layer in the active area of a SAW device.

List of Figures

List of Tables

List of Symbols and Abbreviations

PoC	Point-of-care
SAW	Surface acoustic wave
k^2	Electromechanical coupling coefficient
$LiTaO_3$	Lithium tantalite
GaN	Gallium nitride
GR	Graphene
IDT	Interdigitated transducers
POMA	Poly(o-methoxyaniline)
PANI	Polyaniline
MBE	Molecular beam epitaxy
MOVPE	Metalorganic vapor phase epitaxy
2D	Two-dimensional
FJH	Flash Joule Heating
CBFG	Carbon black-derived flash graphene
XRD	X-ray diffraction
SEM	Scanning electron microscopy
AFM	Atomic force microscopy
TEM	Transmission electron microscopy
XPS	X-ray photoelectron spectroscopy
FTIR	Fourier transform infrared spectroscopy
UV	Ultraviolet
CMOS	Complementary metal-oxide-semiconductor
RF	Radio frequency
f_0	Resonant frequency
v_{SAW}	Velocity of the SAW
λ	Periodicity of the IDT
PVDF	Polyvinylidene fluoride
DMMP	Dimethyl methylphosphonate
S_{11}	Reflection coefficient
S_{21}	Transmission coefficient
VNA	Vector network analyzer
S_m	Mass loading sensitivity

Δf	Difference between resonant frequency and the experimental frequency
f	Experimental frequency
k	Geometric factor
Δm	Mass change per area
GO	Graphene oxide
RH	Relative humidity
LOD	Limit of detection
RT	Room temperature
a, c	Lattice parameters
MOCVD	Metal organic chemical vapor deposition
RMS	Root Mean Square
FWHM	Full width at half maximum
TCF	Temperature coefficient of frequency
AlN	Aluminum nitride
AlGaN	Aluminum gallium nitride
SMR	Solidly mounted resonators
CVD	Chemical vapor deposition
3DAG	3D architecture graphene
PVA	Polyvinyl alcohol
GQD	Graphene quantum dot
ZnO	Zinc oxide
NW	Nanowire
NPs	Nanoparticles
I_A	Acoustoelectric current
GFET	Graphene field-effect transistor
GSAW	Graphene surface acoustic wave
SLG	Single layer graphene
EBE	Electron-beam evaporation
PPy	Polypyrrole
EC	Electrical conductivity
PI	Polyimide
PMMA	Polymethyl methacrylate
PVD	Physical vapor deposition

IPA	Isopropyl Alcohol
UHV	Ultra-high vacuum
FIB	Focused ion beam
Sku	Relative sharpness of morphology
PR	Photoresist S1818
I–V	Current-Voltage
D	Crystallite size
H/λ	Film-thickness-to-wavelength ratio
FFT	Fast Fourier transform
R	Resistance
A	Area
L	Length
ADF-STEM	Annular dark field scanning transmission electron microscope
BET	Brunauer−Emmett−Teller
MB	Methylene blue
X_1	CBFG concentration
X_2	POMA concentration
X_3	Binder concentration
ANOVA	Analysis of variance
CCD	Central composite design
EBL	Electron beam lithography
MEMS	Microelectromechanical systems
MIBK	Methyl isobutyl ketone
PCB	Printed circuit board
SMA	SubMiniature version A
CCW	Conventional coplanar waveguide

Summary

THESIS STRUCTURE FLOWCHART

CHAPTER 01
- ❖ Problem definition
- ❖ Motivation
- ❖ Objectives

CHAPTER 02

Literature Review

- ❖ Surface Acoustic Wave device
- ❖ Gallium Nitride thin films
- ❖ Graphene powder
- ❖ Poly(o-methoxyaniline) powder

Graphical abstract
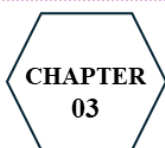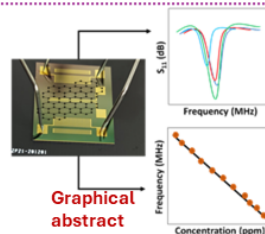
CHAPTER 03

GaN films by sputtering

- ❖ Materials
- ❖ Cleaning and deposition
- ❖ Characterization
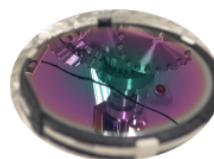
CHAPTER 04

Graphene by Flash Joule Heating

- ❖ Materials
- ❖ Synthesis
- ❖ Characterization
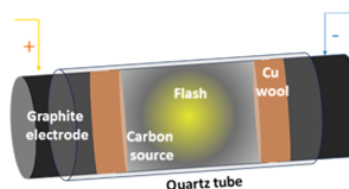
CHAPTER 05

Poly(o-methoxyaniline) by oxidative polymerization

- ❖ Materials
- ❖ Synthesis
- ❖ Characterization
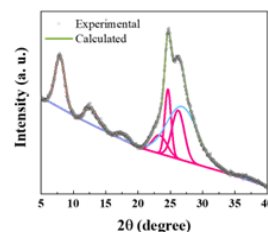
CHAPTER 06

Fabrication of a conductive ink composed of graphene, POMA, or their combination.

- ❖ Materials
- ❖ Production
- ❖ Optimization

Graphical abstract
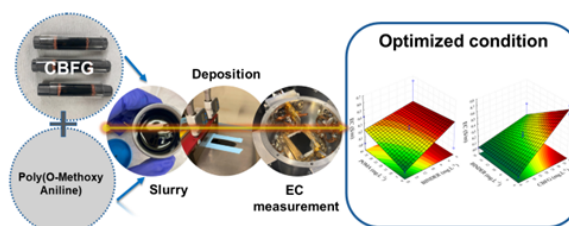
CHAPTER 07

SAW devices

- ❖ SAW sensor production
- ❖ Optimization
- ❖ PCB assemble
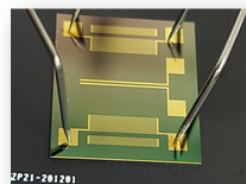
CHAPTER 08
- ❖ Conclusion
- ❖ Perspective

CHAPTER 1.Introduction

1.1   Problem definition

Nanomaterials have been utilized to improve conventional sensor technologies, enabling the miniaturization of devices for various applications such as gas leak detection and disease diagnostics [1–34,5]. However, there is a need for the development of swift and accurate sensors that can be used at point-of-care (PoC) [6,7]. These instruments should provide real-time population assessments for quick and accurate political and social decisions on matters requiring an immediate response.

Despite various sensing technologies being reported in the literature [2], many of them are not available in the market due to complex manufacturing processes, high maintenance costs, and difficult operational setups [2,7]. Some of the available sensors also face issues such as long data analysis, noise problems, high commercial costs, and low sensitivity [2,7,8]. The use of smart sensors, such as surface acoustic wave (SAW) transducers, is necessary to overcome these drawbacks. These smart sensors use electronic acquisition data or wireless signals to process and transfer information, and their working principle can solve some of the issues associated with sensing platforms [9] [10].

SAW devices have high potential for large-scale production due to their low cost compared to conventional platforms. They can be produced using standard nanolithography processes, allowing for the fabrication of portable, inexpensive, and compact devices with remarkable characteristics for diagnostic tests [11,12]. SAW devices have many applications related to the detection of various gases (ammonia, hydrogen) and viral infections (Ebola, COVID-19), making them the leading portable sensors in PoC forms [13–16]. They have practically 100% sensitivity and 100% specificity, use low volumes of sample (6 μL), and present simple processing and short response times (< 60 s) [13,15–19]. They can also be easily produced in reduced sizes and with unit values < 1.50 USD for each disposable component [20]. Their surface can be modified through a chemical interface coating to improve selectivity and sensing of specific reactions [13,15–19] [21–23].

The working principle of SAW devices is fundamentally based on the reverse piezoelectric phenomenon, which the application of an external electrical field is converted into mechanical waves (acoustic waves) through the alternating polarity of the electrodes, and then converted back to electrical signal [23,24]. The piezoelectric surface of the SAW device allows the occurrence of electromechanical coupling where an electrical response is observed with mechanical distress and contrarywise. The piezoelectric coupling coefficient factor or the

electromechanical coupling coefficient (k^2), is a factor that measures the effectiveness of converting mechanical energy to electrical energy and vice versa, and it considers the crystallographic properties of a piezoelectric material such as orientation and symmetry [25,26]. By this, materials with large electromechanical coupling are needed. Quartz and lithium tantalite ($LiTaO_3$) are commonly used for manufacture SAW devices because they present piezoelectric properties and excellent k^2 [19]. However, they can show rough surface, operating frequency < 2 GHz and low sound speed velocity (3000-3500 m/s) [12,27]. In contrast, gallium nitride (GaN) has shown k^2 and sound speed about 4.3% and 3700 m/s, respectively [12,28,29].

GaN is an excellent material as piezoelectric base for SAW device applications due to its unique material properties. GaN has a wide bandgap, which means that it requires a high energy input to excite electrons from the valence band to the conduction band [30,31]. This property enables GaN to operate at high voltages and high temperatures, making it suitable for high-power and high-frequency applications [12,32]. Additionally, GaN has high mechanical stability, which makes it resistant to mechanical stress and deformation [33,34]. This stability enables GaN devices to maintain their performance over a wide range of operating conditions. Finally, GaN has high electron mobility, which means that electrons can move rapidly through the material, allowing fast switching speeds and high-frequency operation [12,35]. These properties make GaN an ideal material for high-frequency applications such as SAW devices [33,36].

Graphene (GR)-based nanomaterials are often used as coating layers in the production of SAW sensors, due to their high sensitivity to surface perturbations [10,37]. GR can also be labeled to detect specific targets, and the interdigitated transducers (IDT) transforms the reaction response into a measurable output signal, which is essential for creating highly selective devices [10,20,38]. GR typically exhibits properties that are suitable for SAW device applications, such as high electrical conductivity, chemical stability, and ease of functionalization.

Conjugated polymers present π-π interactions between conjugated groups along the polymer molecular chain that can provide feasible structural control and functionality for use in organic electronics. Poly(o-methoxyaniline) (POMA), a derivative of polyaniline (PANI), is a type of conjugated polymer that contains a methoxy (– OCH_3) group in the aromatic ring in the ortho-position to the amino group. The presence of the electron donor –OCH_3 substituent increases POMA's processability and solubility in organic solvents while maintaining similar electronic properties compared to PANI. Due to its low production cost, environmental safety,

good thermal stability, and robust biocompatibility, POMA has been widely studied for its applications in electronic, photovoltaic, and in sensors devices [39–42].

Both GR and POMA are potential candidates for being used as sensing layers in the SAW devices. The union of these materials in SAW devices as a sensitive layer can improve the surface chemistry, selectivity, and sensitivity of SAW devices, while GaN can be used as a stable substrate for IDTs and provides high electron mobility and fast response times. Then, jointly they can promote electrical conductivity, selective and sensitive effect on their surface [10,35,38].

This proposal aims to address the hypothesis regarding the feasibility of developing an organic sensing layer (GR and/or POMA ink)/GaN heterostructure for use in swift, user-friendly sensors that offer high sensitivity and selectivity. [19,38,43].

1.2   Motivation

SAW sensing devices are based on the generation, interconversion, and detection of electromechanical waves by IDTs on the surface of a piezoelectric crystal [9]. The wave propagation characteristics are modulated by the wave interaction with physical or chemical changes on the wave path that are measured in terms of frequency, phase, and loss of insertion of the electrical signal [10]. The active area of SAW devices must receive appropriate functionalization to enable recognition events shifting the frequency of the SAW signal [19].

GaN is a direct band gap (3.4 eV) semiconductor with piezoelectric properties that presents high electronic mobility and thermal stability [44]. These features assure the application of GaN in high-frequency (above 5 GHz) sensors [45]. The leading technologies to produce high-quality GaN films are molecular beam epitaxy (MBE) and metalorganic vapor phase epitaxy (MOVPE) techniques. However, they are expensive, demand huge investment and require extreme process conditions [46]. In contrast, the growth of GaN by reactive sputtering [47,48] is simple and relatively low-cost. In addition, micro or nanocrystalline GaN acquired from sputtering holds great potential for application in manufacturing SAW devices [49,50].

GR is a two-dimensional (2D) material of sp^2 hybridized carbon atoms packed in a honeycomb structure and it has shown promise for sensing device and electronic applications [51,52]. This is due to its large theoretical specific surface area of $2630 \ m^2g^{-1}$, high intrinsic mobility $\sim 200,000 \ cm^2 \ v^{-1}s^{-1}$, optical transmittance $\sim 97.7\%$, high electrical conductivity, and functionalization possibilities [51,52]. Additionally. GR can be chemically functionalized to detect specific targets [10,43,53]. Furthermore, GR is very suitable for SAW sensors since the IDT

transforms a mass loading or chemical reaction occurring in the GR's surface into a measurable output signal, necessary to highly manufacture selectivity devices [10,20,38]. There are different approaches to synthesize GR, such as mechanical exfoliation, chemical routes, and thermal and plasma processes [51]. However, to obtain a large sheet of GR, the synthesis techniques usually require high growth temperatures (> 1000 ºC), catalytic substrates, or a transfer process to the target substrate via corrosive solution, and others [51,53–56]. The Flash Joule Heating (FJH) system is a method to obtain carbon black-derived flash graphene (CBFG) on a large scale. This process involves passing a high current through a conductor material for a very short period (in the order of microseconds) to rapidly heat the conductor. For that, any carbon feedstock can be used to prepare CBFG and no solvent is required.

The oxidative polymerization of o-anisidine monomers to produce POMA typically involves the use of an oxidizing agent such as ammonium persulfate $((NH_4)_2S_2O_8)$ and a dopant like hydrochloric acid (HCl). This process generates cation radical sites in the monomer molecule, which serve as initiation points for polymer growth [57]. POMA is soluble in common organic solvents, has a dark greenish-blue color, and has a high degree of conjugation, leading to good electrical conductivity. This happens because conjugation that refers to the alternating single and multiple bonds between atoms in a molecule, typically involving π orbitals plays a crucial role in determining polymers electrical conductivity, including increased delocalization of electrons, lower energy barriers, charge carrier mobility, and doping effects [39,57]. POMA finds application in various fields such as electronic and optoelectronic devices, sensors, and batteries, and it is expected to show satisfactory electrical conductivity and to improve the responses in SAW devices.

Therefore, the combination of nanomaterials with polymeric materials has given rise to a new class of multifunctional materials known as polymer nanocomposites. These materials have significantly enhanced sensor performance across various fields. The utilization of GaN, CBFG, POMA, and their combinations, synthesized through proposed methods, in SAW devices represents a novel approach with potential advantages in large-scale microfabrication and cost reduction for these devices [19,38,43].

1.3 Objectives

1.3.1. General objective

Investigate the feasibility of developing an organic sensing layer (CBFG and/or POMA ink)/GaN heterostructure to be applied in efficient, user-friendly sensors with high sensitivity and selectivity.

1.3.2. Specific objectives

i) Grow and study the properties of GaN films on Si and glass substrates using reactive sputtering.

ii) Synthesize and study the properties of POMA using o oxidative polymerization.

iii) Synthesize and study the properties of CBFG using FJH system.

iv) Fabricate, deposit, and study the electrical properties of an ink containing CBFG, POMA, and their hybrids.

v) Characterize the synthesized materials using X-ray diffraction (XRD), Raman spectroscopy, scanning electron microscopy (SEM), atomic force microscopy (AFM), transmission electron microscopy (TEM), X-ray photoelectron spectroscopy (XPS), porosimetry, and Fourier transform infrared spectroscopy (FTIR).

vi) Manufacture and optimize SAW devices using GaN/Si and GaN/glass as piezoelectric material.

It is important to mention that steps (i), (ii), and (v) were conducted at the Plasmas and Processes Laboratory (LPP) of the Technological Institute of Aeronautics (ITA), Brazil. Steps (iii) to (vi) were carried out at Rice University, Texas.

CHAPTER 2.Literature review

This chapter approaches the fundamental topics about the materials necessary to understand the results of this work. As the main proposal of this project is to produce, characterize and optimize the properties of an heterostructure comprised of GaN, CBFG, POMA, for application in SAW sensors, this chapter trails the following order: surface acoustic waves devices, gallium nitride semiconductors, graphene, and poly(o-methoxyaniline).

The subheadings "2.1. Surface acoustic waves" and "2.3. Graphene" are part of a review article entitled "Recent improvements on surface acoustic wave sensors based on graphenic nanomaterials" published in the Materials Science in Semiconductor Processing (Impact Factor (2023) – 4.1)[58]. As per Elsevier subscription guidelines, authors maintain the privilege of incorporating the article into a thesis, as long as it remains unpublished for commercial purposes.

2.1. Surface acoustic waves devices

SAWs were first described by Lord Rayleigh in 1885 as mechanical waves that occur on the surface of a material, with a small penetration depth of approximately one wavelength [59].

Initially used for electronic applications, SAW sensors have diverse capabilities and are used in various fields such as structural health monitoring, temperature and pressure sensing, ultraviolet (UV) sensing, biological sensing, chemical sensing, gas sensing, and sensing of liquids [23,26]. SAW devices consist of interdigital transducers positioned over a piezoelectric substrate, and changes in stimuli such as radiation, temperature, pressure, mass, or conductivity on the surface of the device can be detected due to the acoustic wave undergoes disturbances in velocity that lead to phase changes and delay. This enables the SAW device to function as a sensor [60,61].

The use of SAW sensors is crucial for many applications in terms of reducing costs, size, and weight [52]. By integrating or attaching the antenna to a piezoelectric structure, it is possible to utilize the correlation between the resonance frequency of the antenna and the amount of strain applied to measure stress/strain. Strain causes modifications to the geometry and current distribution of the antenna, resulting in a shift in its resonant frequency. Thus, an antenna can be used as a practical alternative for wireless strain sensing. Some SAW sensors are wireless and do not require batteries for operation, which is a significant advantage. This reduces costs associated with wiring, decreases weight, eliminates the need for designs to install

and maintain wires, and allows the use of passive sensors as PoC devices and in harsh environments where wires and batteries would not be viable. **Figure 1** shows how sensor technologies can be improved by using nanomaterials for SAW device applications, and their utilities as PoC devices.
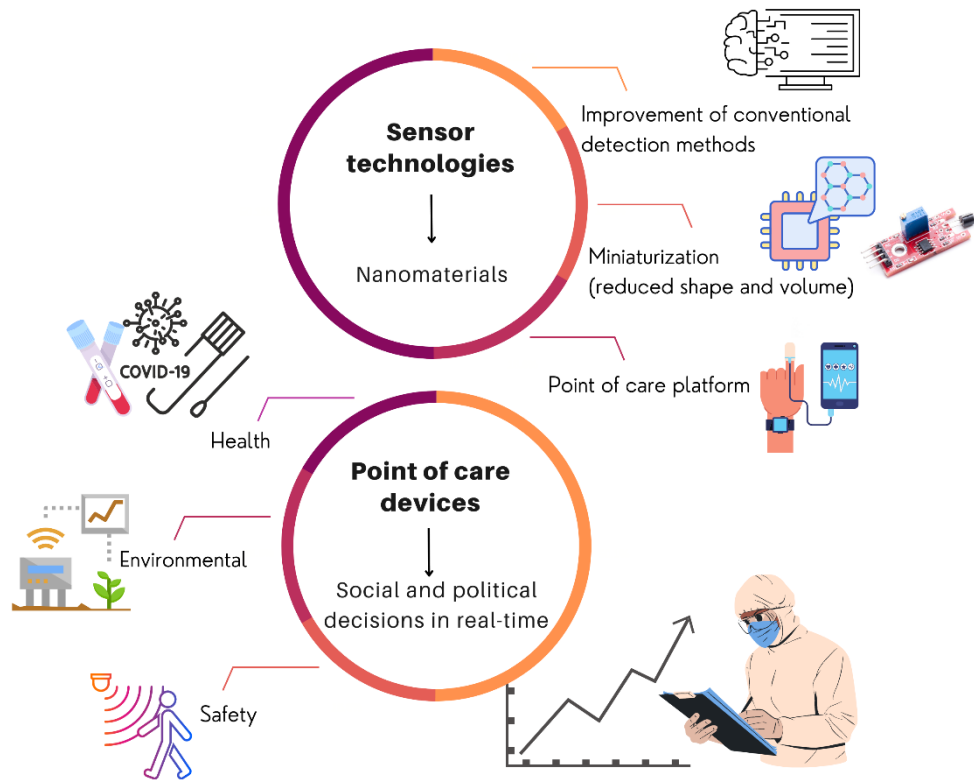
Figure 1: Schematic representation of the advancement and applications of sensor technologies using nanomaterials.

SAW devices are commonly used in applications that require high sensitivity and reliability. The sensitivity of a sensing device to a disturbance increases quadratically with the operating frequency [62]. One way to increase this resonant frequency is to use a piezoelectric substrate with a high acoustic velocity and electron mobility [52,63]. GaN thin films on SiC substrates have achieved frequencies above 14 GHz [63,64].

A SAW sensor is formed by a piezoelectric crystal (substrate) coupled with interdigital transducers that can convert electrical signal to SAW and vice versa in a configuration known as a delay line, with or without resonators (**Figure 2**) [23,65]. This IDT allows for the integration of SAW sensors with complementary metal-oxide-semiconductor (CMOS) technology and was first demonstrated by White and Voltmer in 1965 [66,67].
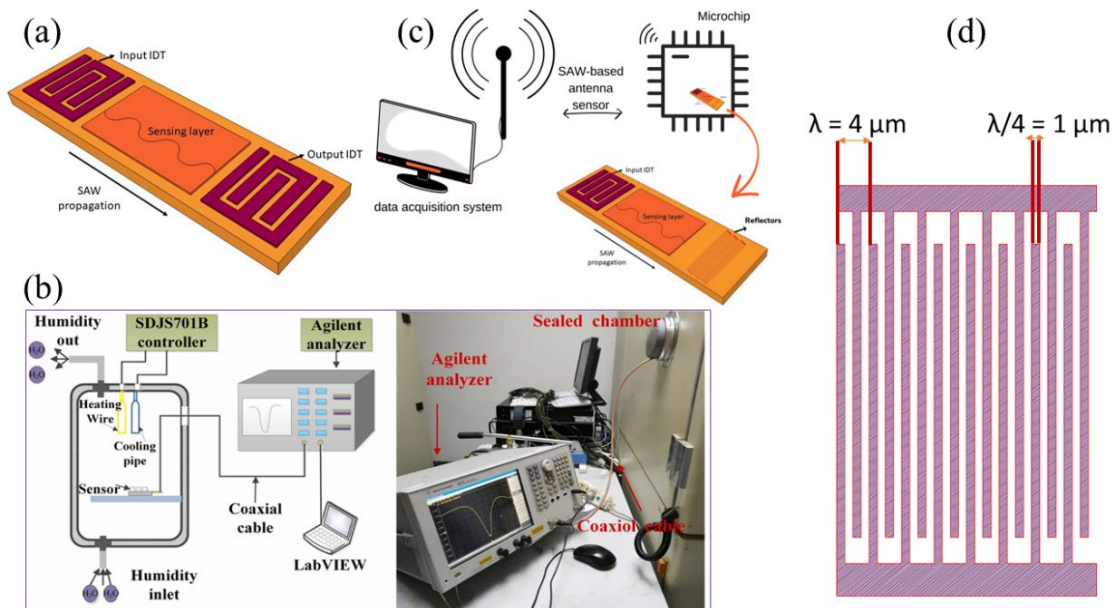
Figure 2: Basic representation of (a) a SAW sensor in delay line configuration and (b) its mechanism of working with cable connections. Adapted with permission [68]. Copyright 2022, Elsevier. (c) Schematic uses of the passive wireless SAW-based antenna system, and (d) IDT patterns illustration.

The IDT is a finger-like metal structure patterned on the piezoelectric substrate. In a delay line configuration, two IDTs are patterned on each side of the piezoelectric crystal: the input IDT, which converts the input electrical signal to SAW, and the output IDT, which converts SAW back to an electrical signal [69]. The application of an electrical current to the input IDT produces an acoustic wave through the alternating polarity of the electrodes, resulting in periodic compression and expansion of the piezoelectric material. Then, the output IDT detects the acoustic wave and converts it back into an electrical signal using the reverse mechanism [23,70–74]. The acoustic wave propagates on the substrate between the IDTs (the sensing layer), as shown in **Figure 2.**

The delay line layout is the most popular SAW device configuration because it can be coated with a wave-guiding layer of choice, reducing insertion loss, and offering a wider frequency of operation with variable bandwidths. This layout is often found to be simple and practical for many sensing applications due to its advantages. However, this configuration still comprises antennas that are not integrated with the SAW device and require cable connections to function, significantly increasing system cost and complexity (**Figure 2b**) [23,70–75]. To avoid damage vulnerability due to external interconnections, a radio frequency (RF) identification

antenna (**Figure 2c**) can be integrally incorporated and directly produced on the device for both the reception and transmission of electromagnetic waves. This results in a strain-sensing passive device with no requirements for external interconnects [23,68,70–75].

The SAW device operates at a resonant frequency that is dependent on the IDT design, also called the central frequency. This dependence is given by the fact that the efficient excitation of the elastic wave occurs when the resonant frequency (f_0) is equal to the phase velocity of the wave (v_{SAW}) divided by the periodicity of the IDT (λ), according to **Equation (1)**.

$$f_0 = \frac{v_{saw}}{\lambda} \tag{1}$$

In this case, the periodicity is equal to the pitch of the IDT (i.e., width and the gap between two electrodes equal to $\lambda/4$), as shown in **Figure 2**. Because of this, both the speed at which sound travels through the material and the maximum resolution achievable for fabricating electrodes using lithography impose constraints on the device's operating range. For example, considering GaN thin film as the piezoelectric layer of the SAW device (v_{GaN} = 3700 m s^{-1}) and λ = 2 µm, theoretically, the resonant frequency would be 1.85 GHz [28,65].

The resonant frequency change is due to the mass or strain applied on a delay-line surface, which perturbs the SAW propagation and is distinguishable at output IDTs. Xu et al. studied a quartz SAW sensor with a GR/polyvinylidene fluoride (PVDF) active layer for gas detection. The frequency shift is mainly due to the adsorption of molecules on the sensing layer, in which, after increasing the dimethyl methylphosphonate (DMMP) concentration, the frequency rapidly shifts to negative values [22]. Boldeiu et al. explored the piezoelectric GaN layer on SiC to study the temperature sensing capability of the SAW sensor. They observed that the increment in temperature shifts the resonance frequency of the structure to lower values due to the expansion of the GaN structure [76].

The key characteristics of SAW devices are obtained by measuring the transfer functions, such as the reflection coefficient (S_{11}) and transmission coefficient (S_{21}), using a vector network analyzer (VNA).

The most used and easily interpreted method of sensing mass changes at the surface of a sensor is through alterations in wave velocity or oscillation frequency. By loading or unloading mass, the wave velocity is perturbed, leading to frequency shifts [24,68]. Changes in surface mass can result from either sorptive interactions or chemical reactions between the analyte and the sensing layer. This sensing approach can be applied in both liquid and gas

phases. A linear relationship is expected between mass-loading and frequency shift [24,68]. In this way, the sensitivity of mass loading on the SAW surface can be described by the proportional shift in oscillation frequency, in accordance with **Equation (2)**.

$$\Delta f_m = 2kS_m\Delta m_A \qquad\qquad (2)$$

where S_m is the mass loading sensitivity, Δf is the difference between f_0 and the experimental frequency (f), k is a geometric factor for the active area or a complex function for some random coating geometry, and Δm is the mass change per area on the active area.

The higher the sensitivity, the better the sensor can distinguish what is being analyzed, such as analyte concentration. Sensitivity can be described as the sensor's response (output signal) per target concentration (change in the concentration or mass of the analyte), and it is obtained by the slope of the calibration curve (response vs concentration curve) [24,68]. Li et al. [68] studied a sensor based on graphene oxide (GO) film with and without a molybdenum disulfide (MoS_2) sensing layer for relative humidity (RH) detection. They found that the sensitivity of the sensor with the MoS_2/GO film was significantly better than the sensor without the sensing layer, with a sensitivity of 114 ppm %RH^{-1} in the low humidity range and a sensitivity of 766.8 ppm %RH^{-1} at high humidity levels.

The limit of detection (LOD) is the minimum concentration or quantity of analyte that can be detected with statistical confidence [24,29,68]. Selectivity refers to a sensor's ability to differentiate the analyte of interest from potential interferences [24,68]. Response time and recovery time are measures of how quickly a sensor can react and recover [24,68,77]. Stability is evaluated by considering short- and long-term effects, noise, and drift. A dual-device setup with the same coating may correct some long- and short-term drift effects as long as both devices' drifts are similar, and the reference device is separate from the analyte [24,68].

2.2.   Gallium nitride semiconductor

Many semiconductors of groups III-nitrides family have been extensively studied because of their wide and direct bandgap, high thermal conductivity, and high electron saturation rate [78]. These remarkable characteristics led them to be used in high-frequency electronic devices, visible and UV light-emitting diodes, laser diodes, and optoelectronic devices.

As part of this group, GaN is a direct gap semiconductor around 3.4 eV at room temperature (RT) [78,79]. GaN crystal structures can be hexagonal (wurtzite) or cubic (zincblende).

Wurtzite GaN structure is more stable than the zincblende GaN, and it will be the focus on this work.

The wurtzite unit cell has two lattice parameters a and c with their values of 3.189 Å and 5.185 Å, respectively. Its outermost layer is composed of gallium (Ga) with three (3) bonds with underlying nitrogen (N) atoms. This formation is only possible because Ga is a soft metal in the III-A group of the periodic table which means it has three (3) free electrons in valence shell whereas N is a group V non-metal element that has five (5) electrons in valence shell. Thus, they covalently bond and form the GaN semiconductor.

GaN exhibits high chemical and thermal stability, high melting point, high breakdown voltage, high electron mobility, and piezoelectricity [78]. These properties led GaN-based materials feasible to compose diverse devices, such as high electron mobility transistors, laser diodes, photovoltaic cells, and RF modules and amplifiers [78]. Additionally, GaN-based devices have shown excellent and reliable performance even under harsh conditions.

The piezoelectric properties of GaN combined with a high resistivity as well as a high bulk and surface crystallinity, make this semiconductor also very interesting for applications involving the SAW devices. SAW sensors show the output signal in the form of RF signal allowing for remote wireless operation. The advantage of using GaN for the SAW oscillator is related to the wide band gap of this material, which allows one to implement remote UV sensors capable of performing at elevated temperatures and harsh environments. In this context, several studies of SAW propagation in GaN-based structures have been performed.

In 2001, Lee et al. [80] produced Zn-, Mg-doped, and undoped GaN films with three thicknesses (0.5, 1.3, and 2.0 µm) onto (0001)-oriented sapphire by metal organic chemical vapor deposition (MOCVD). For that, the substrate was heated above 1000 ºC for cleaning, cooled to 500 ºC to the deposition of amorphous-like GaN as a buffer layer and heated again to 1020 ºC for the growth of high quality GaN-based films. They concluded that the Mg-doped 2.0 µm-thick GaN film showed the best fit for SAW sensor compared to the other samples. The Mg-doped GaN presented sheet resistivity higher than 10^7 Ωcm, Root Mean Square (RMS) roughness of 0.7 nm and good crystallinity quality (full width at half maximum (FWHM) = 460 arcsec), and the resulted sensor presented a center frequency of ~100 MHz.

Similarly, Ciplys et al. (2002) [81] fabricated a SAW delay-line oscillator sensitive to UV light. The SAW oscillator was composed of GaN layer grown on (0001)-oriented sapphire via low-pressure MOCVD. The GaN layer thickness was varied from 1.4 to 2.4 µm. Furthermore, the resulted sensor showed center frequency around 200 MHz.

In 2010, a work developed by Chivukula et al. [82] obtained a SAW sensor operating with a center frequency of 306 MHz for UV detection. For this, the authors deposited 2.4 μm-thick GaN layer via MOCVD onto c-sapphire. Using SiC as substrate, Rýger et al [83] deposited 1.7 μm-thick GaN film also by MOCVD but their IDTs had sub-micrometer dimensions. Based on their design they fabricated a GaN-based SAW sensor with center frequency around 2 GHz. Later, Müller et al. [12,36] used a commercial 1.0 μm-thick GaN/Si grown by MOCVD and for different IDT designs, they got center frequencies ranging from 5 to 7 GHz.

Boldeiu et al. (2022) [76] utilized commercially grown GaN through MOCVD on both SiC and sapphire substrates to fabricate a high sensitivity temperature sensor. The GaN had a thickness of 1 μm and a (0001) crystallographic orientation. Despite using the same design for both devices, the resonant frequencies for GaN/SiC and GaN/sapphire were approximately 4 GHz and 3 GHz, respectively. The GaN/Sapphire SAW device exhibited a higher absolute value of temperature coefficient of frequency (TCF) sensitivity (96.5 ppm/°C) than the GaN/SiC structure (46 ppm/°C). The authors attribute this difference to incomplete information on how material parameters vary with temperature.

In 2023, Jaafar et al. [84] growth 2 μm-thick GaN epitaxial layer by MOCVD on a 125 nm-thick aluminum nitride (AlN) buffer layer deposited on sapphire substrate. The GaN epitaxial layer showed a smooth GaN epitaxial layer with a lower density of etch pits and without any large waves and grains. Also, it presented a root mean square value of 0.212 nm. The authors observed difference center frequency attributed to the different acoustic modes. The center frequency around 462 MHz, 809 MHz, and 1.071 GHz correspond to the Rayleigh mode, Sezawa mode, and sapphire pseudo-bulk mode, respectively.

Moreover, Chang et al. (2021) [85] used a piezoelectric layer of aluminum gallium nitride (AlGaN), with a thickness of 1160 nm, in the production of solidly mounted resonators (SMR) for high-frequency acoustic wave devices. The AlGaN film was deposited on a Bragg reflector, which was comprised of three pairs of Mo and SiO_2 films, using a reactive RF magnetron co-sputtering system at RT. The resulting AlGaN film exhibited a smooth surface, uniform crystal grain distribution, and strong c-axis orientation. Ultimately, the frequency response S_{11} of the SMR device displayed a center frequency of 3.60 GHz.

There are many methods to grow GaN thin films. The widely used techniques for GaN epilayers deposition are chemical vapor deposition (CVD), MOCVD, and MBE [31,86–88]. As clearly stated above, for applications in SAW devices, the widely used technique for GaN growth is MOCVD. However, these techniques are quite expensive, complex, non-

environmentally friendly, and most times require high temperature of reactions, limiting the diversity of substrates [89]. For example, CVD system uses toxic gases to provide the reactions and requires cautious handling procedure [86]. MOCVD technique entails high growth temperature to turn the ammonia gas into active nitrogen species [87]. In addition to the use of toxic gases and high temperature, MBE technique requires ultra-high vacuum conditions [88]. Sputtering is simpler and cheaper than the conventional techniques, and it allows the production of thin films in shorter times with good quality.

2.3.   Graphene

GR is a 2D sheet composed of sp^2 hybridized carbon atoms arranged in a crystal honeycomb lattice that is only one atom thick [21,90]. It can be prepared by various methods, including micromechanical cleavage, CVD, exfoliation of graphite, and chemical oxidation-reduction methods [91]. Theoretically, GR exhibits a range of interesting properties, such as a large specific surface area ($\sim$2630 m^2 g^{-1}), high electron mobility ($\sim$200,000 cm^{2}V^{-1} s^{-1}), optical transparency ($\sim$97.7%), exceptional thermal conductivity ($\sim$5000 Wm K^{-1}), superior mechanical properties with Young's modulus of 1 TPa, high electrical conductivity, zero gap, and functionalization possibilities [37,51,52,92,93].

These properties make GR an attractive material for nanoelectronics applications and a suitable candidate for sensing applications, particularly in SAW sensors [10,37]. This is due to the attenuation of the acoustic wave propagation caused by the adsorption of molecules on the GR film, which is extremely sensitive to surface perturbations [10,21,37,93]. GR can be used for diverse sensing purposes, including humidity, gas, UV, and biosensing (**Figure 3**). The shape and size to which this material is applied can change the sensor's performance.
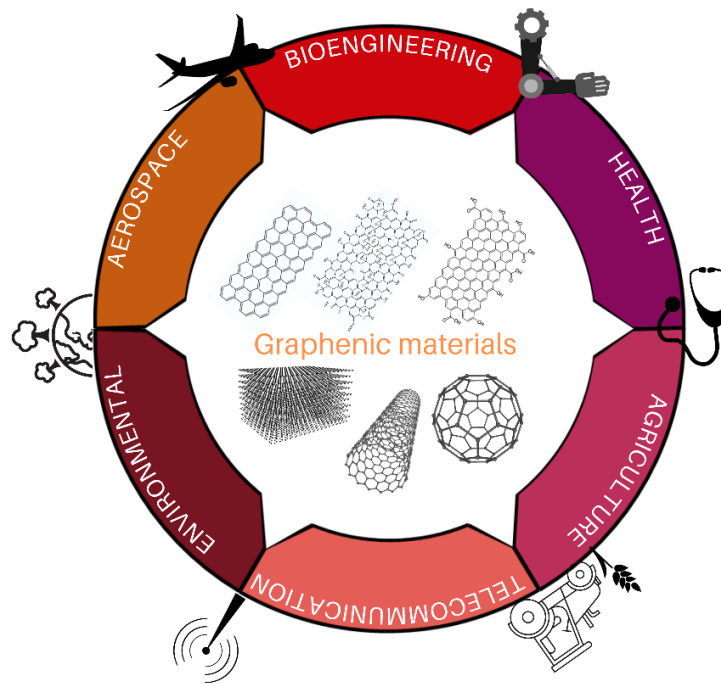
Figure 3: The main application of SAW devices based on graphenic materials.

As humidity sensor, Su et al. (2020) [94] applied a 3D architecture graphene (3DAG) as sensing layer to beneficially use its macropores for the adsorption and flux of gas molecules on the surface and inside of its structure [95–97]. The 3DAG was grown on Ta substrate using the CVD method and peeled from the Ta substrate using a polyvinyl alcohol (PVA) film. The peeled 3DAG/PVA was transferred to the bare SAW device and no apparent change in center frequency was observed, but the insertion loss was increased. Also, the 3DAG/PVA/SiO$_2$/Ta sensor showed improved sensing properties, especially when the RH was higher than 55%. The sensitivity also increased by about a factor of two compared with a bare SAW sensor, and a fast response-recovery, good repeatability, and stability was observed indicating its appropriateness for respiration monitoring.

Graphene quantum dots (GQDs) can provide more oxygen-containing functional groups compared to a 2D structure. Because of that, GQD can significantly improve the SAW sensing performance when combined in composites using polymers and metal oxides. Wu et al. (2020) [97] used zinc oxide (ZnO) nanowires (NWs) and GQDs to form a composite sensing layer (ZnO/GQDs) in a flexible SAW humidity sensor. The GQDs enhance the capacity of ZnO to adsorb water molecules due to the formation of p−n heterojunctions. The authors found that for a constant frequency of 138.35 MHz, the sample with a higher concentration of GQDs (2 mg mL^{-1}) exhibited 18 times higher sensitivity than the SAW device with a lower

concentration of GQDs (0.1 mg mL^{-1}) and 88 times higher sensitivity than a SAW sensor without the composite sensing layer at 80% RH. Additionally, a reduction in the response and recovery time of the SAW humidity sensor was observed with the sensing layer.

GR-based sensing layer has also been used for gas detection. Xu et al. (2015) [21] reported a GR–nickel (Ni)–L-alanine composite sensing layer (GR/Ni/L-alanine) on a quartz substrate as SAW sensor for CO_2 detection. GR enhances the sensitivity because of its ability to adsorb CO_2 while Ni nanoparticles (NPs) catalyze the reactions between L-alanine and CO_2 gas molecules. The GR/Ni/L-alanine SAW device showed the greatest Δf between air and CO_2. The response of the sensor increased rapidly as a function of CO_2 concentration when exposed to concentrations of CO_2 from 0 to 38,500 ppm. The LOD of CO_2 was 200 ppm, and from 0 to 2,000 ppm, and from 2,000 to 38,500 ppm, the sensor presented sensitivity of 2.51 MHz.ppm^{-1}.m^{-2} and 0.46 MHz.ppm^{-1}.m^{-2}, respectively.

Xu et al. (2021) [22] used a porous molecularly imprinted GR/PVDF film as a sensitive membrane on a quartz substrate for DMMP gas detection. The porous GR increased the specific surface area of the sensing film and facilitated gas adsorption, while PVDF protected the metal interdigital electrode. The bare sensor with a resonance frequency of 434.9 MHz, presented a frequency shift of about 294 kHz due to the mass loading effect after the porous GR/PVDF film was fabricated on the sensor's surface. The sensor assembled with a sensing film exhibited a sensitivity of -1.407 kHz ppm^{-1}, response time of 4.5 s and a recovery time of approximately 5.8 s.

The different applications of GR are intrinsically related to its electrical properties. The ability to modulate and control the electronic properties of GR in different media has become an important feature from a commercial application point of view. GR is capable of sensing electric fields that are present alongside traveling SAWs through the creation of acoustoelectric current (I_A) [98,99]. An example of such a device is the graphene field-effect transistor (GFET). To exploit this property of GR, Okuda et al. (2018) [10] combined a GFET with an SH-SAW on a LiTaO$_3$ substrate. They aimed to develop a hybrid sensor, called a graphene surface acoustic wave (GSAW) biosensor, capable of detecting both charge and mass at the same time. Amine-modified silica microbeads with varying densities, ranging from 0 mg mL^{-1} to 6.95 mg mL^{-1}, were introduced into the buffer solution. The increase in microbeads density in the solution caused protonation of the amino groups, resulting in a displacement of the hole current peak towards the lower left. The rise in density also caused mass loading on the SAW path, which resulted in a decrease in its amplitude. Thus, the results demonstrate that the GSAW can operate

as a transducer that detects charge and mass simultaneously contributing to the development of multifunctional sensors with high sensitivity and multifunctionality.

Researchers in the field of biosensors are becoming more interested in the use of GR-related materials. Carbon-based coatings show advantages compared to traditional materials used as sensitive layers for biosensors (such as nanogold films) due to the presence of the sp^2 hybridized carbon atoms in their structural backbone, which provides a route for surface modifications [100]. Ji et al. (2020) [100] studied an SH-SAW biosensor with a single layer graphene (SLG) film in the sensitive area to detect endotoxin, a complex lipopolysaccharide responsible for the adverse effects in human and animals that cause fevers, septic shock, and sepsis. The SLG film was synthesized using CVD on a copper foil and transferred to a quartz substrate. The SLG film had an aptamer, a substance with high affinity and specificity to bind to a target molecule, immobilized on its structure to detect endotoxin [101]. The performance of the biosensor showed a linear detection sensitivity between 0 and 100 ng mL^{-1} with a LOD of about 3.53 ng mL^{-1}. Additionally, the biosensor had excellent selectivity since it did not show any response when submitted to non-target biological samples.

Ji et al. (2020) [102] also developed a biosensor comprised of SLG/Au NPs for the detection of *Staphylococcus aureus* gene sequences. The base frequency of the biosensor was 282.3 MHz. The SLG was deposited onto the surface of the sensitive area, and Au NPs were uniformly loaded onto the CVD-grown SLG film using electron-beam evaporation (EBE). The sensitivity against *S. aureus* gene sequences showed a linear detection range from 0 to 10 nmol/L with a LOD lower than 12.4 pg mL^{-1}. Moreover, the proposed biosensor showed excellent stability in the liquid phase for more than 0.5 h ($\pm 0.1°$).

Therefore, a variety of modification methods using GR are available for SAW devices, some latest data are listed in **Table 1.** This material, if well utilized, can enhance the SAW device's performance.

Table 1: Examples of GR-based SAW devices reported from 2012 to 2022.

Piezoelectric base	Sensing layer	Target	Sensitivity	LOD	Response / recovery time (s)	f(MHz)	Ref
ST-cut quartz	GR/Ni/ L-alanine	CO_2	2.51 MHz ppm^{-1}.m^{-2}	200 ppm	-/20	434	[21]
ST-cut quartz	GR/PVDF	DMMP	−1.407 kHz ppm^{-1}	3 ppm	2.9/3.7	435	[22]
ST-cut quartz	3DAG/ PVA/ SiO$_2$	RH	−0.991 kHz %RH^{-1}	5%	24/14.4	204	[94]
Glass	GQDs/ ZnO NWs	RH	40.16 kHz %RH^{-1}	30%	27/12	220	[97]
Glass	GQDs/ ZnO NWs	UV light	1.53 ppm mw^{-1} cm^{-2}	30 mw cm^{-2}	8/18	220	[103]
36° Y-90° X quartz	SLG	Endotoxin	0.044 deg ng^{-1}mL^{-1}	3.53 ng mL^{-1}	-	246	[100]
ST-90° X quartz	SLG/Au NPs	S. aureus gene sequences	-	12.4 pg mL^{-1}	-	282	[102]

*f(MHz) = central frequency

2.4. Poly(o-methoxyaniline)

Conjugated polymers are materials with unique electrical and optical properties due to their conjugated π bonds along the polymer backbone [104,105]. They have been widely used in electronics, sensing, and biology because of their flexibility, low cost, ease of chemical modification, semiconducting properties, and low cytotoxicity. The homo-polymerization of single aromatic units such as aniline, o-anisidine, and pyrrole requires oxidative polymerization, which is used to synthesize PANI, POMA, and polypyrrole (PPy). In these cases, iron(III) sulfate ($Fe_2(SO_4)_3$) and $(NH_4)_2S_2O_8$ are commonly used as initiators of the reaction containing liquid conjugated monomer.

There have been extensive applications of doped conductive polymers including corrosion protection [106], microwave absorber [107], supercapacitors [108], and sensors [42]. Among the

commonly used conductive polymers, PANI has been extensively used in the gas sensor field due to their unique properties, convenient synthesis, strong conductivity, and ability to detect ammonia gas at RT [40]. However, the practical application of PANI in sensors is limited due to the strong rigidity of the aniline chain, and low solubility of the polymer, resulting in limited processability and unattractive mechanical properties for commercial purposes. To address these limitations, organic acids have been used to dope the PANI and increase its solubility in common organic solvents as well as compatibility with other processing polymers [109]. As a result, researchers are currently focused on developing long-chain PANI and its derivatives with improved solubility to overcome these limitations.

POMA, also known as poly(o-anisidine), is a type of conjugated polymer derivative of PANI. POMA contains a methoxy group ($-OCH_3$) on the ortho-position of the phenyl ring, which increases its solubility in organic solvents and processability without compromising its optical and electronic properties [57,110]. One of the POMA limitations is that its electrical conductivity can be lower than the PANI due to the methoxy group present in the carbon ring. However, this property is dependent on the doping level, the type of dopant and the synthesis method. Thus, the wide range of conductivities design allows obtaining materials with predesigned electrical conductivity, accordingly with the desired application [57,111]. Biondo et al. [112]. prepared POMA doped with HCl, HNO_3, H_2SO_4 and H_3PO_4 by in situ chemical oxidative polymerization [57]. The authors observed that the nature of the counterions directly impact the structure and electrical properties of the POMA. For example, the use of HCl, HNO_3 and H_2SO_4 as dopant acid resulted in around 50% of crystallinity, whereas the use of H_3PO_4 presented crystallinity around 40%. Additionally, the variation in the dopant acid resulted in an electrical conductivity (EC) range of 6.6×10^{-1}-5.2×10^{-4} S cm^{-1}, being the most and less conductive doped with HCl and H_3PO_4, respectively.

POMA is cost-effective, environmentally safe, thermally stable, and biocompatible, making it useful in electronic, photovoltaic, and optical applications. POMA has been used in transistors [113], solar cells [114,115], supercapacitor [108], resistive random-access memories [104], and sensors [39,41,116].

Many SAW sensors have been reported, mainly focused on exploring sensitive materials with good sensing characteristics. Polymers are highly recommended as humidity sensitive materials because they exhibit low cost, adjustable properties, and ease of fabrication.

In work developed in 2013 by Wang et al. [117], the emeraldine form of PANI was used as sensing layer in a quartz-based SAW device for humidity sensing. In the RH range of ~0.5%–

17%, the sensor response presented linearity and sensitivity of 106 Hz/%RH. Conversely, in the RH range above 20% RH, the sensor response became nonlinear. The authors understand that at low humidity, the water vapor adsorbed in the PANI layer changed only the conductivity being the main sensor response mechanism, while at high humidity, both conductivity and viscoelasticity of PANI changed, leading to greater disturbance of the SAW propagation and less control of the sensitivity.

In 2022, Memon et al. [118] presented a SAW sensor for humidity detection using polyimide (PI) as sensing layer. The PI film was spin coated on the SAW resonator and the performance of the device was studied in the range of 10-90%RH and it presented sensitivity of 4.15 kHz/RH, and response and recovery time of 7 s and 13 s, respectively.

Similarly, in 2022, Prabakaran et al. [119] prepared a SAW sensor for L-Tryptophan detection that was assembled by casting hydrophilic PVDF as sensing layer on a quartz substrate. The center frequency and LOD of the device were calculated to be 170 MHz, and 0.2 ng/ml, respectively.

In addition to the polymers' interesting features, polymer-based nanocomposites can be more effective at adsorption due to their increased surface area. This increased detection area of nanostructured materials can lead to improved sensing capabilities and adsorption capacity. To achieve a high signal-to-noise ratio and a short sensor response time, it is desirable to prepare very thin and uniform sensitive films. However, obtaining nanocomposites with consistent structural features such as particle morphology can be challenging, as the dispersion of filler particles in the polymer matrix is often uneven. Additionally, particles can be prone to agglomeration in composite materials, and the crystalline quality can be adversely affected during composite preparation. These limitations can often be overcome by the conditions of synthesis and applications.

A study conducted by Wang et al. (2023) [120] proposed a SAW formaldehyde sensor that utilized a composite film of GR and polymethyl methacrylate (PMMA), demonstrating high sensitivity and short response and recovery time. To achieve uniform dispersion of GR sheets in the PMMA film, a multisource spray deposition method was employed. The formaldehyde-sensing ability was further improved by optimizing the film thickness and operating temperature.

Building upon the fundamentals, this study aims to assess POMA's effectiveness as a sensing layer and introduce CBFG as a filler in its matrix to create an innovative nanocomposite for SAW sensors.

CHAPTER 3. GaN films by sputtering

This chapter is dedicated to discussing the obtaining of high-quality GaN film via the reactive sputtering technique and presenting the results to justify its use as a piezoelectric material in SAW devices. The fundamentals of the technique used in the methodology are addressed.

3.1. Reactive magnetron sputtering

Sputtering deposition is a technique for producing thin films via physical vapor deposition (PVD) [121,122]. It involves bombarding a target material with high-energy ions to eject atoms that then condense onto a substrate. Reactive sputtering is a variation of this method that uses a reactive gas introduced into the sputtering chamber to react with the sputtered material, condense onto the substrate's surface, and form a compound. The magnetron sputtering technique is a type of sputtering system that includes permanent magnets located beneath the target. This design boosts efficiency and reduces the minimum pressure limit by creating plasma that ionizes the gas, generating high-energy ions that bombard the target material [121,122]. For example, in this work, the magnetron is placed under the target (liquid Ga), and reactive gas (nitrogen) is injected into the chamber and reacts with Ga to form GaN and further condense onto the surface of the substrate (glass or silicon).

Reactive magnetron sputtering offers advantages in controlling thin film properties, such as thickness, stoichiometry, and crystal structure, and can be performed at low temperatures, making it ideal for temperature-sensitive substrates [121,122]. However, precise process parameter control is necessary, and defects may form in the thin film. Despite these limitations, sputtered AlN and AlGaN on SiO_2/Mo/Si(100) substrate have been used to create solidly mounted resonator devices operating with a center frequency of ~3.5 GHz [123]. Sputtered AlN on Si and glass substrates were also used to produce SAW resonators with a center frequency of ~4.2 GHz for use as temperature sensors [124]. Additionally, in a study led by Oliveira et al. (2022) [125], the impact of working pressure and RF power on GaN film growth properties on Si(100) and glass substrates was investigated. The authors discovered that heating the substrate to 550 ºC, applying an RF power of 60 W to the Ga target, and using a working pressure of 0.3 mTorr improved the crystalline quality of the films. These nanocrystalline films with high orientation possessed crystalline qualities appropriate for device use.

3.2.   Materials and Methodology

Table 2 lists all reagents used in this step and their respective manufacturers.

Table 2. Information on reagents used in this work.

Reagent name	Molecular formula	Provider	Purity	CAS number
Sulfuric acid	H_2SO_4	Synth	95-98%	7664-93-9
Hydrogen peroxide	H_2O_2	Synth	30%	7722-84-1
Acetone	C_3H_6O	Fisher Chemical	>99.5%	67-64-1
Isopropyl Alcohol	C_3H_8O	Fisher Chemical	≥99.5%	67-63-0
Liquid Ga	Ga	Process Materials Inc	99.999%	7440-55-3
Extran detergent	-	Merck Millipore	-	-

3.2.1.   Substrates cleaning process

The silicon wafers underwent a cleaning process using a piranha solution to remove organic residues and oxides from the surface. Initially, they were washed with deionized water and dried with compressed air. Then, 30 mL of H_2SO_4 were added to a 2 L beaker, followed by 10 mL of H_2O_2 added dropwise in a 3:1 ratio. The previously cleaned wafers were added to the solution and left to react for 15 minutes or until the bubbling on the surface disappeared. Subsequently, the wafers were immersed in deionized water in another beaker, repeating the process twice. Finally, the wafers were removed from the beaker with Teflon tweezers and dried with compressed air.

The glass substrates were cleaned by brushing the glass slides in a detergent solution (Extran 300 Liquid Detergent), and sonicating the substrates in ethyl alcohol, IPA, and acetone for 1 min each to remove insoluble organic contaminants. The samples were dried with compressed air.

3.2.2.   Sputtering of GaN thin films

GaN films were grown on Si(100) and borosilicate glass substrates using a dedicated reactive tri-magnetron sputtering deposition system for III-nitrides thin films. The system was installed in a spherical ultra-high vacuum (UHV) chamber (KJ Lesker SP1800SEP) made of 304 stainless steel and equipped with a 4-inch TOROUS® magnetron containing liquid Ga. The magnetron was located 90 mm from the substrate

holder, which rotated and heated the substrate. A 600W RF-power supply with matching box (SEREN R301 + SEREM MC2) powered the magnetron. The deposition conditions of GaN thin films on Si and glass were previously optimized and more detailed information can be found elsewhere [125].

In summary, the GaN deposition was carried out using a 1:2 mass flow ratio of Ar and N_2 gases, independently supplied to the system, at a substrate temperature of 550 °C, a working pressure of 3 mTorr, deposition times of 2, 4 and 6 hours, and a rotation speed of 6 rpm. The liquid Ga target was subjected to an RF power of 60 W during deposition.

3.2.3. Characterization

Producing a GaN piezoelectric material with good crystal quality (few defects) and surface morphology (smooth surface) is crucial for SAW propagation from an input to an output IDT [80,84,85,126]. Hence, characterization techniques are used to obtain information about the structural and morphological quality of the produced GaN films, as these characteristics greatly impact the performance of SAWs.

3.2.3.1. X-Ray diffraction of GaN thin films

The GaN thin films were characterized using XRD on a Rigaku SmartLab diffractometer with a Cu Kα X-ray tube, using the ω-2θ configuration in continuous mode. All measurements were performed at a voltage of 40 kV and a current of 44 mA, with a 5 mm mask and a scan speed of 0.1 °/s. The scanning range was set to 30° to 70° for all samples. Additionally, X-ray pole figures of selected GaN reflections were measured. The Bragg angle (2θ) for the selected reflection (34.55º) was kept constant whereas the tilt angle χ (ranging from 0 to 90º) and the rotation angle ϕ (ranging from 0 to 360º) of the sample were varied. Then, the intensity of the diffracted beam was taken as a function of the angles χ and ϕ to create the pole figure. Only a pixel detector with Soller slits of 5º was used in the path of the diffracted beam for these measurements.

3.2.3.2. Raman spectroscopy of GaN thin films

The vibrational properties were investigated using Raman spectroscopy to study the E_2 (high) and A_1 (LO) phonon modes in the GaN thin films. For this, the Raman spectra of GaN/glass samples, with plotted standard deviation, were collected using a Renishaw inVia Raman microscope outfitted with a 5 mW 532 nm laser. A 50x objective lens, 10% filter, 20 s duration time, and 20 accumulations were the parameters used to

collect all spectra. The Raman spectra were recorded in the range of 350-1250 cm^{-1}. The analysis was not performed on GaN/Si samples because silicon produces a high-intensity signal under the green laser.

3.2.3.3. Scanning electron microscopy of GaN thin films

Cross-sectional SEM images were collected using a FEI Helios 660 instrument. Samples were prepared using focused ion beam (FIB) milling. First, carbon was deposited by electron beam to protect the thickness of the GaN, then FIB deposition was used to further grow the protective upper C layer. Then, FIB milling was used to cut angled cross-sections to determine the GaN thickness. A voltage of 15 keV was employed in imaging.

3.2.3.4. Atomic force microscopy of GaN thin films

AFM measurements of GaN/Si samples were collected on a Park SmartScan NX20 AFM in tapping mode using TESPA-V2 cantilevers. A 1.00 Hz scan rate and 512-pixel resolution was used. Surface roughness RMS and relative sharpness of morphology (Sku) were determined from randomly selected 10x15 µm areas of the samples.

3.2.3.5. Transmission electron microscopy of GaN thin films

High resolution TEM images were collected using a double-tilt holder on a JEOL 2100F instrument to evaluate the crystallinity of the GaN on Si wafer. For that, the samples were prepared using the FIB on the Helios to mill a very thin cross section of the material. First, a non-destructive E-Beam deposition was used to layer a small pad of amorphous carbon on top of the GaN substrate to preserve the thickness and integrity of the GaN layer. Then the FIB was used to deposit an even thicker layer atop that. The cross section was cut out and under the protective amorphous carbon layer, the GaN was preserved as the carbon is milled first. After being prepared, the cross section was mounted on the TEM grid and further imaged by TEM. An accelerating voltage of 200 kV was used.

3.2.3.6. X-ray photoelectron spectroscopy of GaN thin films

XPS data were collected using a PHI Quantera SXM scanning X-ray microprobe with a base pressure of 5×10^{-9} Torr. Survey spectra were recorded using 0.5 eV step sizes with a pass energy of 140 eV. Elemental spectra were recorded using 0.25 eV step sizes with a pass energy of 69 eV. The XPS data was also obtained after sputtering an

area of 3×3 mm^2 using a 4 kV Ar$^+$ sputter source for 6 min with an interval time of 2 min per acquisition layer. The process was repeated 3 times and resulted in the acquisition of four spectra referring to 4 layers, including the surface. All the XPS spectra were corrected using the C*1s* peaks (284.8 eV) as reference.

3.2.3.7.   Electrical properties of GaN thin films

The GaN/glass samples were rinsed with acetone and IPA and dried with N$_2$ gas. Then, the source and drain electrodes were patterned onto the samples using the maskless photolithography method. For this, the photoresist S1818 (PR) was deposited on the GaN thin film surface by spin-coating (Laurell Tech WS-650) at 500 rpm for 5 s to spread, and 3000 rpm for 60 seconds to make it uniformly deposited. The samples were pre-baked for 60 seconds at 100 ºC. Then, the samples were placed in the maskless lithography system (Bruker - SF-100 Lightning) and exposed to UV for 1.2 seconds. The patterns were developed with a Microposit^{TM} MF^{TM} -321 developer for 30-40 seconds. In the Load-Lock E-beam Evaporator (Kurt J. Lesker - PRO Line PVD75), 50 nm of metal (Au) was deposited to form the electrode. Finally, to lift off the residual PR, the samples were dipped in acetone for 6 hours. **Figure 4a** shows the three pads that were fabricated with a width of 100 μm, a spacing of 20 μm between them, and a height of 10 nm of Ti and 50 nm of Au. Then, current–voltage (I-V) curves were obtained using a semiconductor parameter analyzer (HP Hewlett Packard 4145A), with the pads spaced 20 μm apart from each other, as depicted in **Figure 4b**. **Figure 4c** represents the gap between the IDTs and the photoresist residue on these fingers. To remove the remaining residue, the samples were sonicated for 10 seconds in acetone, which improved the development but caused a detachment of the Au pads. Additionally, PR residues remained (**Figure 4d-f**). No further steps were taken. The entire microfabrication procedure was performed in a Cleanroom Class 100 (ISO 5).
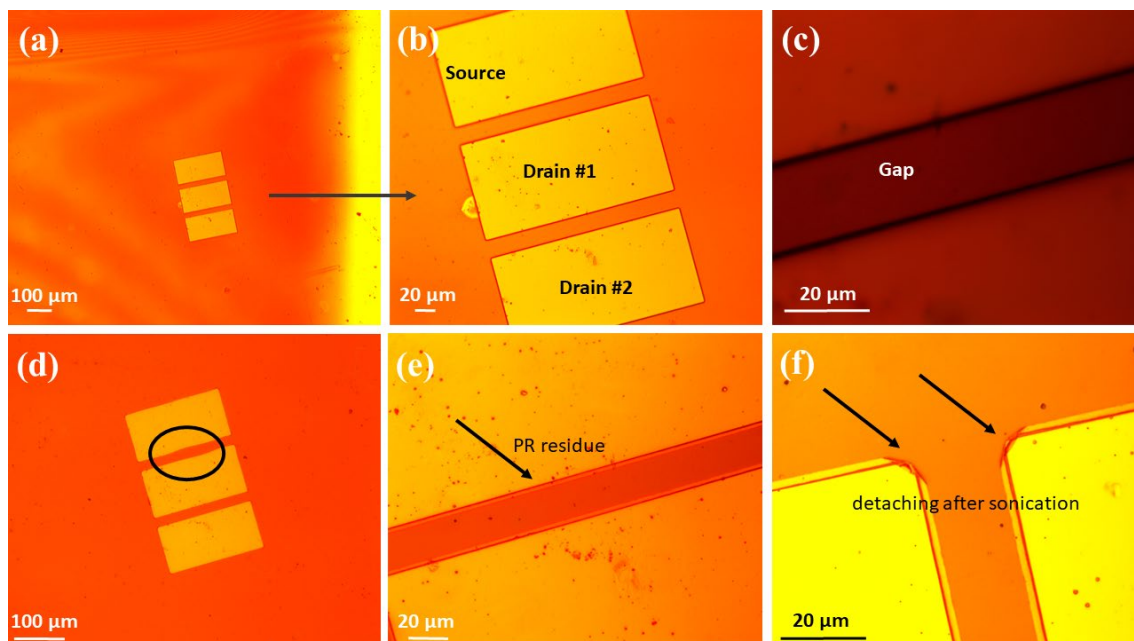
Figure 4: Optical images of the metallic contacts after 30-40 seconds of development time at (a) 10x, (b) 20x, and (c) 100x of magnification from an optical microscope; and after sonication in acetone for 10 s, the pattern presents (d) over development, (e) PR residue, and (f) extreme detaching of Au along with PR residue.

3.3. Results and discussion

3.3.1. Characterization

3.3.1.1. X-Ray diffraction of GaN/Si(100) samples

The structural properties of GaN grown on silicon and glass substrates were obtained using XRD. To assist the readers in this section, the thicknesses of the samples were 329 ± 17 nm, 569 ± 30 nm, and 1162 ± 36 nm, for samples grown for 2 h, 4 h, and 6 h, respectively. This result will be discussed in the microscopy section.

Figure 5 shows the non-normalized XRD patterns obtained by Bragg-Brentano method of the GaN films grown at three different times on Si(100) substrate. The indexed peaks revealed polycrystalline GaN films with (hexagonal) wurtzite crystal structure, highly orientated to the *c*-direction. This structure matches with the indexed PDF Card No.: 01-089-7522 (GaN, space group: P63mc, a = b = 3.1891 Å, c = 5.1853 Å). There was no evidence of significate changes in the diffraction pattern of the samples grown by different times [127].

The XRD patterns in **Figure 5** exhibited peaks for GaN at 34.55° in all samples for the (0002) plane, 36.92°, 36.82º, and 36.84º for the (10$\underline{1}$1) plane, and 63.53º, 63.41º, and 63.48º for the (10$\underline{1}$3) plane. These results indicate that hexagonal-GaN (h-GaN) was

successfully deposited on the Si(100) substrate using magnetron sputtering with strong (0002) preferred orientation, i.e, with *c*-axis preferentially oriented perpendicularly to the substrate surface. It is worth noting that no peak for cubic-GaN (c-GaN) was detected in the XRD patterns, even though the four-fold symmetry of Si(100) is known to favor the growth of a cubic phase [128]. For high frequency SAW device applications, the GaN films with a preferred orientation along the (0002) crystal plane and with wurtzite structure is preferred than the zinc-blend (cubic) as it is more stable, has larger elastic modulus, higher theoretical band gap, and is anisotropic (essential for piezoelectricity) [129–131]. Additionally, these diffraction intensities become more intense as the deposition time increases due to the increase in thickness.
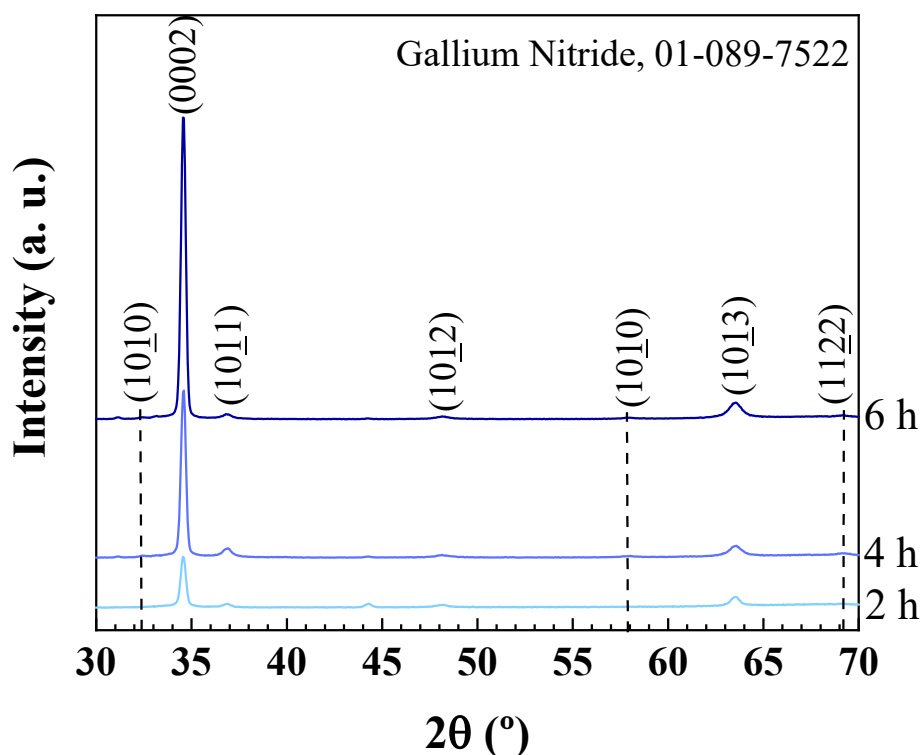
Figure 5: X-ray diffractograms of GaN thin films grown on a Si(100) substrate with different deposition times using magnetron sputtering technique.

Larger crystallites sizes and therefore an enhancement in the crystalline quality for films deposited for a long period of time was expected. However, as shown in **Table 3**, there is no linear tendency in the crystalline size as the deposition time increases. Crystallite size (D) values were calculated from the (0002) reflections using Scherrer equation, and they were found to be 331 ± 5 Å, 324 ± 2 Å, and 348 ± 2 Å for GaN films

deposited at 2, 4, and 6 hours, respectively (**Table 3**). The thicker GaN film (deposited for 6 h) exhibited a decrease in the FWHM and an increase in D, possibly due to its ability to act as a self-buffer layer for the neighboring columnar morphology. This helps to alleviate substrate tension and promotes a higher quality and highly oriented morphology with larger crystallites.

Table 3: FWHM (0002) and D for GaN/Si(100) samples.

Deposition time (h)	FWHM (º)	D (Å)
2	0.279 ± 0.004	331 ± 5
4	0.285 ± 0.002	324 ± 2
6	0.265 ± 0.001	348 ± 2

Figure 6 shows the normalized X-ray diffraction pattern of GaN thin films grown on Si(100) of the GaN (a) (0002), (b) (10$\underline{1}$1), and (c) (10$\underline{1}$3) peaks. The data normalization was done by dividing the data by the mean. According to the indexed GaN PDF card, the (0002), (10$\underline{1}$1), and (10$\underline{1}$3) plane positions estimated for the unstrained GaN are 34.57º, 36.84º, and 63.44º, respectively (PDF card No 01-089-7522). The sample grown for 4 h showed the most significant shift for all planes, indicating it has a high defect density, while the sample grown by 6 h presented the plane positions closer to the stress-free GaN film, being the one with better quality.
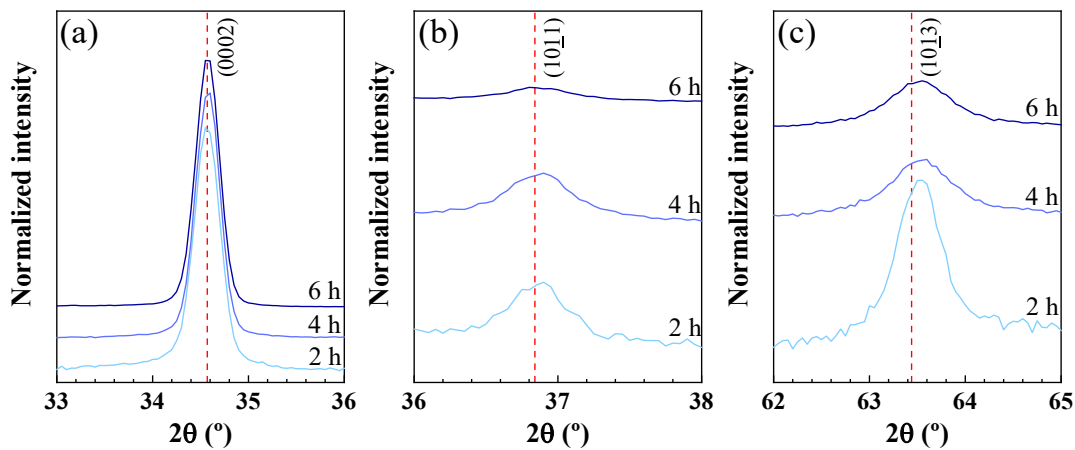
Figure 6: Expanded XRD in the interval (a) 33°-36°, (b) 36º-38º, and (c) 62º-65º, showing the main diffraction peaks of the GaN/Si samples and respective expected degree positions (vertical red dashed lines).

The shift seen in the XRD can be used to verify the quality of the films based on expansion or contraction of the unit cell due to defects. Then, the lattice parameters a and c were calculated, and they are shown on **Figure 7**. According to the indexed PDF Card, the values of a and c are, respectively, 3.189 Å and 5.185 Å for unstrained GaN and the c/a ratios is 1.63 for GaN. As expected by the previous discussion, GaN film grown for 6 h presented lattice parameter closer to the unstrained structure.
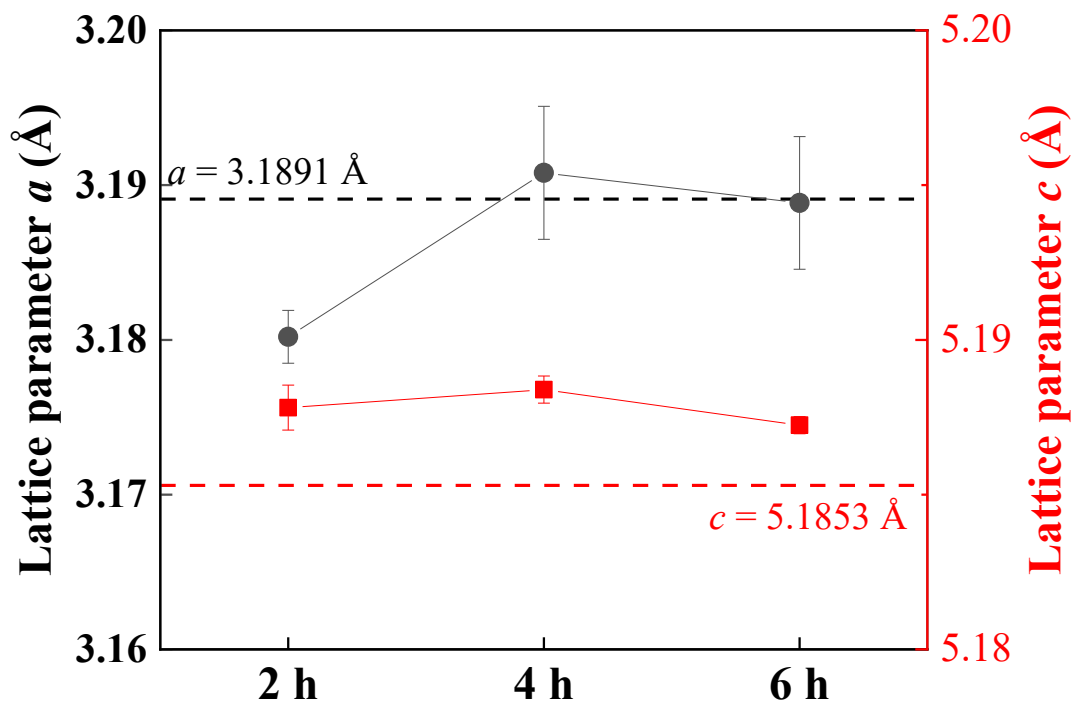
Figure 7: Structural parameters of GaN grown on Si for 2 h, 4 h, and 6 h. The black and red dashed lines identify the lattice parameters a and c, respectively, of the unstrained GaN according to the PDF card.

To further investigate the alignment and orientation of GaN films, XRD pole figures were measured for two reflections. The first reflection analyzed was the GaN (0002) reflection, as shown in **Figure 8**. The most prominent diffracted signal (0002) was observed in the center of the pole figure for all samples, and it shows that the GaN films grow preferentially oriented along the out-of-plane (surface normal) direction [132–134]. The (0002) planes of all samples exhibited some degree of tilt. However, the spot at the center of the (0002) pole figure for the GaN grown for 2 h was significantly dispersed, suggesting a weakened preferred orientation along the surface normal compared to the

other samples [135]. On the other hand, the GaN grown for 4 and 6 hours maintained a highly preferred orientation along the surface normal, with some domains still exhibiting the preferred orientation but with slight tilting along the surface normal, as shown in **Figure 8**. There could be two possible phenomena occurring in this case [136]. Firstly, it is likely that the crystal inclination angles are significantly smaller than the columnar angles, resulting in the dominance of the *c*-axis crystal orientation (0002) for the majority of the columnar inclined films. Alternatively, the deposited inclined films may consist of a mixture of vertically aligned crystals and crystals with inclined angles.
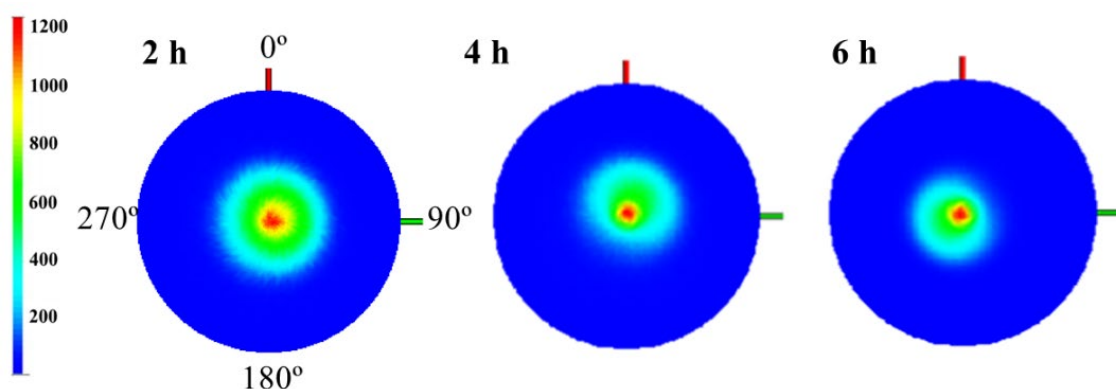
Figure 8: X-ray diffraction pole figures of GaN (0002) reflection of the sample grown on Si for 2 h, 4 h, and 6 h.

3.3.1.2. X-Ray diffraction of GaN/glass samples

Figure 9 shows the non-normalized XRD patterns obtained by Bragg-Brentano method of the GaN films grown at three different times on glass substrate. The indexed peaks revealed the same structure of the GaN grown on Si and matches with PDF Card No.: 01-089-7522.

The XRD patterns in **Figure 9** showed peaks for GaN at 34.47°, 34.55°, and 34.48° for the (0002) plane, 36.70°, 36.75°, and 36.64° for the (10$\underline{1}$1) plane, 63.30°, 63.25°, and 63.33° for the (10$\underline{1}$3) plane, corresponding to samples grown for 2, 4, and 6 h, respectively. These results indicate the succeed obtention of h-GaN on glass using magnetron sputtering.

Higher intensities in the (0002) planes indicate that the crystallites are mostly oriented with the *c*-axis perpendicular to the substrate surface. The preferred orientation became more intense with an increase in deposition time, but it remained higher than expected for non-oriented GaN grown for 2 h. Conversely, the (10$\underline{1}$1) peak demonstrated

the inverse behavior, with the most intense peak associated with a lower deposition time. According to the van der Drift model [137], thinner films are primarily composed of the first nucleation layers, which are mostly randomly oriented. As the thickness increases, the crystallites with fast growth direction aligned with the film growth direction dominate the film's composition, resulting in a highly oriented film.
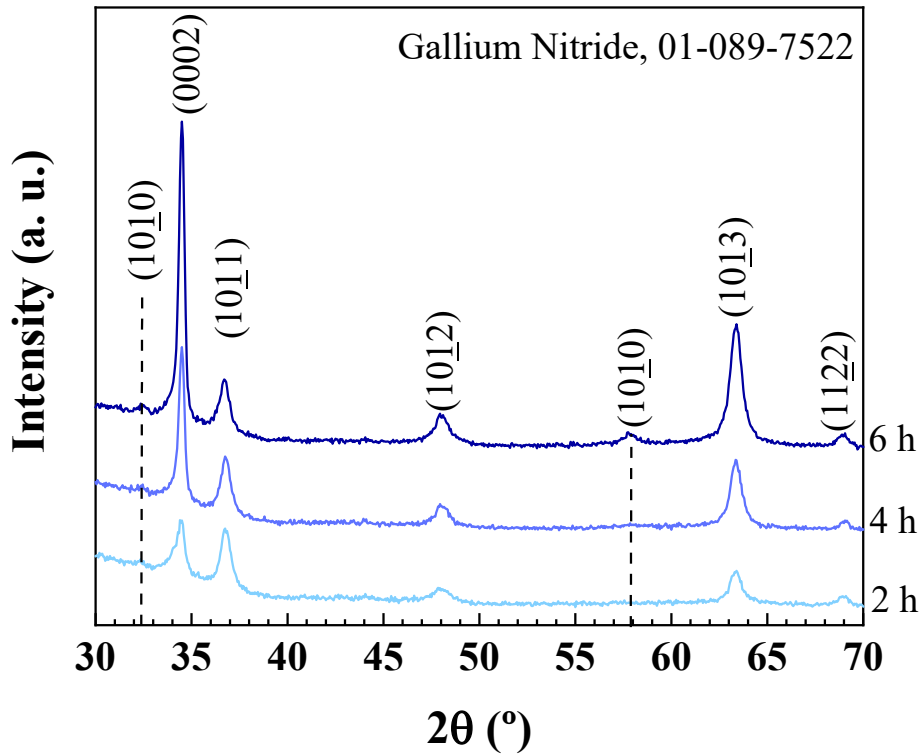
Figure 9: X-ray diffractograms of GaN thin films grown on glass substrate with different deposition times using magnetron sputtering technique.

Due to the same reasons, larger crystallites sizes and therefore an enhancement in the crystalline quality for films deposited for a long period of time was expected. **Table 4** shows ~42% of huge improvement in the quality occurs growing the film for 4 h instead of 2 h, but a slight enhancement (~2%) occurs from 4 h to 6 h. The thicker GaN film (deposited for 6 h) exhibited a decrease in the FWHM and an increase in D.

Table 4: FWHM (0002) and D for GaN/glass samples.

Deposition time (h)	FWHM (º)	D (Å)
2	0.540 ± 0.030	171 ± 9
4	0.316 ± 0.007	292 ± 7
6	0.311 ± 0.005	297 ± 5

Figure 10 shows the normalized diffractograms of GaN thin films grown on glass of the GaN (a) (0002), (b) (10$\underline{1}$1), and (c) (10$\underline{1}$3) peaks. According to the indexed GaN PDF card, the (0002), (10$\underline{1}$1), and (10$\underline{1}$3) plane positions estimated for the unstrained GaN are 34.57º, 36.84º, and 63.44º, respectively. A downshift is observed for all samples compared to the position's peaks of the unstrained GaN. This indicates the high defect density when grown on glass instead of Si.
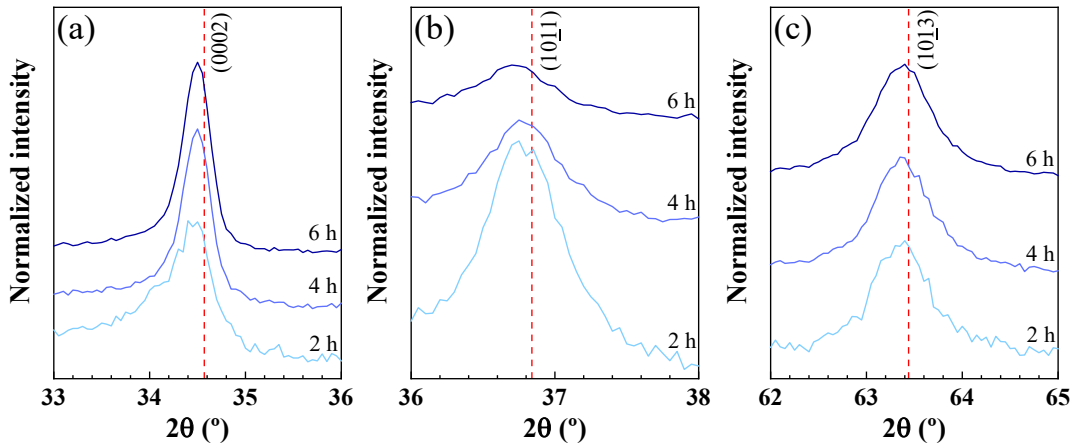
Figure 10: Expanded XRD in the interval (a) 33°-36°, (b) 36º-38º, and (c) 62º-65º, showing the main diffraction peaks of the GaN/glass samples and respective expected degree positions (vertical red dashed lines).

The shift seen in the plane's positions can be used to assess the quality of the films based on the expansion or contraction of the unit cell due to defects. The lattice parameters a and c were then calculated and displayed in **Figure 11.** As discussed earlier, it was anticipated that the GaN film grown for 6 h would have a lattice parameter closer to the unstrained structure. However, the sample grown for 4 hours demonstrated better results in contrast to the film grown on Si substrate. This comparison indicates that the c parameter values obtained are significantly higher than expected, while the a parameter

values are relatively close to the reference, with the exception of the sample grown for 6 h. This might be due to tensile strain on the film that provokes the expansion of the lattice parameter.
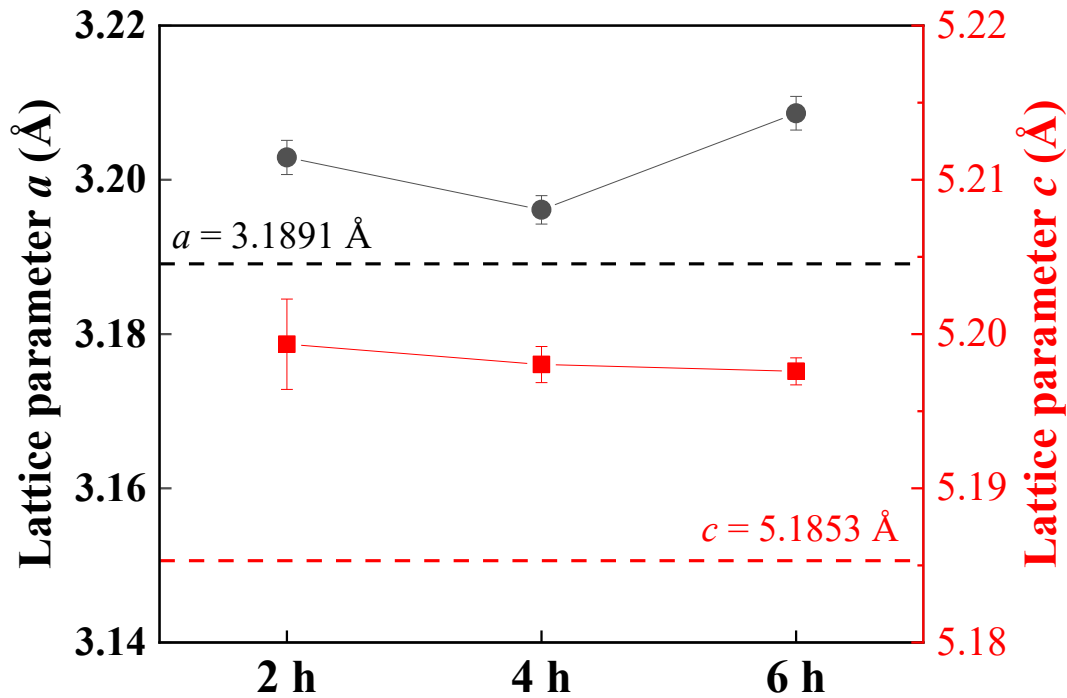

Figure 11: Structural parameters of GaN grown on glass for 2, 4 and 6 h. The black and red dashed lines identify the lattice parameters a and c, respectively, of the unstrained GaN according to the PDF card.

The reflection analyzed was the GaN (0002), as shown in **Figure 12**. The most prominent diffracted signal (0002) was observed in the center of the pole figure for GaN grown for 2 and 4 h, and it shows that the GaN films grow preferentially oriented along the out-of-plane (surface normal) direction, in these cases [132–134]. The (0002) planes for the sample's grown for 6 h exhibited an interestingly high degree of tilt. Overall, the spot in the center of the (0002) pole figure for all samples was largely dispersed, indicating a weakened preferred orientation along the surface normal [135].
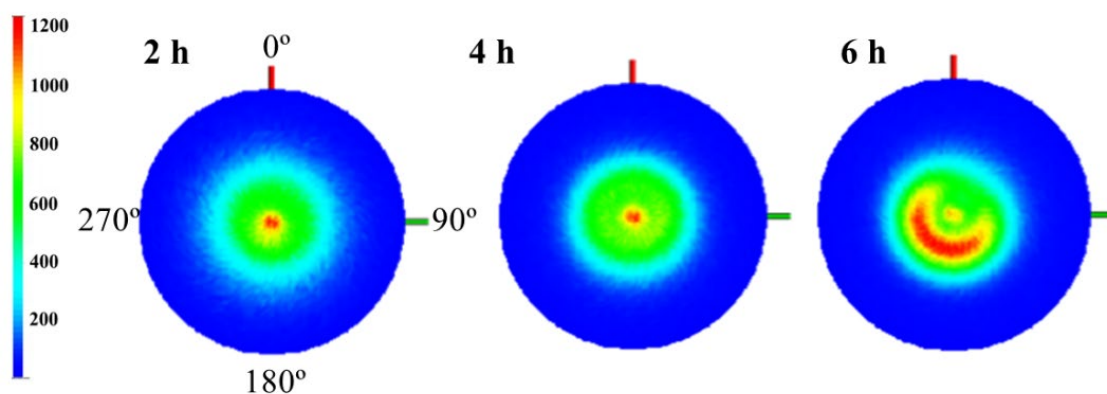
Figure 12: X-ray diffraction pole figures of GaN (0002) reflection of the sample grown on glass for 2 h, 4 h, and 6 h.

3.3.1.3. Raman spectroscopy of GaN/glass thin films

Figure 13 shows the Raman spectra of GaN/glass samples along with the spectrum of glass substrate as reference. As expected, as the sample thickness increases, there is a larger volume of material available for scattering of incident light. This results in a higher number of scattering events, leading to an overall increase in Raman signal intensity. Each sample displays the E_2 (high) and A_1 (LO) peaks in distinct spectral positions, which are representative of the wurtzite GaN phonon modes. There is also an overlapping shoulder between 500 cm^{-1} and 600 cm^{-1}, related to the glass substrate Raman spectrum.
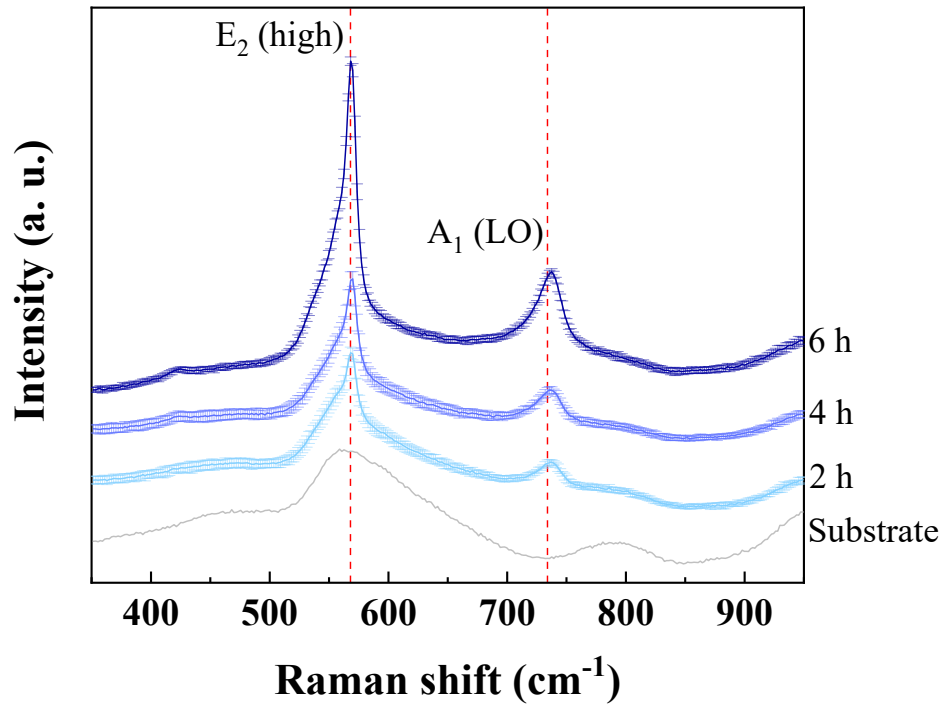
Figure 13: Raman spectra of GaN/glass samples grown at different deposition time. The red dashed lines are related to the phonon modes of unstrained GaN film.

The stretching and compression of atoms in the GaN lattice can be detected by the E_2 (high) phonon mode. A shift of the E_2 (high) phonon peak to lower or higher frequencies from its peak position in a high-quality and unstrained GaN film indicates compressive or tractive stress in the GaN films, respectively [138,139]. The positions of both E_2 (high) and A_1 (LO) modes are upshifted only by 1-2 cm^{-1} (

Table 5), with respect to the respective reported values of 734 cm^{-1} and 568 cm^{-1} for epitaxially grown films [140,141]. Therefore, despite being nanocrystalline and deposited on amorphous substrates, the Raman data show a good structural quality of the films, including a good optical-vibrational coupling.

Table 5: E_2 (high) and A_1 (LO) phonon frequencies observed for the GaN/glass samples and compared to other works.

Sample	E_2 (high) (cm^{-1})	A_1 (LO) (cm^{-1})	Ref
2 h	568.86	735.94	This work
4 h	569.24	735.12	This work
6 h	568.77	735.46	This work
GaN 350-700 ºC	560	728	[31]
GaN-NPs	568.4	735.6	[142]
Unstrained GaN	568	734	[140,141]

3.3.1.4. Scanning electron microscopy of GaN/Si(100) thin films

The thicknesses of GaN grown on Si were obtained using SEM cross-section images as shown in **Figure 14a**. These films adhered well on substrate without cracks and voids. **Figure 14b** shows the surface morphology of the thicker sample, which presented densely packed GaN flakes. It may be noted that initially sparse nuclei islands will be formed during the nucleation stage.
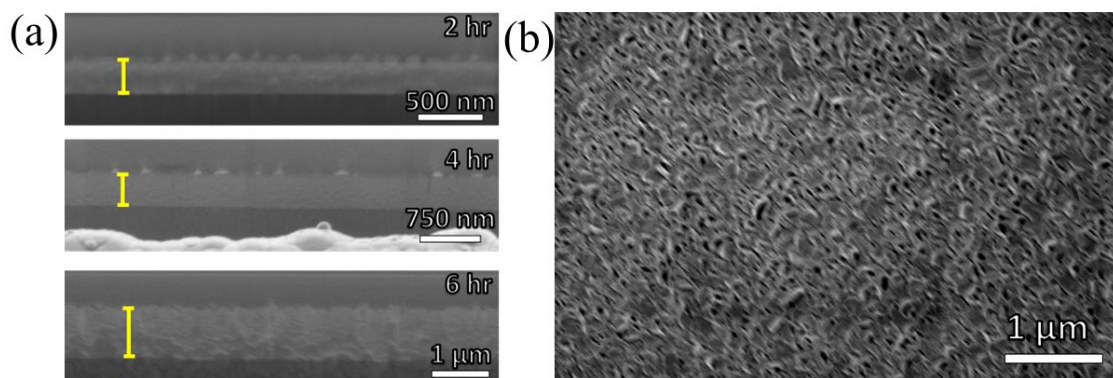
Figure 14: Cross-section images showing the thickness of GaN/Si grow for (a) 2h, 4h, and 6 h, and (b) SEM surface morphology of GaN/Si grown by 6 h.

Table 6 displays the thickness of each GaN film that was grown for three different deposition times (2 h, 4 h, and 6 h). When it comes to designing SAW devices that employ

thin films as the piezoelectric material, the thickness of the piezoelectric layer is a critical parameter. Previous research on AlN/diamond has investigated the impact of film thickness on the response of SAW devices [143,144]. In such cases, the k^2 and propagation velocity of the acoustic waves are determined by the film-thickness-to-wavelength ratio (H/λ). When H/λ is small, the SAW extends far into the underlying solid, and v approaches the large velocity value of the bare substrate, although k^2 is reduced due to the nonpiezoelectric nature of the substrate. Conversely, when H/λ is large, the SAW is mostly confined to the film region [143,144]. As a result, the design of GaN/Si-based SAW devices that operate at high frequencies and with low loss demands careful consideration of the film thickness, which must balance the other factors such as crystalline quality.

In this work, SAW resonators with periods of 1000 nm, 500 nm, and 100 nm were fabricated using GaN films of varying thicknesses, as listed in **Table 6**, to investigate the impact of piezoelectric film thickness on SAW response. The methodology employed in the microfabrication of the SAW resonators will be presented and discussed in **Chapter 7**.

The kH (2πH/λ) values for λ = 1000 nm were 2.07, 3.58, and 4.29 for films grown for 2 h, 4 h, and 6 h, respectively. The quality of the GaN film, and thus its piezoelectricity, depends on its thickness [143,144]. The experimental data presented illustrates the trade-off between selecting an appropriate thickness and maintaining the crystallographic quality of the piezoelectric film. Based on XRD and SEM results, and considering only the samples grown on Si, the sample grown for 6 h is expected to exhibit the best response for SAW sensor applications.

Table 6: Data on film growth and roughness of GaN films grown on Si.

Sample	2 h	4 h	6 h
Film thickness, SEM (nm)	329 ± 17	569 ± 30	1162 ± 36
RMS roughness, AFM (nm)	10.6	11.4	18.8
Sku sharpness, AFM	4.718	3.356	3.091
H/λ (1000 nm)	0.33	0.57	1.16
H/λ (500 nm)	0.66	1.14	2.32
H/λ (100 nm)	3.29	5.70	11.61

3.3.1.5. Atomic force microscopy of GaN thin films

Typical atomic force microscope images for the GaN films deposited for 2 h, 4 h, and 6 h are shown in **Figure 15.** The fine GaN grains of the sample are of uniform density with clear boundaries and a clean surface. There are few voids present in the samples, and the size of the crystals grow as the reaction time gets longer.
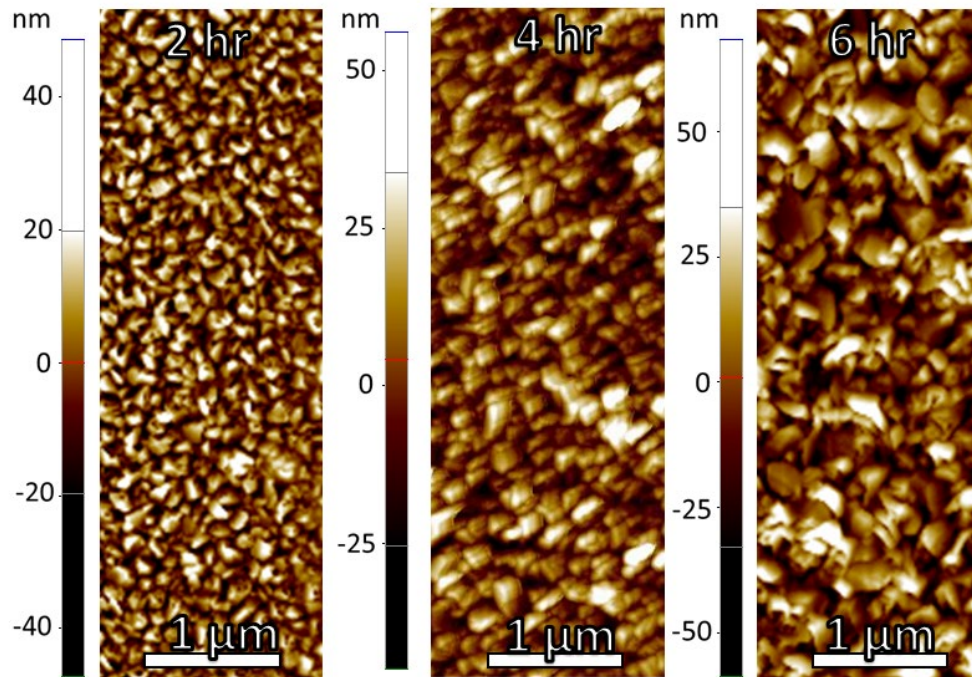
Figure 15: AFM images of the samples of the GaN films grown for 2 h, 4 h, and 6 h.

The RMS roughness values of GaN films are shown in **Table 6**. As the thickness increases, the RMS roughness increases. However, no significant change is observed from the sample deposited for 2 h and 4 h, but a significant huge increment in the roughness is observed for 6 h. The surface roughness of the RF-sputtered GaN film used in SAW resonators ranged from 10 to 18 nm, while the range for 0.5-2 µm-thick GaN films grown by MOCVD was 0.28–2.5 nm [80,145]. This is an expected result, since MOCVD is a technique well established to grow epitaxial GaN. However, considering the sputtered samples, the GaN films grown for 2 and 4 hours were much smoother than the thicker film.

Considering that the increment in RMS roughness in a factor associated with the sputtering system, then a practical limit of roughness might be attended. To meet the standard and practical demand for high-frequency SAW devices application, the surface

roughness of the GaN films should be less than 10 nm [146]. This is because SAW devices are extremely sensitive to the surface, which means that a rough surface would impact the SAW properties. Therefore, less roughness is better for this application. A uniform and dense GaN film, which satisfies this requirement, was successfully grown on a Si substrate for 2 hours.

3.3.1.6. Transmission electron microscopy of GaN thin films

Figure 16 presents the cross-sectional transmission electron micrographs. The image reveals a columnar morphology of the grown layers aligned with the preferential growth along the *c*-axis, which is in good agreement with the XRD results.

Furthermore, according to the **Figure 16**, it can be inferred that even though the films are polycrystalline, as seen in the XRD results, there is cohesion between the columns grown on Si(100), indicating that the film has a high grain density. Additionally, there is continuity in the grain boundaries, with growth of preferentially hexagonal crystalline planes in the (0002) plane family, as observed in the film's diffraction pattern (image indexed in **Figure 16**). This observation confirms the strong texture of the film, also evident in the pole figures and XRD patterns, where the *c*-axis of the crystallographic axis is preferably perpendicular to the film's normal plane [147].
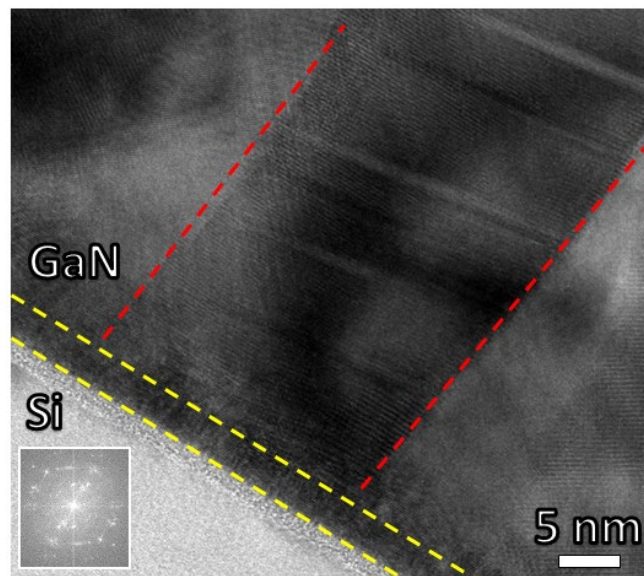
Figure 16: Cross-sectional TEM micrograph of GaN grown by 2 h on Si substrate at 300k of magnification. The fast Fourier transform (FFT) is inset. The red dashed line indicates the boundary of columnar growth, and the yellow dashed line denotes the intermediate growth phase between the film and the substrate.

In **Figure 16**, the yellow dashed lines highlight an intermediate region, indicating the disorganized growth of the film between the film and substrate. This area notably lacks texture. This phenomenon occurs due to the initial growth stage, where the mismatch between the film and substrate leads to randomly oriented nucleus, forming the intermediate layer. Additionally, this could be the reason for the appearance of other peaks in the XRD related to different growth directions concerning the plane of the substrate. Subsequently, beyond this nanometric layer, the crystallites preferentially align in the *c*-direction perpendicular to the substrate, while most columnar growth exhibits (0002) planes predominantly parallel to the substrate [147].

3.3.1.7. X-ray photoelectron spectroscopy of GaN/Si(100) thin films

XPS was used to determine the chemical surface properties of the GaN film deposited on Si(100). **Figure 17** shows the XPS survey spectrum of the GaN film.
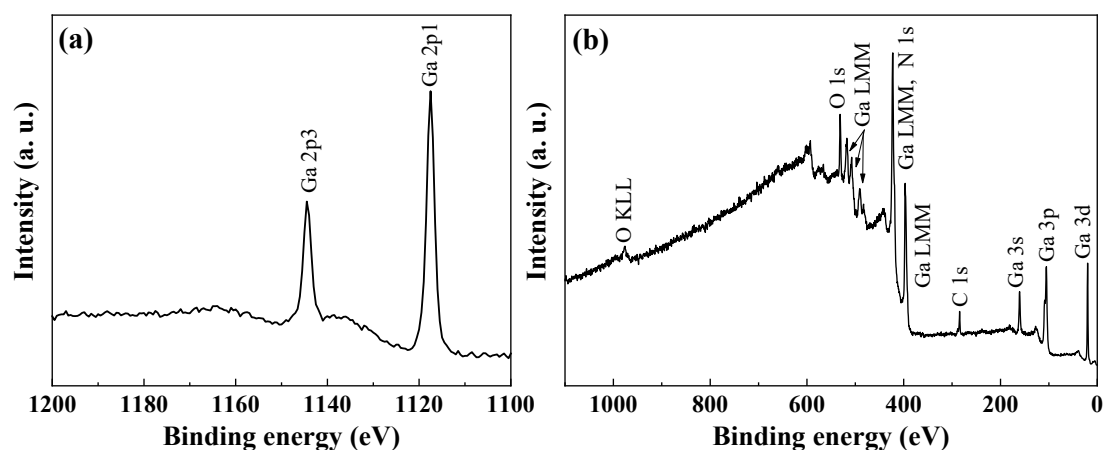
Figure 17: XPS survey spectrum of GaN thin film sputtering deposited for 2 h in the range of (a) 1200-1100 eV and (b) 1100-0 eV.

Figure 17 reveals the presence of impurities, including oxygen and carbon, in the GaN film. As wurtzite GaN surfaces are highly reactive to oxygen adsorption, the presence of oxygen and carbon traces in the GaN can be attributed to contamination and adsorption [148], or even the presence of functional groups such as: C=O and C–O [149]. However, based on the XPS spectra obtained from the surface and three consecutive layers (**Figure 18**), it can be observed that the carbon content is no longer present in the

GaN films from the second layer onwards, and only traces of oxygen are detected. This could be due to the presence of hydroxyl groups bonded to the film's surface (first layer) [150].
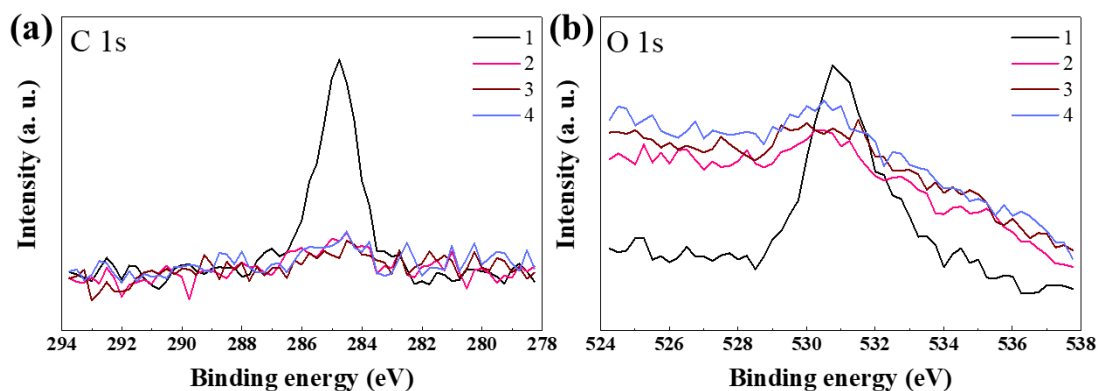
Figure 18: High resolution XPS scan of GaN/Si samples grown at 2 h at a region containing (a) C 1s, and (b) O 1s peaks taken at different layers. The label 1 represents the surface of the sample while 2, 3, and 4 are consecutive underneath layers measured after sputtering the film.

3.3.1.8. Electrical properties of GaN thin films

The I–V characteristics (**Figure 19**) were carried out to obtain the electrical performance and understand the device applicability. The electrical response was measured at an applied bias voltage from -1 V to +1 V. This measurement was conducted within this range to assess the quality of the electrical contact. The selected range is significantly higher than the voltage that will be applied to the SAW devices, as the objective is to ensure robustness and reliability of the electrical contact.

It was observed from **Figure 19** that the obtained I–V curves were linear and symmetrical, confirming that the carrier density in GaN is high [149]. Additionally, as expected, the obtained I-V curve exhibited the typical characteristics of a semiconductor I-V curve for GaN [151–153].

Figure 19 reveals that the as-deposited metallic Au contact to the GaN/glass exhibited a good ohmic contact. In other words, it means that the electrical contact exhibits a linear and proportional relationship between the applied voltage and the resulting current. Also, the resistance at the interface between the contact material and the semiconductor is low and relatively constant. This allows for efficient and unrestricted flow of current, without significant voltage drop or non-linear behavior [154]
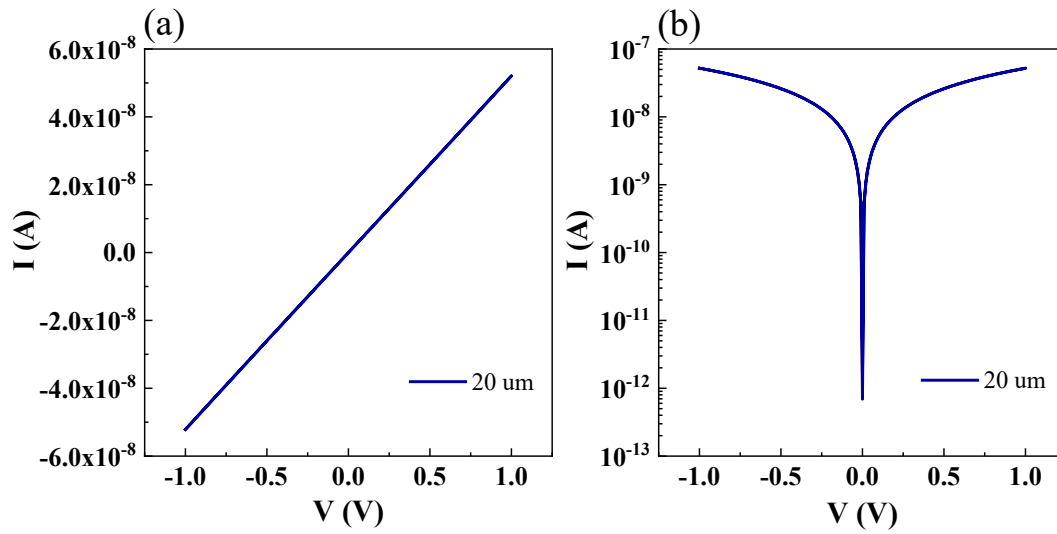
Figure 19: The forward and reverse (a) I-V curve and (b) log I-V plots of GaN/glass grown at 2 h.

The resistance (R), obtained by taking the inverse of the slope of the I-V curve, was determined through a linear fit of the experimental data (R = 1.92 x 10^7 Ω). By considering that resistivity is typically given in Ω.cm and is calculated as the product of resistance, area (A = w x t = 3.29 x 10^{-11} m^2), and length between the two contacts (L = 20 x 10^{-6} m), the resistivity of GaN was found to be approximately 3 kΩ.cm. Monish et al. [155] showed that the resistivity of sputtered GaN can range from 100 kΩ.cm to 1 mΩ.cm, depending on the doping level. They noted that intentional or unintentional doping introduces carriers in the valence or conduction band, enabling the conduction of electricity even at voltages below the semiconductor's band gap. In the context of SAW devices, it is crucial to transform the electrical voltage between the IDTs into mechanical deformation within GaN, rather than electric current. Considering the relatively high resistivity value obtained, it indicates a low concentration of electronic carriers and defects [155,156]. This low carrier concentration facilitates the operation of SAW devices. This result also allows us to confirm if the metallic pad is well adhered and if the transfer of energy is efficient [151–153].

3.4. Conclusion

The GaN thin films were successfully deposited by magnetron sputtering. The GaN films were polycrystalline and exhibited a wurtzite crystal structure with preferential

orientation in the c-direction, as confirmed by XRD, Raman, and TEM measurements. The produced films exhibited traces of carbon and oxygen, primarily as adsorbates that could be easily removed. It was observed that the GaN films grown for 6 hours on Si and glass exhibited better crystalline quality compared to the samples grown for 2 and 4 hours. Considering the values of H/λ, it is expected that the sample grown for 6 hours would demonstrate the best performance in SAW applications. However, the GaN film grown for 6 hours exhibited the highest RMS value among the studied samples, which decreases the quality of the sample and may negatively affect the SAW performance when using this sample as the base piezoelectric material. The electrical results showed a satisfactory ohmic contact between the IDTs and GaN film. Moreover, the relatively high resistivity of films grown by sputtering is an important factor for electromechanical coupling coefficients and it is expected to fabricate SAW devices. This comprehensive study is of great importance in obtaining high-quality sputtered samples with suitable characteristics for SAW device applications and to enable the development of SAW devices operating at high frequencies.

CHAPTER 4. Graphene by Flash Joule Heating

This chapter discusses the methodology used to obtain CBFG and the corresponding results that support its application as a sensing layer in SAW devices.

This chapter is part of a research article entitled "Flash Graphene and Poly(O-Methoxy Aniline) for the Composition of a Solvent-Based Conductive Ink" published in the Surfaces and Interfaces (Impact Factor (2023) – 6.2)[157]. As per Elsevier subscription guidelines, authors maintain the privilege of incorporating the article into a thesis, as long as it remains unpublished for commercial purposes.

4.1 Synthesis of graphene by flash Joule heating system

The FJH technique is a method of rapidly heating a material using high-intensity electrical pulses [158–162]. It involves passing a high-current pulse through a conductor to generate intense heat within a very short duration. The conductor in this case is the carbon material (carbon black) used as precursor, and the conduction is linked with the electrodes using copper wool and graphite spacers, the illustration will be shown on the methodology section.

Briefly, the process uses a high-voltage capacitors bank which is charged to store a significant amount of electrical energy that is released in a very short duration, typically in the range of microseconds to milliseconds. The stored electrical energy is rapidly discharged through the conductor, creating a high-intensity current pulse. The current passing through the conductor generates heat due to the resistance of the material. The controlling of the current pulse is given by the duty cycle. Then, the resistance of the conductor causes the electrical energy to convert into heat. This process is known as Joule heating or resistive heating. The heating effect is localized within the conductor, rapidly raising its temperature. The high-intensity current pulse results in a rapid increase in the conductor's temperature. The duration of the pulse is carefully controlled to prevent excessive heating that could lead to material damage, vaporization, or even explosion. After the pulse, the material reaches a state of thermal equilibrium with its surroundings, retaining the elevated temperature [158–162].

The FJH process eliminates the need for furnaces, solvents, or reactive gases. Moreover, the resulting yields depend on the carbon content of the source material [158,162]. For instance, when carbon black is used, the yields can vary between 80% and 90%, while maintaining a carbon purity level exceeding 99%.

In 2020, Luong et al. [162] demonstrated the FJH process as a low-energy bottom-up synthesis method for turbostratic GR derived from organic sources. Turbostraticity occurs with the rotational misalignment of GR layers, significantly reducing the interlayer π-π interactions compared to the ordered stacking (AB stacking) in graphite, leading to several enhanced properties. The reduced coupling facilitates easier exfoliation into high-quality graphene flakes, ensures better dispersibility in solvents and binders, resulting in a more homogeneous conductive ink, and improves electrical conductivity due to increased anisotropy. This anisotropy, arising from the rotational disorder, enhances electrical conductivity by allowing different in-plane and out-of-plane behaviors. Additionally, the authors managed to overcome a significant limitation of the bottom-up approach, which had hindered the production of gram-scale quantities of GR within a short timeframe. They reported a technique that utilizes high-voltage electric discharge and rapidly elevates the temperature of the carbon source to levels exceeding 3,000 K in less than 100 ms. As a result, the amorphous carbon was transformed into turbostratic GR, facilitating the dispersion of flash GR in several solvents.

One limitation of this method is that the as-prepared sample is in a powdered form, necessitating the production of an ink for deposition onto specific surfaces [158,162]. However, the numerous advantages mentioned outweigh this minor drawback, reinforcing the material's property that is significance in SAW sensor applications.

4.2   Materials and Methodology

Carbon black (C, Cabot Corporation, CAS n° 1333-86-4) was used as precursor to produce CBFG.

4.2.1   Synthesis route of flash graphene

A capacitor-based 0.624 F FJH system was used to provide electrical energy to the flash sample. The flash system utilized a 1 kHz scale pulse width modulation system to control the current discharge with a duty cycle sequence of 10% for 1 s, followed by 20% for 0.5 s, and finally 50% for 5 s, all mediated by a customized LabVIEW program.

1.5 g of carbon black was added to the inner center of a quartz tube (inner diameter of 16 mm, outer diameter of 20 mm, and length of 6 cm), and copper wool was added to each side of the inner tube to improve the electrical connection for Joule heating during the reaction. The Cu wool was compressed with graphite electrodes (diameter of 16 mm

and length of 3 cm). The copper wool was touching the sample, and the graphite spacers were connected with the capacitor banks (as shown in **Figure 20a**). A 0.72-inch wide and 1-inch-long passivated stainless-steel compression spring was wrapped around the outside of the quartz tube to reinforce the tube against the reaction pressure buildup. (as shown in **Figure 20**).
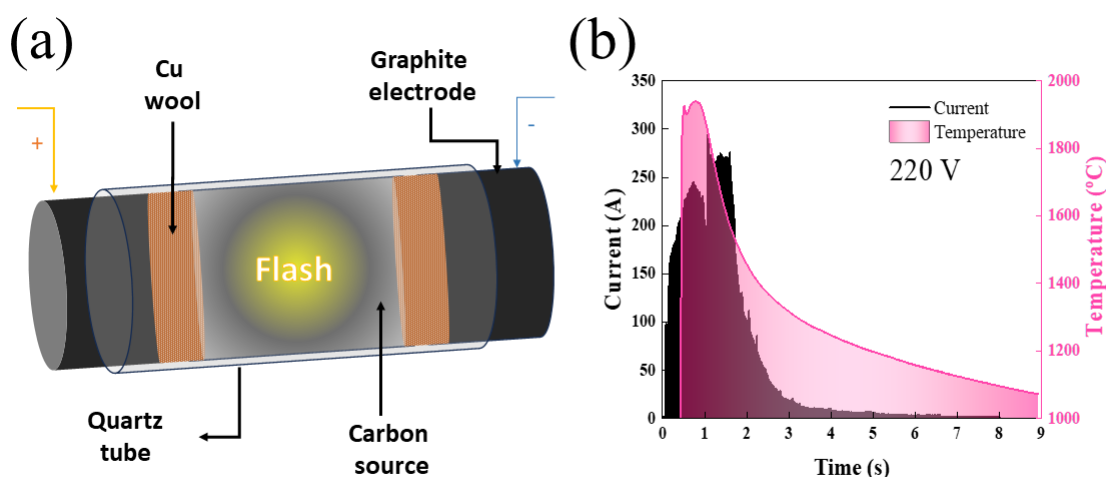
Figure 20: (a) FJH system set up for CBFG synthesis. (b) Current recorded during the FJH process using the initial voltage of 220 V.

The FJH station can induce reactions with both high current and short duration, as well as low current and long duration. **Figure 20a** provides a simplified schematic of the FJH system. Initially, a low-current with an initial voltage of 100 V is applied to the carbon black powders inside the tube, triggering long-duration reaction (~7 s). This flash, associated with the carbonization process, does not emit visible light. In the second step an initial voltage of 150 V is applied, and carbonization occurs, resulting in an increase in current due to decreasing powder resistance. Following carbonization, graphitization is achieved by charging 220 V, resulting in a maximum current through the sample of approximately 295 A, displaying a homogeneous glow with a discharge time of ~5 s (**Figure 20b**). The working parameters, current, and temperature values are displayed in **Table 7**.

Table 7. FJH conditions employed to produce CBFG powders.

Voltage (V)	R_i (Ω)	Duty Cycle	I_{max} (A)	T_{max} (°C)
100	2.3	10% 1 s, 20% 0.5 s, 50% 5 s	-	n.d.
150	-	10% 1 s, 20% 0.5 s, 50% 5 s	-	n.d.
220	-	10% 1 s, 20% 0.5 s, 50% 5 s	295	1941

n.d.: not detected; below the minimum detected by the equipment.

4.2.2 Characterization

4.2.2.1 Raman spectroscopy of CBFG powders

Raman spectra were measured using Renishaw Raman microscope equipped with a 532 nm laser and LiveTrack software to automatically adjust focus between spectra. The laser was focused by a 50x objective lens, exposed by 1 s during 3 accumulations, and a filter of 1% was used to avoid burning the material. The Raman spectra were recorded in the range of 1200-3000 cm^{-1}. For each CBFG sample, 200 measurements were taken across a square 1000 µm2 grid of the sample, and then averaged together using custom Python software.

4.2.2.2 X-Ray diffraction of CBFG powders

The X-ray powder diffraction data were collected using a Rigaku SmartLab II diffractometer in a Bragg–Brentano configuration with a Cu Kα radiation (λ = 1.5406 Å) source operating at 40 kV and 44 mA. Measurements of each system were performed in the 2θ range of 10-80º for the CBFG samples with a scan width of 0.02º per step, a scan rate of 1º per min, and a step size of 0.05°. The sample was ground with a mortar and pestle to guarantee homogeneity, with no exposure to solvent.

4.2.2.3 X-ray photoelectron spectroscopy of CBFG powders

XPS data were collected (PHI Quantera SXM scanning X-ray microprobe) using a base pressure of 5×10^{-9} Torr. A 0.25 eV step size and a pass energy of 140 eV were used for recording the survey spectra. A step size of 0.1 eV and a pass energy of 26 eV were used for recording the elemental spectra. All the XPS spectra were corrected using the C 1s peaks (284.6 eV for C=C and 284.8 eV for C-C) as reference.

4.2.2.4   Scanning electron microscopy of CBFG powders

The as-prepared CBFG-based powders were characterized by scanning electron microscopy using an FEI Quanta 400 ESEM FEG system at a voltage of 20 kV with a working distance of 10 mm. The samples did not require any extra treatment.

4.2.2.5   Transmission electron microscopy of CBFG powders

Annular dark field scanning transmission electron microscope (ADF-STEM) images were taken using the FEI Titan Themis (S/TEM) system, operating at 300 keV. To prepare the powder samples, 300 μL of a solution containing 1 mg of sample per 1 mL of ethanol was drop-cast onto a Cu/lacey carbon TEM grid (Ted Pella). The grid was then dried at 80 °C on a hotplate for an hour, followed by overnight vacuum drying.

4.2.2.6   Porosimetry of CBFG powders

Brunauer−Emmett−Teller (BET) surface area analysis was carried out using a Quantachrome Autosorb-iQ3-MP/Kr BET surface analyzer. The BET analysis was conducted using N_2 gas at 77.35 K. Before analysis, the samples were degassed for 5 h at 200 °C under a high vacuum.

4.3   Results and discussion

4.3.1   Characterization

4.3.1.1   Raman spectroscopy of CBFG powders

According to the spectra of CBFG in **Figure 21**, CBFG was successfully synthesized. The proposed mechanism for synthesizing this type of CBFG using an FJH system relies on ultrafast electrical discharge that heats the material to temperatures exceeding 3000 ºC, allowing C-H bond homolysis to break the polymer chains and yield thermodynamically favored products [163]. As a result, the intermediate products, polyaromatic hydrocarbons, can be considered as the nucleation sites for the eventual formation of turbostratic CBFG sheets. These sheets can expand through the aromatic rearrangement of other mobile carbon species [162,163].
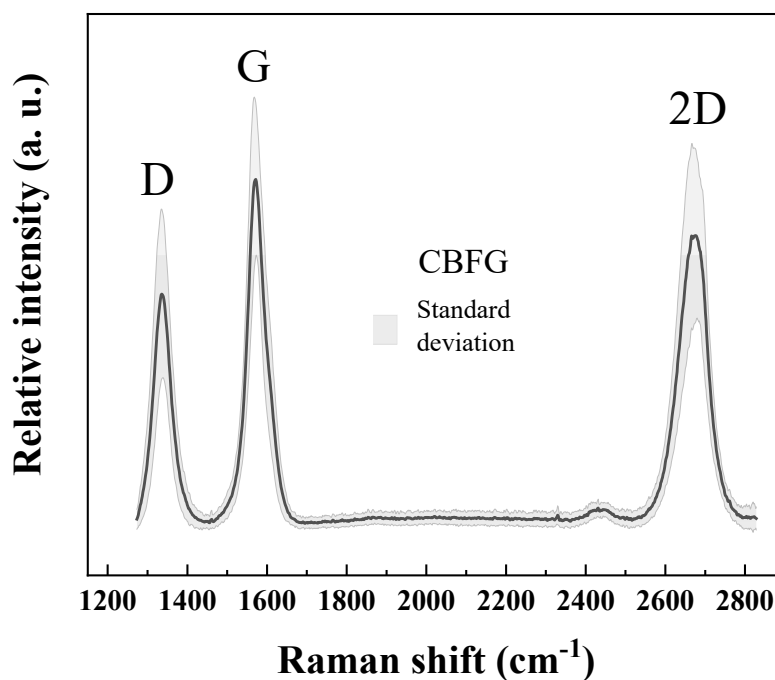
Figure 21: Raman spectra of CBFG. Shaded area represents the standard deviation of 200 spectra map.

Figure 21 depicts three prominent Raman-active phonon modes commonly observed in GR-based materials: D (~1350 cm^{-1}), G (~1580 cm^{-1}), and 2D (~2700 cm^{-1}) [162,164]. The D peak serves as an indication of structural defects within the sample. The G band corresponds to the stretching of bonds between pairs of sp^2 atoms in rings and chains. Both the D and G bands are consistently present in all poly-aromatic hydrocarbons. The 2D band is a second-order overtone of the D band, and it originates from the interaction between electronic excitations and lattice vibrations, providing information about the number of GR layers and stacking order.

The presence of the D peak is typically forbidden by selection rules, yet it often appears due to disruptions in symmetry, such as armchair edges or point defects. Thus, D peak is present in turbostratic CBFG, and it indicates structural defects and disorder within its carbon lattice. Turbostratic CBFG's disordered nature is characterized by a high density of defects, grain boundaries, and other imperfections. These structural irregularities cause increased scattering of incident laser light, consequently activating the D peak in the Raman spectrum [165,166].

To assess the quality of the prepared CBFG powder, it is necessary to analyze the D/G and 2D/G peak intensity ratios. A high D/G intensity ratio often indicates the formation of low-quality GR, characterized by low crystallinity, small sheet size, and a high concentration of defects [158,162]. CBFG exhibits a relatively low D/G ratio (0.63 ± 0.07) and a high 2D/G ratio (0.88 ± 0.06) suggesting high quality GR, and FWHM of 2D of 53.31 ± 1.61 cm^{-1}.

In the presence of multilayer GR, fitting the 2D peak with a single Lorentzian function becomes challenging due to the presence of multiple phonon levels. In contrast, a single Lorentzian profile indicates a single layer GR or demonstrates how the electronically decoupled nature of turbostratic CBFG sheets can spectroscopically resemble monolayer GR. In **Figure 22**, the collected Raman spectrum demonstrates a good Lorentzian fitting with an R^2 value above 0.99, indicating the absence of AB stacking and a material with only a few stacked layers [160,162,167]. Therefore, the turbostratic nature of the synthesized CBFG was observed through the fitting of a single Lorentzian function to the 2D peak (**Figure 22**).
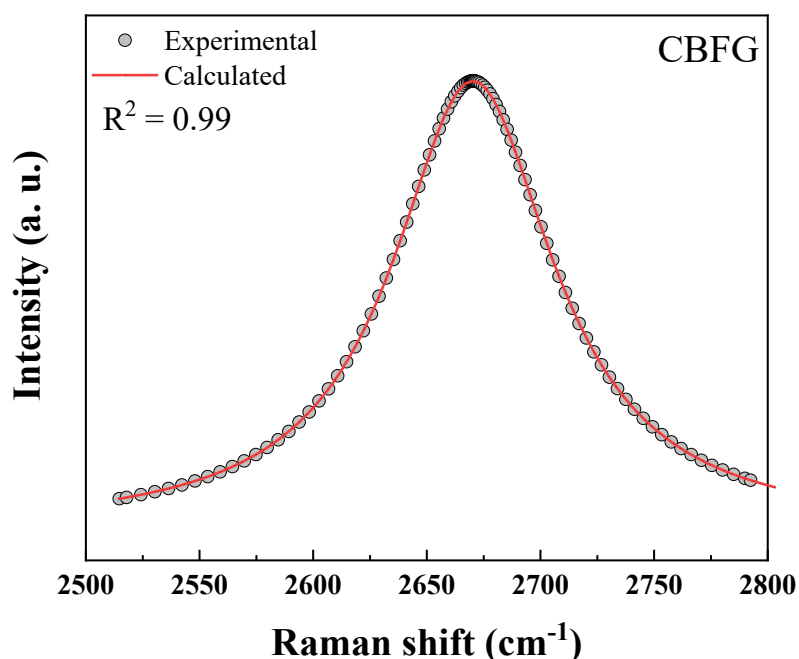
Figure 22. The Lorentzian fitting of the Raman spectrum from the average spectra for CBFG (actual spectrum dashed circles, Lorentzian fit solid red line).

The system's rapid cooling resulted in the formation of kinetically stable turbostratic CBFG, as opposed to GR with an AB-stacked morphology [162,167]. This is supported by the presence of the TS_1 (1869 cm^{-1}) and TS_2 (2015 cm^{-1}) bands in the Raman spectrum, confirming the attainment of turbostratic CBFG (**Figure 23**).
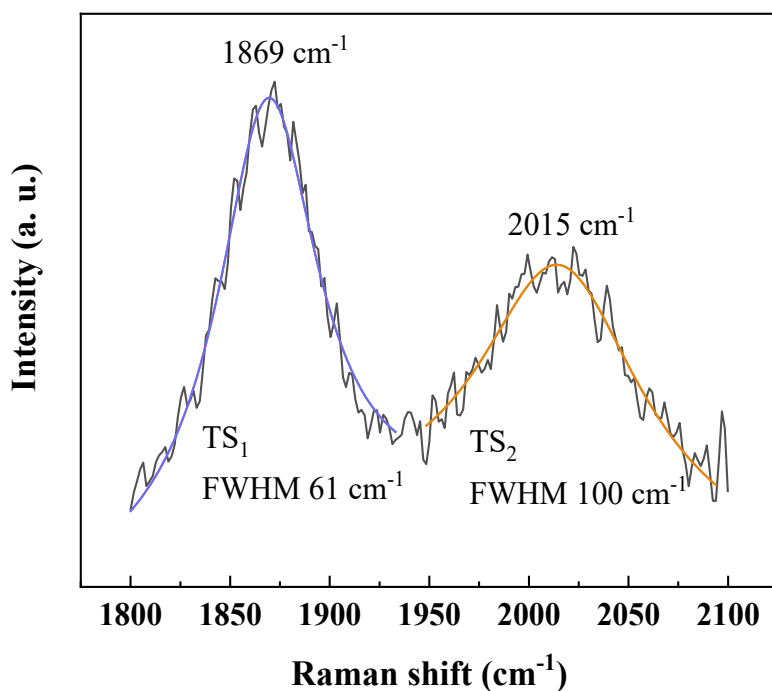
Figure 23: (a) Turbostratic peaks in the Raman spectrum of CBFG. The overlapped smooth lines represent the Lorentzian fitting. The blue one is characteristic of TS_1 and showed the R-squared equal to 0.978 and the orange one is characteristic of TS_2 and showed the R-squared equal to 0.932. These Raman bands are exhibited in the presence of turbostratic GR, and the fits indicate the high quality of the CBFG.

The peak observed at 1865 cm^{-1} results from the merging of in-plane transverse acoustic and longitudinal optic modes, identified as the TS_1 band, and the peak at 2021 cm^{-1} arises from the consolidation of in-plane transverse optic and longitudinal acoustic modes, known as the TS_2 band [165].

The presence of TS_1 and TS_2 bands in the Raman spectrum indicates rotational disorder and spectroscopic decoupling between the GR layers, signifying the absence of graphitic stacking in turbostratic CBFG [159,160,167,168]. The observation of these peaks, along with the multifunctional 2D peak, confirms that the as-prepared CBFG does not possess graphitic stacking.

In turbostratic CBFG, the interlayer spacing between GR sheets is increased, and the sheets are rotated relative to each other. Consequently, the intensity of the 2D peak in CBFG increases with the number of GR layers. However, even with an increased number of layers, CBFG retains its desirable properties as a 2D material, as the enlarged interlayer spacing hinders interlayer electron transport.

The disordered arrangement of turbostratic CBFG layers makes it easier for them to exfoliate quickly when mixed and ensures better uniformity during coating and composite production [162,169]. Although these layers are randomly stacked, they still maintain their two-dimensional properties [162,163,170,171]. In other words, what defines a material as 2D is not its physical dimensions or the number of atomic layers, but rather its properties, particularly electronic properties. A 2D material is characterized by high anisotropy in electron mobility. Turbostratic CBFG possesses the highest level of anisotropy, remaining fully 2D even with multiple layers [163,170–173].

Hence, the synthesis of CBFG through FJH provides a straightforward and cost-effective method for mass production. This approach produces GR with good dispersibility which makes this material suitable for ink production and further deposition on the active area of a SAW device to act as sensing layer.

4.3.1.2 X-Ray diffraction of CBFG powders

Figure 24a shows the XRD patterns of the CBFG. XRD technique allows the analysis of turbostratic CBFG sheets arrangement. These sheets can randomly shift and rotate along the normal axis of the GR layers. As a result, the spacing between layers and the shape of the atomic layers undergo changes. When the crystal size decreases or the GR sheets become curved, the diffraction angle of the (002) peak, typically seen around 26.7º, decreases [158]. Additionally, the FWHM of the (002) peak increases [168]. **Figure 24b** shows this phenomenon, and it reveals complete conversion to crystalline GR, evidenced by the prominent (002) peak at 26.06° with an interlayer spacing of 3.41 Å. This downward shift of the (002) peak compared to pristine GR indicates an expansion in interlayer spacing of the CBFG [160].
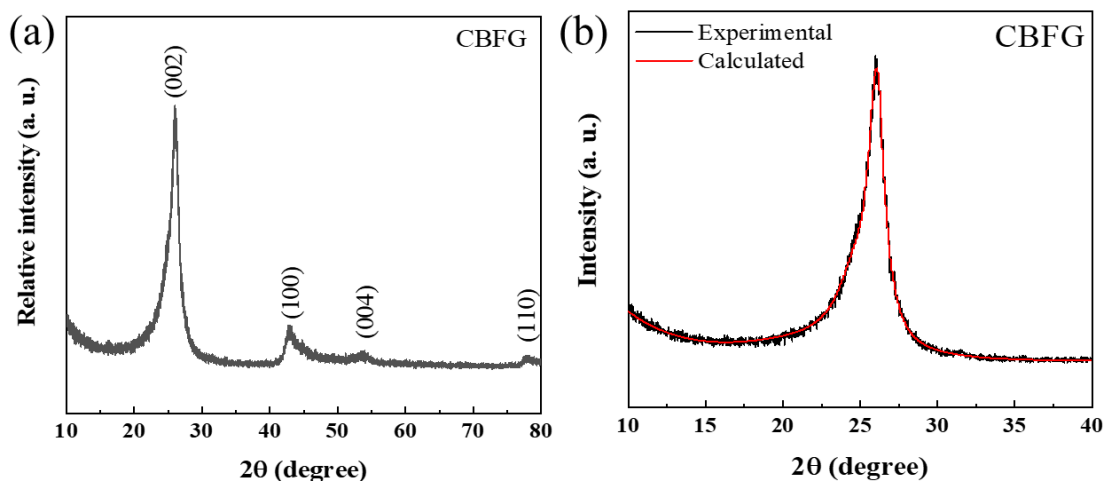
Figure 24: XRD pattern of the CBFG samples, and (b) expansion of the region between 24 and 28º.

By comparing turbostratic CBFG to graphite nanoplatelets, an increase in the FWHM of the (002) peak is observed, as well as an asymmetric shape towards lower diffraction angles, indicating a broader range of stacking environments compared to graphite. This suggests a smaller crystal size and/or curvature of the GR layers. A (100) peak at $2\theta = 42.8°$ corresponds to the in-plane interatomic spacing. The FWHM of this peak indicates large in-plane sheet sizes [162]. Additionally, the typical (100) reflection displays an asymmetrical shape with a noticeable tail on the high Bragg angle side, which indicates the absence of ordered stacking of basal planes and confirms the presence of a turbostratic structure [160].

Calculations using Bragg's law and Scherrer's equation were performed to determine the size of the flakes and the average spacing between layers. The values can be found in **Table 8**.

Table 8. Analysis of the diffraction angle of the (002) peak from the XRD pattern.

Sample	CBFG
2θ (degree)	26.06
FWHM (degree)	1.49
d_{002} (Å)	3.41
Thickness (Å)	60.81
Layer Number	~18

The sample presented an interlayer distance around 3.41 Å. This is significantly increased from the 3.35 Å that occurs in bulk AB-stacked graphite [174]. The increased interlayer spacing results from the decreased π-π stacking interactions, which are disrupted by the rotational disorder that occurs in turbostratic GR. This weakening of π-π stacking interactions, resulting in easier exfoliation of bulk turbostratic CBFG [167].

4.3.1.3   X-ray photoelectron spectroscopy of CBFG powders

To analyze if the CBFG presented any impurity from its precursor, the purity was analyzed using XPS. As shown in **Figure 25** only carbon is presented in the as-prepared CBFG.
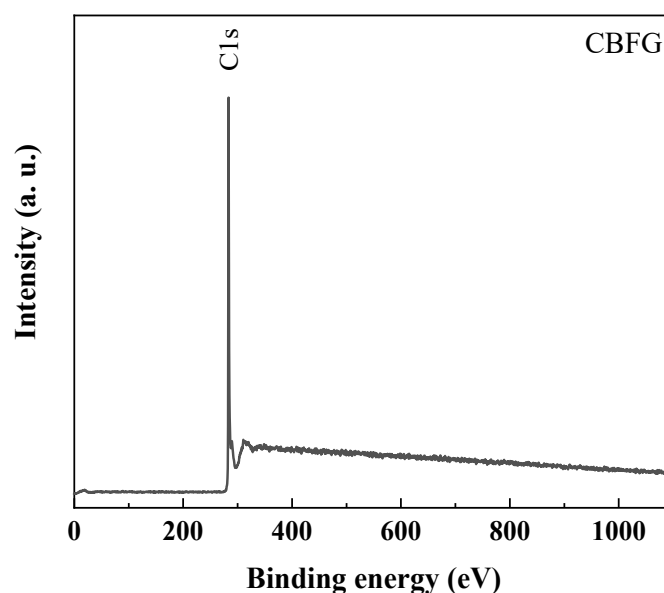
Figure 25: Wide survey XPS spectra of CBFG.

No extra treatment was performed, which is an indicative of the highly pure nature of the turbostratic CBFG with 100% carbon of atomic concentration composition.

4.3.1.4   Scanning electron microscopy of CBFG powders

Figure 26a shows wrinkled and overlaid CBFG layers, while **Figure 26b** presents non-orientated wrinkled CBFG. This rough surface morphology will result in a high surface area, as shown further.
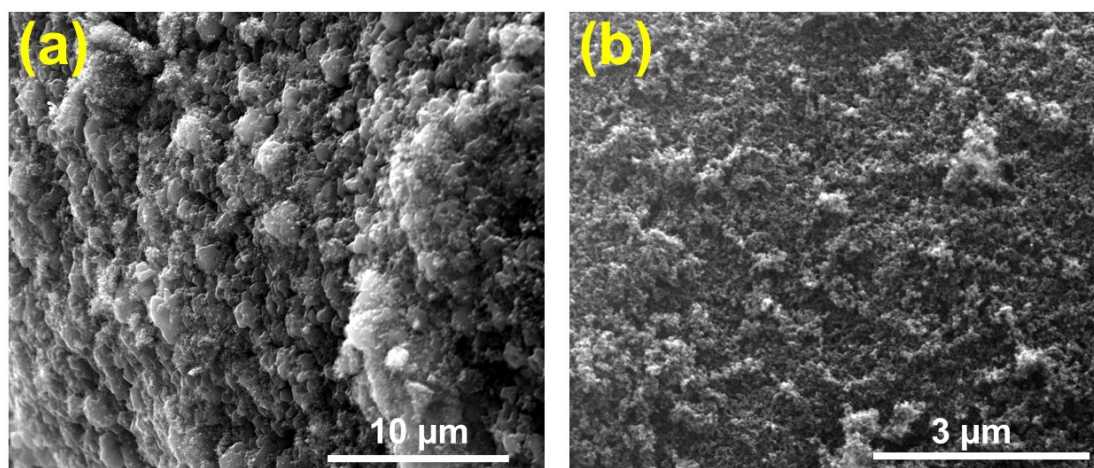
Figure 26: SEM images of CBFG powders with scale bar of (a) 10 µm and (b) 3 µm.

4.3.1.5   Transmission electron microscopy of CBFG powders

According to TEM image shown in **Figure 27a**, CBFG exhibits crystallinity, which is proved by the presence of the lattice fringe of the CBFG and the sheet dimensions revealed sizes up to approximately 20 nm. The TEM image also shows a few layers of wrinkled CBFG arranged in a turbostratic layering configuration. **Figure 27b** displays the FFT, revealing several distinct Bragg spots, representing the misalignment between CBFG sheets in the [002] stacking direction, confirming the turbostratic nature of the CBFG [175].
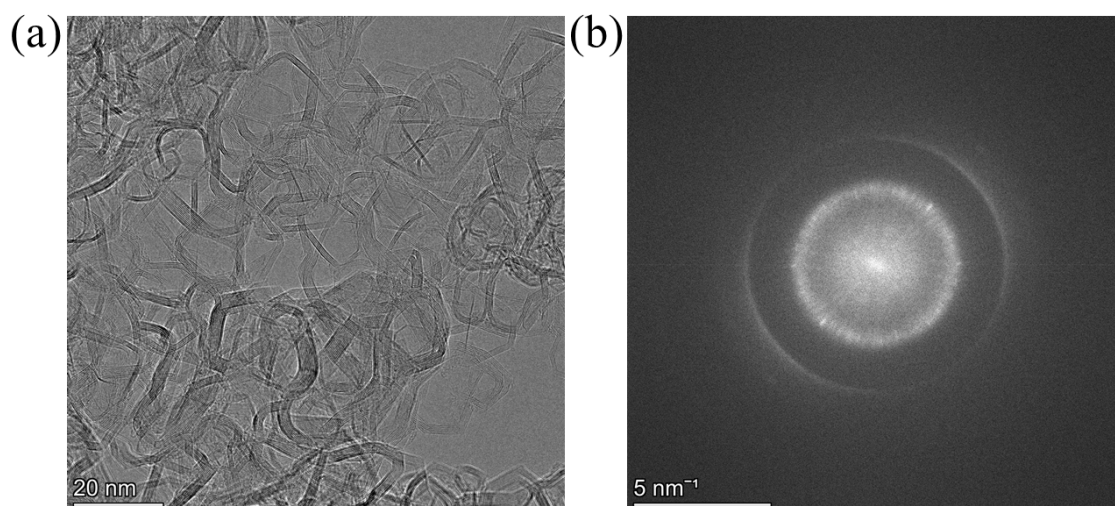
Figure 27: (a) TEM images of synthesized CBFG, and (b) a FFT of the region in (a).

4.3.1.6 Porosimetry of CBFG powders

The porosity and surface area of the CBFG powders were evaluated using the BET analysis. Isotherm curves (**Figure 28a**) indicate that the surface area of CBFG can be as high as ~293 $m^2 g^{-1}$. High surface area is known to positively impact sensing and adsorption capabilities of adsorbents. Considering the high adsorption of the CBFG, the uptake of methylene blue (MB), a common pollutant, was tested. CBFG exhibited high adsorption performance, removing 100% of the pollutant after 20 minutes in an aqueous system (**Figure 28b**).
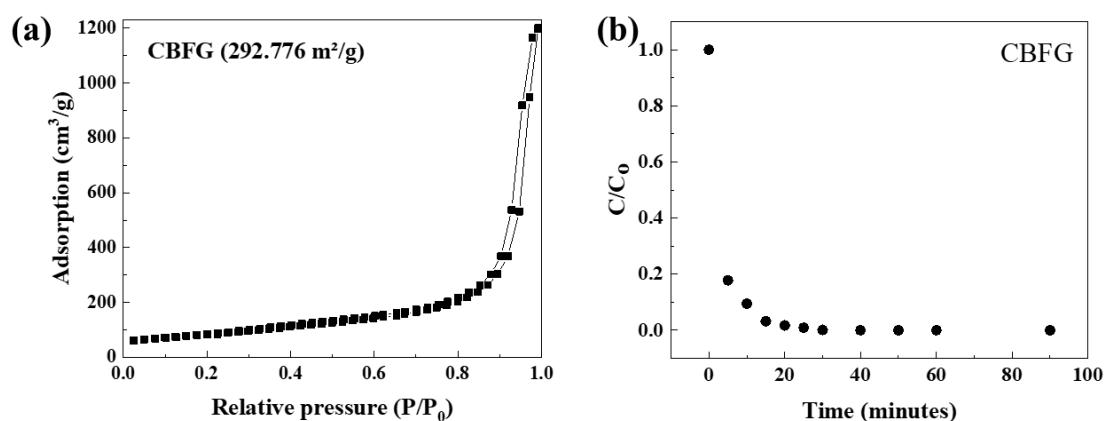
Figure 28: (a) BET isotherms for CBFG powders. The dashed black lines correspond to the BET isotherms of CBFG (b) Variation of the concentration of the MB vs time during adsorption on CBFG powders.

4.4 Conclusion

According to XRD and Raman measurements, we successfully synthesized CBFG using an ultrafast and solvent-free FJH method. XPS analysis proved the high purity of the CBFG powders (100% C). SEM and TEM images confirmed that the as-prepared CBFG is composed of turbostratic sheets of CBFG. Spectroscopically, these turbostratic sheets behave optically like monolayer GR. CBFG can easily disperse in an ethanol solution and form stable, concentrated slurries due to its turbostratic nature. The prepared CBFG exhibited a high surface area (~293 $m^2 g^{-1}$) and proved to be an excellent adsorbent for MB dye (R% = 100% after 20 min). The ease of synthesis, along with these remarkable properties, makes CBFG an ideal material for composing conductive ink. Moreover, the good dispersibility of the synthesized materials renders them suitable for

ink production and subsequent deposition as a sensing layer on the active area of a SAW device.

CHAPTER 5. Poly(o-methoxyaniline) by oxidative polymerization

This chapter discusses the synthesis of POMA and examining the advantages and limitations of employing this polymer as a sensing layer.

This chapter is part of a research article entitled "Flash Graphene and Poly(O-Methoxy Aniline) for the Composition of a Solvent-Based Conductive Ink" published in the Surfaces and Interfaces (Impact Factor (2023) – 6.2)[157]. As per Elsevier subscription guidelines, authors maintain the privilege of incorporating the article into a thesis, as long as it remains unpublished for commercial purposes.

5.1. Synthesis of poly(o-methoxyaniline) by oxidative polymerization

POMA is a conducting polymer that can be synthesized through oxidative polymerization. The process begins with the selection of the monomer, o-methoxyaniline (o-anisidine), an aniline derivative with a methoxy (CH_3O-) group attached to the ortho position of the aromatic ring. During oxidative polymerization, an oxidizing agent such as $(NH_4)_2S_2O_8$, ferric chloride ($FeCl_3$), or potassium dichromate ($K_2Cr_2O_7$) is used. This oxidizing agent initiates the reaction by oxidizing the o-anisidine monomer, leading to the formation of radical cations, which are positively charged radicals on the monomer units. These radical cations are highly reactive and undergo coupling reactions with neighboring monomer units. This coupling reaction forms covalent bonds between the units, resulting in polymer chain growth. The radical cations act as intermediates in this chain propagation process [57,114,176,177].

POMA exhibits interesting properties such as electrical conductivity, which can be tuned by varying the polymerization conditions and dopants. It also possesses good stability and can be synthesized in various forms including films, and nanoparticles. These properties make POMA suitable for a wide range of applications, including sensors, actuators, electronic devices, and coatings [40,108,178].

5.2. Materials and methodology

The chemicals utilized in this study are listed in **Table 9**. They were of reagent-grade quality, commercially available, and used as received. Distilled water was employed for preparing all solutions.

Table 9. Information on reagents used in this work.

Reagent Name	Molecular Formula	Provider	CAS number
o-anisidine	$CH_3OC_6H_4NH_2$	Sigma-Aldrich	90-04-0
hydrochloric acid	HCl	Neon	7647-01-0
ammonium persulfate	$(NH_4)_2S_2O_8$	Neon	7727-54-0
acetone	C_3H_6O	Sigma-Aldrich	67-64-1
terpineol	$C_{10}H_{18}O$	Sigma-Aldrich	8000-41-7
water	H_2O	Sigma-Aldrich	7732-18-5
ethanol	C_2H_6O	Neon	64-17-5
ethyl cellulose	$C_{20}H_{38}O_{11}$	Sigma-Aldrich	9004-57-3

5.2.1. Synthesis route of poly(o-methoxyaniline)

The process to produce POMA powders is illustrated in **Figure 29** and the chemicals utilized in this process are listed in **Table 9**. Briefly, 70 mL of o-anisidine solution was added to a 250 mL glass volumetric flask. With a heating mantle, the solution was distilled for 3 hours at 230 °C. At the end of the process, the clear distilled liquid was used to obtain POMA. A 1 M HCl solution was prepared, and 50 mL of this solution was added to a 250 mL volumetric flask. The solution was stabilized in an ice bath at 0-10 °C when 2.88 g of $(NH_4)_2S_2O_8$ was added to it (volumetric flask 1). Subsequently, in a 500 mL volumetric flask (volumetric flask 2), 75 mL of the 1 M HCl solution was added. This volumetric flask was also stabilized in an ice bath at 0-10 °C. Then, 6.2 mL of the distilled o-anisidine was added to volumetric flask 2. The solution from volumetric flask 1 was transferred to a separation funnel. This solution slowly dripped for 10 minutes into volumetric flask 2, still under an ice bath. This mixture was stirred using a magnetic stirrer at 300 rpm. Afterwards, the material was filtered, washed with acetone solution 3 times, and dried in a drying oven at 40 °C.
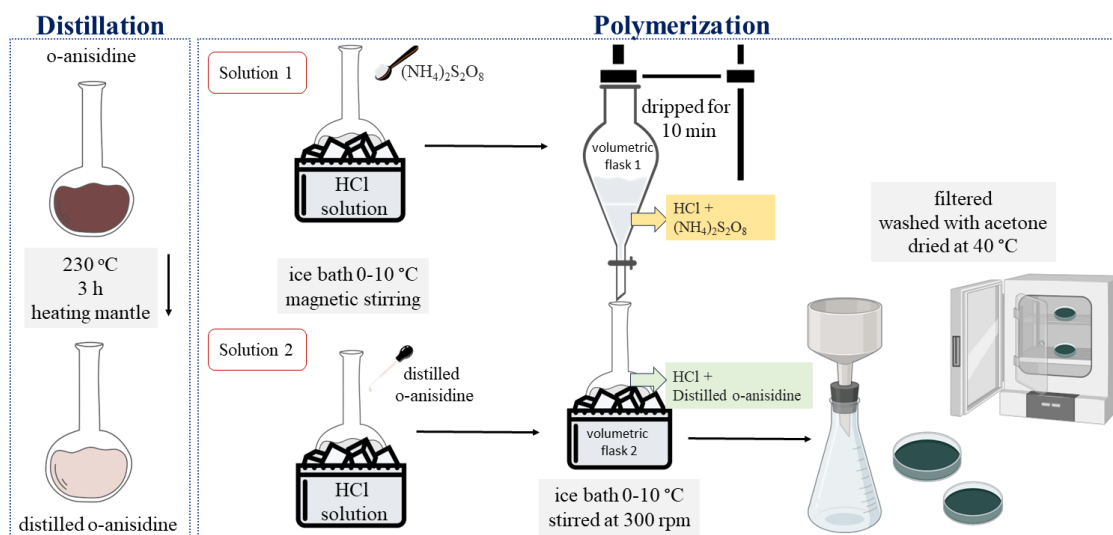
Figure 29: Sketch of the process used to synthesize POMA powders.

5.2.2. Characterization

XRD, XPS, SEM, and porosimetry techniques were performed on POMA in the same manner as for CBFG powders. The detailed methodology for these analyses is provided in Section 4, subsection 4.2.2. Henceforth, only procedures not previously stated will be presented.

5.2.3. Fourier-transform infrared spectroscopy infrared of POMA powders

FTIR spectra of POMA powders were recorded on a Bruker spectrophotometer in the range 400–4000 cm^{-1} but only the region related to the polymer chain is presented (1800–800 cm^{-1}). Samples were pressed into KBr disks. Results were analyzed using Bruker's Spectroscopic Software OPUS.

5.3. Results and Discussion

5.3.1. Characterization

5.3.1.1. X-ray diffraction of POMA powders

The XRD pattern for the POMA powder is shown in **Figure 30**. Previous results of emeraldine-salt form of POMA synthesized by different routes presented similar diffractograms [179].
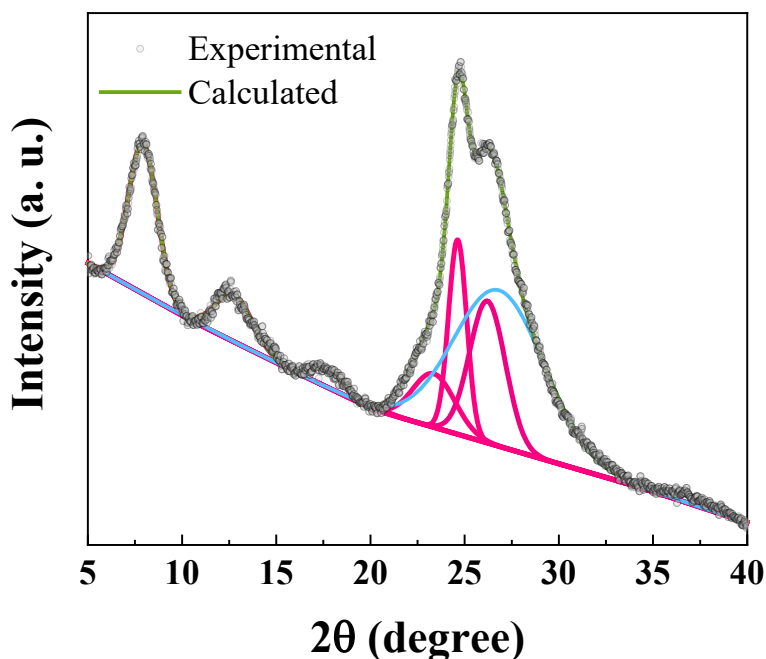
Figure 30: X-ray diffraction pattern of the as-prepared POMA. XRD pattern (gray circles) was fitted (green curves) by using the Gaussian function (pink curves). The blue curves are due to the non-crystalline and nanosized crystallites contribution.

The Bragg diffraction peaks of $2\theta \sim 7.9°$, $12.8°$, $17.7°$, $23.4°$, $24.6°$, $26.2°$, $26.8°$ and a broad peak $36.8°$ can be found in the XRD pattern of the POMA salts [180]. These peaks were assessed from the fit of the experimental XRD patterns using the Gaussian function. The polymer chain alignments are due the HCl doping integrated in the synthesis process and caused the semi crystalline XRD patterns whereas the broad peaks are a coexistence of nanosized crystallites and amorphous chains [112].

5.3.1.2. X-ray photoelectron spectroscopy of POMA powders

Figure 31a shows the XPS survey spectrum of the emeraldine-salt form of POMA [179]. Elemental analysis exhibited C 76.72 wt.%, N 7.12 wt.%, O 14.16 wt.%. Traces of Cl and S have been detected. They were used as HCl and $(NH_4)_2SO_8$ during POMA synthesis for N protonation and deprotonation. Calculated values were Cl 1.46 wt.% and S 0.24 wt.%,
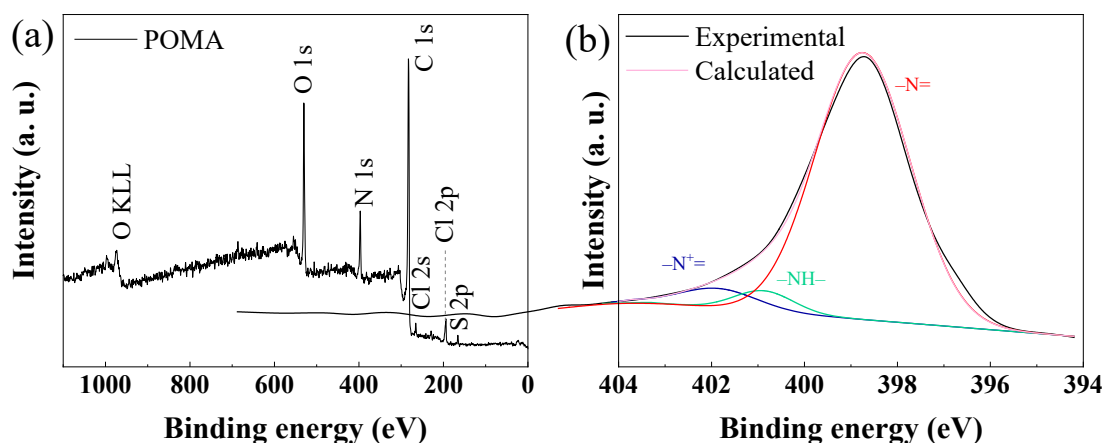
Figure 31: (a) Full survey and (b) N1s XPS scan spectra of the as-prepared POMA.

An N1s elemental scan (**Figure 31b**) has been interpreted to gain insight into the polymer chain. Peaks corresponding to imine N atoms (–N=, binding energy (B.E.) ~398.7 eV), amine N atoms (–NH–, B.E. ~400.9 eV) as well as charged N species (B.E. ~401.9 eV) were observed. This agrees with the FTIR spectrum of the as-prepared POMA powders presented in **Figure 32**.

5.3.1.3. Fourier-transform infrared spectroscopy infrared of POMA powders

The presence of the two bands at 1493 and 1573 cm^{-1} (**Figure 32**) have a major contribution from the quinoid rings and benzenoid ring units, respectively. This is an indicator that the polymer chain is composed of the amine and imine units [179].
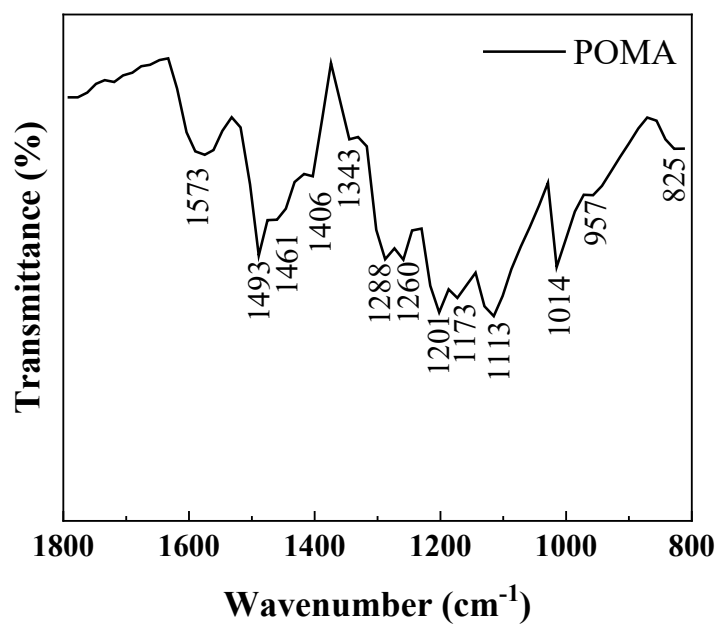
Figure 32: FTIR spectrum of the as-synthesized POMA.

5.3.1.4. Scanning electron microscopy of POMA powders

Figure 33 shows the SEM images of the as-prepared POMA. The features' morphology is globular with diverse micrometric sizes, which may consist of both crystalline and amorphous phases.
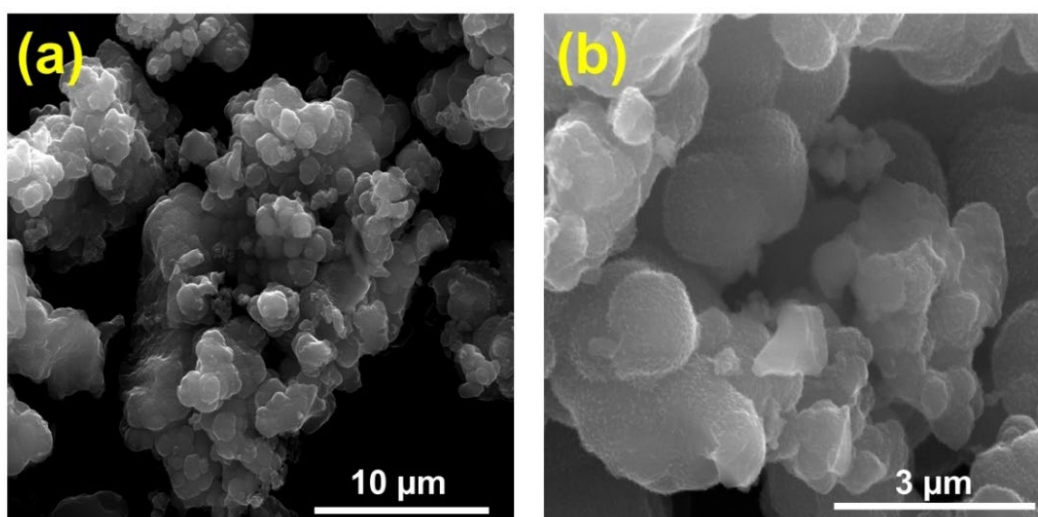
Figure 33: SEM images of the as-synthesized POMA with scale bar of (a) 10 μm and (b) 3 μm.

5.3.1.5. Porosimetry of POMA powders

The porosity and surface area of the POMA powders were evaluated using the BET analysis. Isotherm curves (**Figure 34**) indicate that the surface area of POMA was extremely low, at approximately 4 m^2 g^{-1}. Since a low surface area is known to negatively impact sensing and adsorption capabilities of adsorbents, no experiments were conducted to evaluate the adsorption capacity of POMA, suggesting that the result would be inferior to that of CBFG powders.
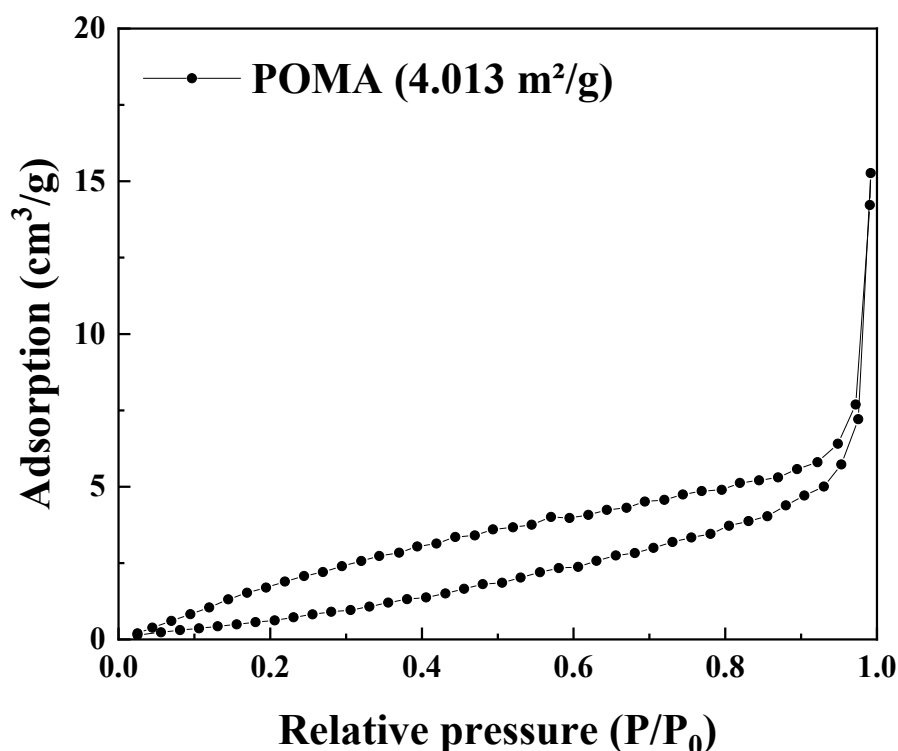
Figure 34: (a) BET isotherms for POMA powders. The dashed red lines correspond to the BET isotherms of POMA.

5.4. Conclusion

We successfully synthesized POMA in its emeraldine salt form through oxidative polymerization using HCl as a dopant, as evidenced by XRD and XPS results. Although traces of Cl and S were detected due to remaining reagents in the synthesis, the desired product was still achieved. FTIR data revealed a polymer chain composed of amine and imine units, consistent with XPS analysis. SEM images depicted material with a globular morphology and varying sizes. However, this morphology did not contribute significantly to an increase in surface area, which POMA exhibited at a very low level of around

$4 \, m^2 \, g^{-1}$. Despite its lower surface area compared to CBFG, the ease of synthesis, coupled with its remarkable properties such as functionalized surface, dispersibility, and doping, makes POMA an excellent material for formulating a conductive ink.

CHAPTER 6. Fabrication of a conductive ink composed of CBFG, POMA, or their combination.

This chapter approaches the fabrication of a conductive ink based on CBFG, POMA, or their combination. The objective is to optimize the ink's conductive properties and adsorption characteristics for coating the active area of the SAW device, thereby enhancing features such as sensitivity.

This chapter is part of a research article entitled "Flash Graphene and Poly(O-Methoxy Aniline) for the Composition of a Solvent-Based Conductive Ink" published in the Surfaces and Interfaces (Impact Factor (2023) – 6.2)[157]. As per Elsevier subscription guidelines, authors maintain the privilege of incorporating the article into a thesis, as long as it remains unpublished for commercial purposes.

6.1.   Materials and methodology

6.1.1. Production of conductive ink

The process of ink production is illustrated in **Figure 38** and the chemicals utilized in the production of the ink are listed in **Table 9**. An amount of as-prepared CBFG or POMA, or a combination of CBFG (X_1) and POMA (X_2), according to combinations of the experimental design (ranging from 0 to 40 mg L^{-1}), was added to the beaker 1 (step 1). Then, a volume of water, terpineol, and ethanol were added to the beaker 1 in proportion to the amount of solid precursor to achieve the target concentration (step 2). This mixture was kept under magnetic stirring for 30 minutes at RT. In the beaker 2, an amount of ethyl cellulose (10 cp and 46 cp – 1:1) was magnetically mixed also considering the binder amount (X_3) (ranging from 4 to 16 mg L^{-1}), with a proper volume of ethanol until homogenized (step 3). The solution from beaker 2 was poured into the previous solution (beaker 1) and subjected to magnetic stirring and sonication for 30 minutes each (step 4). Afterwards, according to step 5 the solvent content was evaporated using a rotary evaporator set to 60 mbar and 50 °C, aiming to reach the final ink concentration. The resulting slurry underwent ball milling util it achieved the appropriate viscosity for deposition. Subsequently, it was applied onto a glass substrate using the doctor blade technique, ensuring a consistent thickness of 200 μm. After applying the ink, the samples were dried in a controlled atmosphere at 55 °C for 2 hours. Subsequently, the EC was measured using a semiconductor analyzer.
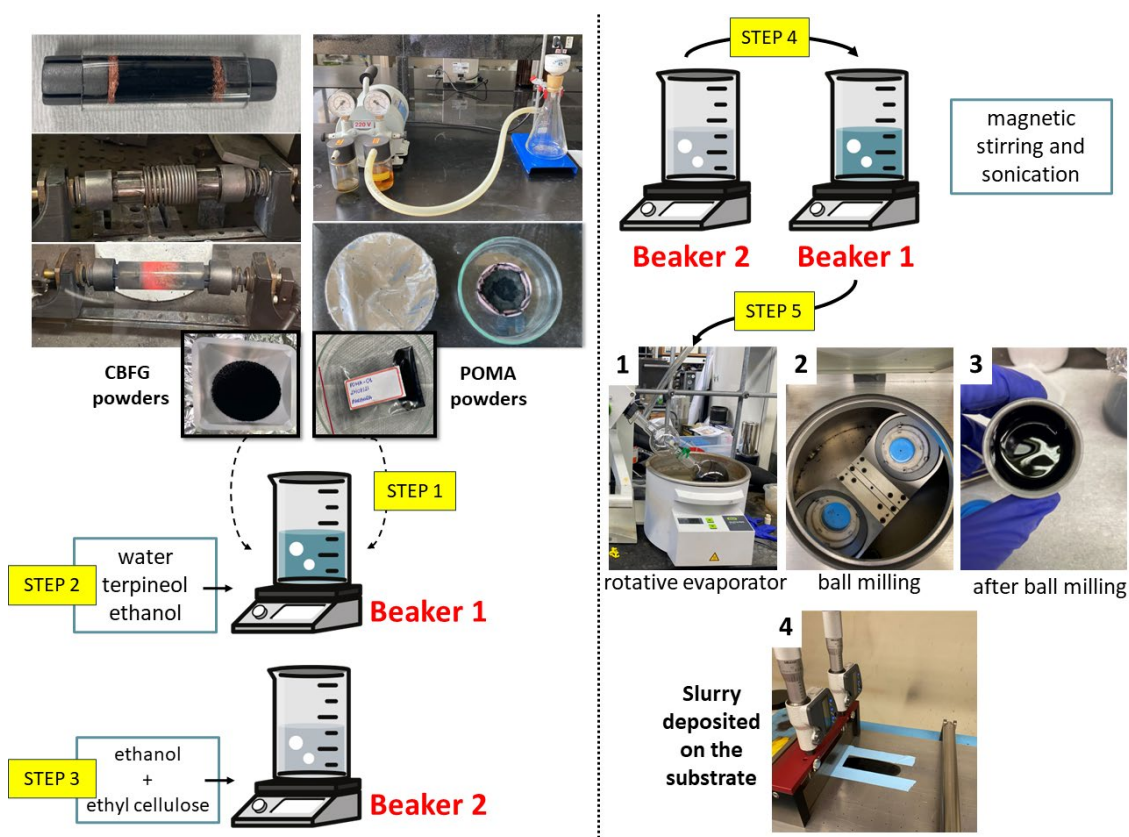
Figure 35: Diagram of the ink production process.

6.1.2. Electrical conductivity measurements and ink optimization

Eleven runs, each consisting of three samples, were measured to calculate the average conductivity, resulting in a total of 33 probes. The ink, in a viscous slurry form, was applied to produce solid films with thickness of 200 μm on glass substrates (XY dimensions: 15 mm × 25 mm) using the doctor blade technique. The EC of the ink was then measured using a semiconductor analyzer. The effect of all process parameters was analyzed based on the EC response (S m^{-1}). A 2^3 factorial design of experiment was performed using eight cube (factorial) points, and three replicates of center point, resulting in 11 experiments. This design has been selected to determine the optimal number of experiments based on EC. Herein, the independent variables were the concentration of CBFG (X_1: 0–40 mg L^{-1}), concentration of POMA (X_2: 0−40 mg L^{-1}), and concentration of binder (X_3: 4–16 mg L^{-1}), **Table 10**. The binder concentration range was chosen according to previous studies. The results were evaluated in STATISTICA 12.0 software.

Table 10. Matrix of the experiment's factors, their levels and response

Code	Factor	Level		
		Low (-1)	Central (0)	High (+1)
X_1	CBFG concentration (mg L^{-1})	0	20	40
X_2	POMA concentration (mg L^{-1})	0	20	40
X_3	Binder concentration (mg L^{-1})	4	10	16

6.2.   Results and discussion

6.2.1. Electrical conductivity measurements and ink optimization

The highest EC values obtained for CBFG and POMA inks when deposited on glass substrate via doctor blade technique were 0.77 S m^{-1} and 9.6×10^{-5} S m^{-1}, respectively. It is important to mention that every deposited film had a minimum mixed concentration of binder, which is highly resistive, negatively affecting the EC of the films (**Table 11**). CBFG-based ink was expected to be conductive as the CBFG precursor (carbon black) exhibited 2.3 Ω before flashing. The EC value of POMA-based ink was within the values found in literature (~9×10^{-5} – ~9×10^{-5} S cm^{-1}) [112,179–181]. This shows the success of the synthesis route to obtain a conductivity polymer.

Table 11. Coded matrix for experimental design and EC for each material

Runs	X_1	X_2	X_3	Electrical conductivity
	(mg mL^{-1})			(S m^{-1})
1	0	0	4	7.90E-09
2	0	0	16	1.14E-08
3	0	40	4	9.63E-05
4	0	40	16	1.23E-04
5	40	0	4	7.66E-01
6	40	0	16	3.69E-04
7	40	40	4	6.32E-01
8	40	40	16	3.99E-01
9	20	20	10	2.97E-01
10	20	20	10	5.94E-01
11	20	20	10	2.25E-01

Considering the values obtained in **Table 11** and in order to optimize the ink performance and obtain the optimal condition with the highest value of EC, an analysis of variance (ANOVA) was performed and is presented in **Table 12**.

Table 12. Analysis of variance for the experimental central composite design (CCD).

Parameter	SS	DF	MS	F	p
(1) CBFG concentration (mg·L^{-1})	0.40	1.0	0.40	316.18	0.00*
(2) POMA concentration (mg·L^{-1})	0.01	1.0	0.01	6.88	0.12
(3) Binder concentration (mg·L^{-1})	0.12	1.0	0.12	97.51	0.01*
1 by 2	0.01	1.0	0.01	6.86	0.12
1 by 3	0.12	1.0	0.12	97.52	0.01*
2 by 3	0.04	1.0	0.04	27.80	0.03*
1*2*3	0.04	1.0	0.04	27.79	0.03*
Lack of Fit	0.00	1.0	0.00	2.02	0.29
Pure Error	0.00	2.0	0.00		
Total SS	0.75	10.0		R² 0.9931	

*Significative factor (p<0.05).

It is possible to observe that there was no lack of adjustment for the evaluated response, and the proposed regression model (**Equation (6)**) explains about 99.3% of the variation in the responses (R² 0.9931 / R²adj 0.9771).

$$y = 0.23 + 0.44\,X_1 + 0.06\,X_2 - 0.24\,X_3 + 0.06\,X_1\,X_2 - 0.24\,X_1\,X_3 + 0.13\,X_2\,X_3 + 0.13\,X_1\,X_2\,X_3 \quad (6)$$

From the Pareto chart analysis (**Figure 36a**), it was possible to observe that the linear parameters for the CBFG concentration and the Binder concentration showed a significant effect, being positive and negative, respectively. This result indicates that inks obtained with a higher CBFG concentration and a lower Binder concentration present better EC result. This result is confirmed when evaluating that the interaction between these factors was also significant and with a negative result.
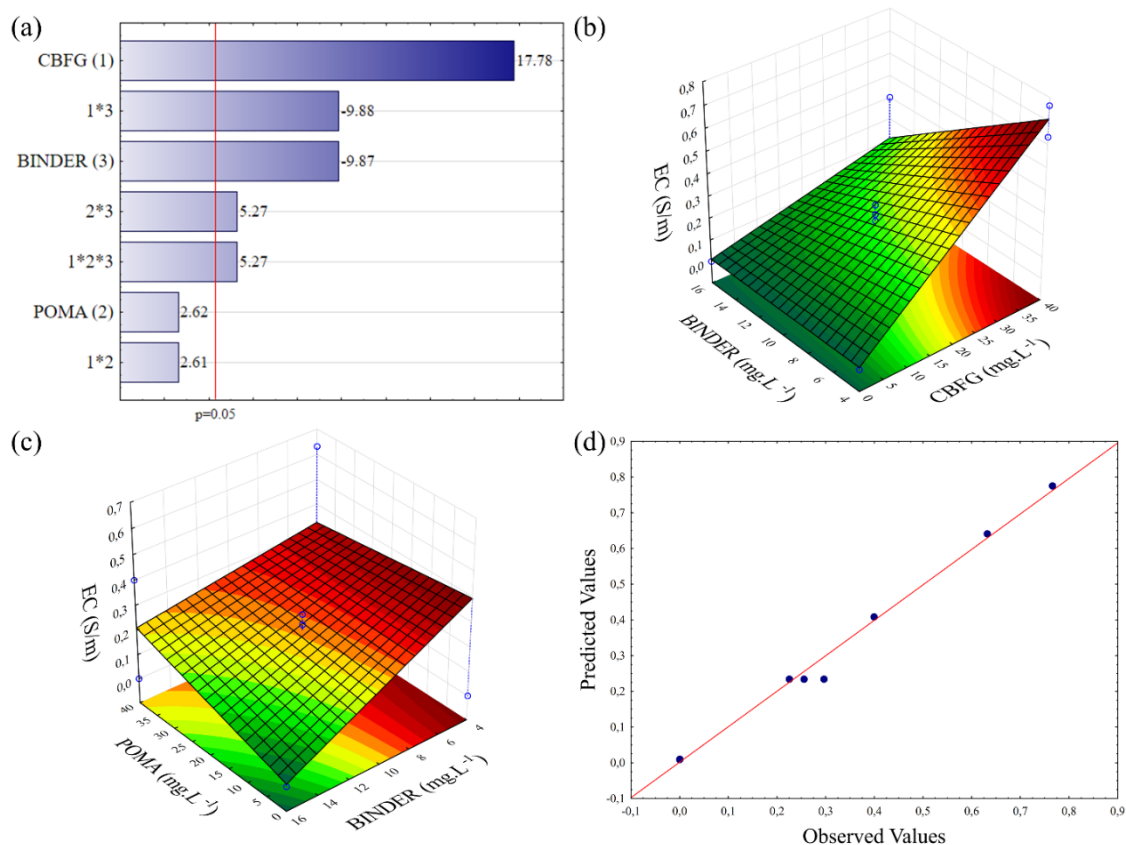
Figure 36. (a) Pareto chart, (b) response surface for the interaction between BINDER vs. CBFG, and (c) POMA vs. BINDER. (d) Predicted vs. observed values.

The response is improved when one of the factors is positive and the other negative, confirmed on the response surface (**Figure 36b**). Still, by Pareto, it is observed that the interaction between POMA and Binder concentration was also significant, this time being positive. That is, when both are positive or both negative, the EC response is improved. In this case, looking at the response surface (**Figure 36c**), the response presented a better value when both were negative since the Binder concentration factor was significant and negative. The low interaction between CBFG and POMA in the improvement of the ink EC when both are used in the composition might be due to the inertness of pure CBFG, showing that the procedure to fabricate the ink can be further optimized.

The Observed vs. Predicted (**Figure 36d**) shows good linearity, indicating that the model corresponds well to the evaluated response. The desirability function was used in the optimization process to find a formulation that benefited the response simultaneously. From the desirability profile of the process, it is possible to observe that the responses

had a variability between $7.9 \cdot 10^{-9}$ and 0.765 S m^{-1} for electric conductivity. Applying the simultaneous optimization process, the desirability function finds an answer for the best ink formulation with a value of 0.768 S m^{-1} when the CBFG, POMA, and Binder concentrations are 40.0, 2.0, and 4.0 mg L^{-1}, respectively.

Optimizing concentration parameters for achieving controlled and wanted printed features with the desired EC is crucial for ensuring reliable printing of CBFG/POMA ink in various applications such as printed electronics, sensors, and conductive traces in electronic devices. This optimized ink, composed of CBFG and POMA in specific amounts, can be printed on diverse substrates (both flexible and rigid) using conventional methods like inkjet printing and screen printing. However, a comprehensive study of the ink's variable properties such as viscosity, surface tension, curing methods, among others, must be conducted to understand the process and ensure its reliability.

6.3. Conclusion

The turbostratic CBFG powders were dispersed in an ethanol solution, and with and without POMA, formed a stable, and concentrated slurry. The POMA powder, when applied in the ink, exhibited a slight contribution for the increment of the ink's EC. Both materials were used individually and combined to compose a conductive ink. It was observed that the highest EC of 0.768 S m^{-1} for the concentrations of 40.0, 2.0, and 4.0 mg L^{-1} of CBFG, POMA, and binder, respectively.

CHAPTER 7. SAW devices

This chapter approaches the microfabrication of the bare SAW devices. The fundamentals of the primary techniques employed in the methodology, along with the corresponding results, are addressed.

7.1. Microfabrication of SAW devices

7.1.1 Electron beam lithography

Electron beam lithography (EBL) is a type of maskless lithography that is widely used in the fabrication of microelectronic devices and other nanotechnology applications, including semiconductor fabrication and microelectromechanical systems (MEMS) [182,183].

EBL is a process that uses a focused beam of electrons to create patterns on a substrate with high accuracy and resolution. The electron beam is directed onto an electron-sensitive resist, and then the beam is scanned across the resist's surface in a dot-by-dot fashion to generate patterns on the substrate with precision. The size and shape of the pattern are determined by the beam's size and shape, which can be varied by controlling the voltage and current of the electron beam. After exposure, the resist is developed to remove either the exposed or unexposed portions of the resist, depending on the resist type [182].

7.2. Materials and methodology

7.2.1. Microfabrication routine and parameters optimization

EBL system (Elionix ELS-G100) was used to produce and optimize the microfabrication of the pads and IDTs. The optimization was carried out to obtain resonators with patterns of 1000 nm, 500 nm, and 100 nm. For that the following parameters were considered: field size, feed pitch, scan pitch, area dose, and dose time, while maintaining a field size of 1,000 μm and a beam current of 1E-9 A. The samples were rinsed separately with acetone and IPA, and then dried using N_2 gas. A spin coating method was used to deposit the 950 PMMA A4. The coating process involved spinning the sample at a speed of 500 rpm to spread the PMMA and then at 3,000 rpm to ensure uniform deposition. The sample was pre-baked at 180 ºC for 1 min and 40 s. After exposure, methyl isobutyl ketone (MIBK):IPA developer was used to develop the sample for 1 min and 30 s, followed by rinsing with IPA and drying with N_2 gas.

To create an adhesion layer, an EBE was used to deposit 10 nm of Ti, followed by the deposition of 50 nm of Au as a metallic contact. A lift-off procedure was performed by immersing the samples in acetone overnight. The samples were then rinsed with acetone and any remaining reactions were halted using IPA. Finally, N_2 gas was employed to dry the samples. Optical inspections were conducted after each step to ensure quality control.

Typically, for non-conductive substrates, the E-beam deflects, and consequently, it cannot penetrate the sample, making it impossible to write the pattern on non-conductive polymers. This is also the case for glass substrates, where a layer of chromium (~3 nm) is needed to make the surface conductive, and the EBL process can be successfully performed. Because of that, the devices were not fabricated on the glass samples. This will be classified as future work.

7.2.2. Production of the printed circuit board

A printed circuit board (PCB) was fabricated to perform measurements of the devices on the network analyzer, as depicted in **Figure 37**. The substrate employed was FR4, which belongs to a class of PCB base materials composed of a flame-retardant epoxy resin and a composite of glass fabric. Semi-precision coaxial RF connectors known as SubMiniature version A (SMA) were utilized. The transmission medium consisted of a conventional coplanar waveguide (CCW). To secure the device, simple tape was used to affix it to the etched portion of the PCB. Wire bonds were employed to establish connections both as a ground and along the transmission path.
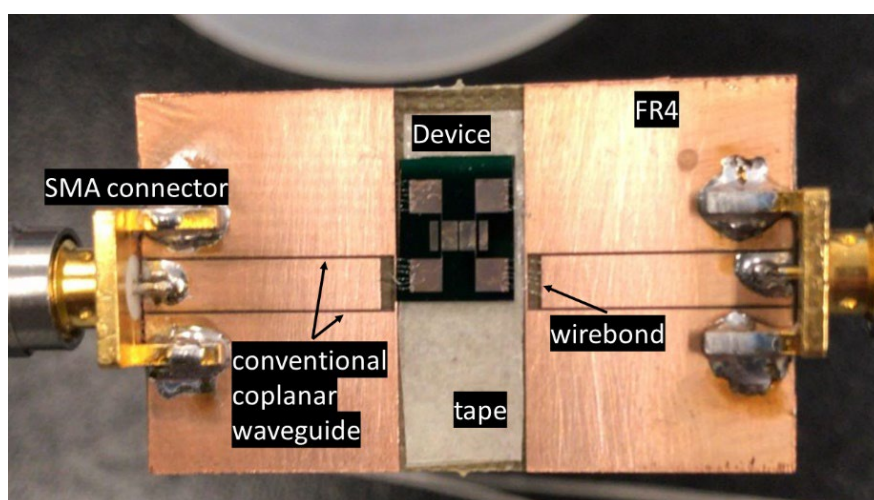
Figure 37: PCB for VNA measurements.

7.3. Results and discussion

7.3.1 Optimization of microfabrication parameters

Figure 38 shows the SAW device produced using the optimized conditions of the microfabrication process of the 1000 nm pattern were found to be 1,000,000 dots of field size, 3 dots of feed pitch, 3 dots of scan pitch, 1280 µC/cm^2 of area dose and 0.1152 µsec/dot of dose time. The small particles are from the PMMA.
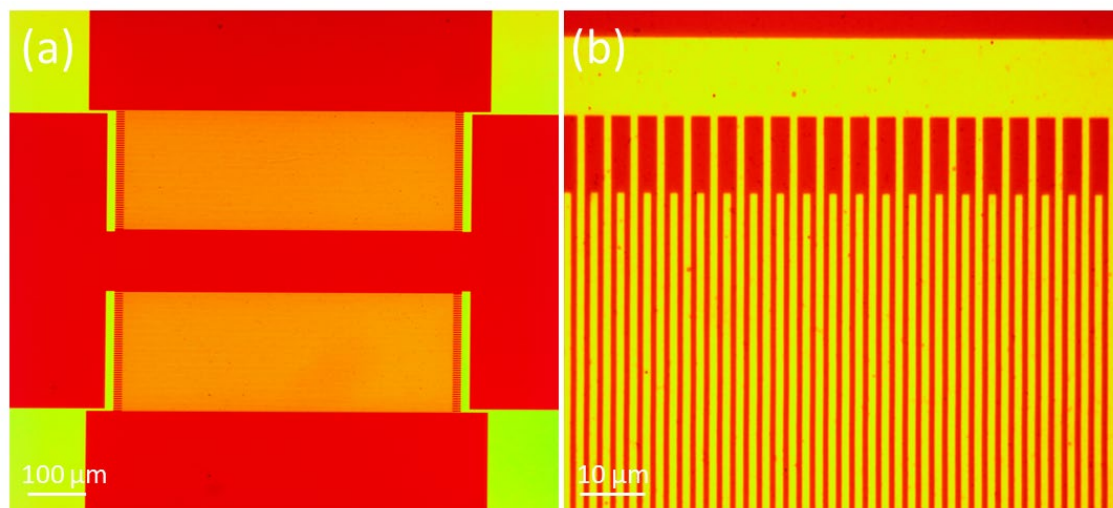
Figure 38: SAW sensor pattern on GaN/Si after lift-off procedure (1 min and 20 s). Smallest feature of 1000 nm.

7.4. Conclusion

SAW devices were successfully produced, presenting clear fingers and large IDTs. These devices are now in tryout phase and simulations are being done to understand fundamentally the occurrences in the device. It is expected that further studies will simulate the fundamental condition of the SAW device comprised of GaN thin film as piezoelectric substrate on Si and glass, as well as test the devices in a semiconductor analyzer with and without the ink.

CHAPTER 8.Conclusion and Perspectives

Conclusion

This work was developed with the main objective of demonstrating the feasibility of developing a heterostructure comprising GaN and CBFG/POMA for SAW device applications. To achieve this, GaN thin films were successfully deposited using magnetron sputtering. These films were found to be polycrystalline with a wurtzite crystal structure and exhibited preferential orientation along the *c*-direction, as confirmed by XRD, Raman, and TEM analyses. It was noted that GaN films grown for 6 hours on both Si and glass substrates showed a high RMS value (~19 nm), which could potentially have a negative impact on SAW performance. However, these films also displayed better crystalline quality (FWHM ~ 0.265 ± 0.001 (GaN/Si) and FWHM ~ 0.311 ± 0.005 (GaN/glass)) compared to those grown for 2 (FWHM ~ 0.279 ± 0.004 (GaN/Si) and FWHM ~ 0.540 ± 0.030 (GaN/glass)) and 4 hours (FWHM ~ 0.285 ± 0.002 (GaN/Si) and FWHM ~ 0.316 ± 0.007 (GaN/glass)), which could be a more crucial factor in SAW functionality. The electrical tests indicated satisfactory ohmic contact between the IDTs and the GaN film, a desirable characteristic for promoting strain rather than current in response to radiofrequency stimuli.

CBFG was synthesized successfully through an ultrafast and solvent-free FJH method, demonstrating its high purity as confirmed by XPS analysis of the powders. SEM and TEM images further validated that the CBFG comprised turbostratic sheets of GR. This characteristic enhances CBFG's dispersibility in ethanol solutions, facilitating the formation of stable and concentrated slurries. The prepared CBFG exhibited a high surface area (~293 m^2 g^{-1}) and demonstrated excellent adsorption properties (R% = 100% after 20 min), making it an ideal candidate for composing a conductive ink.

POMA was effectively synthesized in its emeraldine salt form via oxidative polymerization using HCl as a dopant, as confirmed by XRD and XPS analyses. FTIR data revealed a polymer chain consisting of amine and imine units, consistent with XPS findings. SEM images showed a globular morphology with varying sizes. However, this morphology did not significantly contribute to an increase in surface area, which remained low at around 4 m^2 g^{-1} for POMA. Despite its lower surface area compared to CBFG, the straightforward synthesis process and properties as processability, dispersibility, and chemical surface of POMA, make it an excellent candidate in combination with CBFG for composing a conductive ink.

After obtaining both materials (CBFG and POMA), they were utilized to produce a conductive ink. Both materials were used independently and in combination to formulate the conductive ink. The composition of this ink was optimized by adjusting the concentration ratio of the precursors and binder. Turbostratic CBFG powders were dispersed in an ethanol solution to form a stable and concentrated slurry, with and without the addition of POMA. When POMA was included in the ink, it contributed slightly to enhancing the ink's EC. The highest EC value of 0.768 S m^{-1} was observed for a concentration combination of 40.0 mg L^{-1} CBFG, 2.0 mg L^{-1} POMA, and 4.0 mg L^{-1} binder.

SAW devices were successfully manufactured. Currently, they have been fabricated solely on Si(100) due to equipment limitations encountered with dielectric materials like glass during EBL. Although the fabrication process is complete, additional studies are required to assess the device's functionality both with and without the ink.

This thorough investigation is significant as it provides the possibility of obtaining top-notch sputtered samples and organic conductive ink with suitable characteristics for SAW device applications. It sets the stage for the development of SAW devices capable of operating at high frequencies.

Perspectives

This thesis is part of a project focused on producing SAW sensors with GaN-based piezoelectric substrates and CBFG/POMA ink as the sensing layer. It aims to ensure device functionality by achieving resonance frequency using a VNA. This thesis, a sub-project of the main project, aimed to obtain high-quality GaN thin films via sputtering and synthesizing CBFG and POMA nanomaterials using FJH system and oxidative polymerization, respectively. The objective was to develop a heterojunction with GaN as the piezoelectric substrate and CBFG/POMA ink deposited on the GaN surface and between lithographically obtained electrodes. Completing the main project requires achieving other sub-project objectives, namely:

- Simulate the SAW propagation on various substrates to obtain theoretical values for the electromechanical coefficient and resonant frequency.

- Conduct trials on the already fabricated devices to assess their performance.

- Produce new devices incorporating GaN thin films as piezoelectric substrates on glass.

- Test the newly produced devices using a semiconductor analyzer, both with and without the conductive ink, to evaluate their functionality.

References

1   ABDEL-KARIM, R.; REDA, Y.; ABDEL-FATTAH, A. Review—Nanostructured Materials-based Nanosensors. **J Electrochem Soc**, v. 167, p. 037554, 2020.

2   KALSOOM, T. *et al.* Advances in Sensor Technologies in the Era of Smart Factory and Industry 4.0. **Sensors (Switzerland)**, v. 20, p. 1–22, 2020.

3   JAVAID, M. *et al.* Exploring the Potential of Nanosensors: a Brief Overview. **Sensors International**, v. 2, p. 100130, 2021.

4   LI, C. *et al.* Miniature Single-fiber Photoacoustic Sensor for Methane Gas Leakage Detection. **Opt Lasers Eng**, v. 149, p**.** 106792, 2022.

5   ARNDT, N. *et al.* Different Approaches to Develop Nanosensors for Diagnosis of Diseases. **Advanced Science**, v. 7, p. 1–31, 2020.

6   JAVAID, M. *et al.* Sensors for Daily Life: a Review. **Sensors International**, v. 2, p. 100121, 2021.

7   TAN, E. *et al.* Towards Closed-loop Integration of Point-of-care Technologies. **Trends Biotechnol**, v. 37, p. 775–788, 2019.

8   ADAM, T.; GOPINATH S. Nanosensors: Recent Perspectives on Attainments and Future Promise of Downstream Applications. **Process Biochemistry**, v. 117, p. 153–173, 2022.

9   LÄNGE, K.; RAPP, B. E.; RAPP, M. Surface Acoustic Wave Biosensors: a Review. **Anal Bioanal Chem**, v. 391, p. 1509–1519, 2008.

10   OKUDA, S. *et al.* Graphene Surface Acoustic Wave Sensor for Simultaneous Detection of Charge and Mass. **ACS Sens**, v. 3, p**.** 200–204, 2018.

11   LIU, H. *et al.* Resonance Frequency Readout Circuit for a 900 MHz SAW Device. **Sensors (Switzerland)**, v. 17, p. 1–20, 2017.

12   MÜLLER, A. *et al.* GaN/Si based Single SAW Resonator Temperature Sensor Operating in the GHz Frequency Range. **Sens Actuators A Phys**, v. 209, p. 115–123, 2014.

13   JIANG, Y. *et al.* SAW Sensor for Influenza A Virus Detection Enabled with Efficient Surface Functionalization. **Sens Actuators B Chem**, v. 209, p. 78–84, 2015.

14   JALANDRA, R. *et al.* Strategies and Perspectives to Develop SARS-CoV-2 Detection Methods and Diagnostics. **Biomedicine and Pharmacotherapy**, v. 129, p. 110446, 2020.

15   HASSAN, M. M. *et al.* A Review on Plasmonic and Metamaterial based Biosensing Platforms for Virus Detection. **Sens Biosensing Res**, v. 33, p. 100429, 2021.

16   GOGOLA, J. L. *et al.* Label-free Aptasensor for P24-HIV Protein Detection based on Graphene Quantum Dots as an Electrochemical Signal Amplifier. **Anal Chim Acta**, v. 1166, p. 338548, 2021.

17   CRUZ, C. *et al.* Carbon SH-SAW-based Electronic Nose to Discriminate and Classify Sub-ppm NO_2. **Sensors**, v. 22, p. 1–13, 2022.

18   LE, X. *et al.* Surface Acoustic Wave Humidity Sensors based on Uniform and Thickness Controllable Graphene Oxide Thin Films Formed by Surface Tension. **Microsyst Nanoeng**, v. 5, 2019.

19   ZHANG, J. *et al.* Recent Advances in Acoustic Wave Biosensors for the Detection of Disease-related Biomarkers: a Review. **Anal Chim Acta**, v. 1164, p. 338321, 2021.

20   GRAY, E. R. *et al.* Ultra-rapid, Sensitive and Specific Digital Diagnosis of HIV with a Dual-channel SAW Biosensor in a Pilot Clinical Study. **NPJ Digit Med**, v. 1, p. 35, 2018.

21   XU, S. *et al.* Carbon Dioxide Sensors Based on a Surface Acoustic Wave Device with a Graphene-nickel-L-alanine Multilayer Film. **J Mater Chem C Mater**, v. 3, p. 3882–3890, 2015.

22   XU, S. *et al.* Surface Acoustic Wave DMMP Gas Sensor with a Porous Graphene/PVDF Molecularly Imprinted Sensing Membrane. **Micromachines (Basel)**, v. 12, p. 552, 2021.

23   MANDAL, D.; BANERJEE, S. Surface Acoustic Wave (SAW) Sensors: Physics, Materials, and Applications. **Sensors**, v. 22, p. 820, 2022.

24   BALLANTINE, Jr. D. S. *et al.* Acoustic Wave Sensors: theory, design and physico-chemical applications. **Elsevier**, 1996.

25   ZAMKOVSKAYA, A.; MAKSIMOVA, E. Aspects of symmetry of Electromechanical Coupling Factors in Piezoelectric Single Crystals. **J Phys Conf Ser**, v. 769, p. 012067, 2016.

26   AGOSTINI, M.; CECCHINI, M. Ultra-high-frequency (UHF) Surface-acoustic-wave (SAW) Microfluidics and Biosensors. **Nanotechnology**, v. 32, p. 312001, 2021.

27   KAO, H. L. *et al.* Epitaxial AlN Thin Film Surface Acoustic Wave Devices Prepared on GaN/Sapphire using Low-temperature Helicon Sputtering System. **Jpn J Appl Phys**, v. 47, p. 124–129, 2008.

28   PALACIOS, T. *et al.* High Frequency SAW Devices on AlGaN: Fabrication, Characterization and Integration with Optoelectronics. **In: Proceedings of the IEEE Ultrasonics Symposium**, p. 57–60, 2002.

29   WOODS, R. C.; BOROUMAND, F. A. Comments on 'Epitaxially Grown GaN Thin-film SAW Filter with High Velocity and Low Insertion Loss'. **IEEE Trans Electron Devices**, v. 53, p. 173–176, 2006.

30   PANKOVE, J. I.; MOUSTAKAS, T. D. Gallium Nitride (GaN) II - Semiconductors and semimetals. **Academic Press**, 1999.

31   YADAV, B. S.; MAJOR, S. S.; SRINIVASA, R. S. Growth and Structure of Sputtered Gallium Nitride Films. **J Appl Phys**, v. 102, p. 073516, 2007.

32   QUAY, R. Gallium Nitride Electronics. **Springer Berlin Heidelberg: Berlin, Heidelberg**, 2008.

33   MULLER, A. *et al.* GaN Membrane Supported SAW Pressure Sensors with Embedded Temperature Sensing Capability. **IEEE Sens J**, v. 17, p. 7383–7393, 2017.

34   PEREIRA, M. B.; DINIZ, E. M.; GUERINI, S. Structural and Electronic Properties of GaN (0001)/α-Al$_2$O$_3$ (0001) Interface. **Advances in Condensed Matter Physics**, v. 2015, 2015.

35   MULLER, A. *et al.* SAW Devices Manufactured on GaN/Si for Frequencies Beyond 5 GHz. **Electron Device Letters, IEEE**, v. 31, p. 1398–1400, 2010.

36   MÜLLER, A. *et al.* Sezawa Propagation Mode in GaN on Si Surface Acoustic Wave Type Temperature Sensor Structures Operating at GHz Frequencies. **IEEE Electron Device Letters**, v. 36, p. 1299–1302, 2015.

37   ZHOU, J. *et al.* Graphene-Based Fully Transparent Thin Film Surface Acoustic Wave Devices for Sensing and Lab-on-chip Applications. **J Electrochem Soc**, v. 166, p. B432–B440, 2019.

38   LEBEDEV, A. A. *et al.* Graphene on SiC Substrate as Biosensor: Theoretical Background, Preparation, and Characterization. **Materials**, v. 14, p. 590, 2021.

39   SANGAMITHIRAI, D. *et al.* A Voltammetric Biosensor based on Poly(o-methoxyaniline)-gold Nanocomposite Modified Electrode for the Simultaneous Determination of Dopamine and Folic Acid. **Materials Science and Engineering C**, v. 91, p. 512–523, 2018.

40   GAO, R. *et al.* Synthesis of ZnO@poly-o-methoxyaniline Nanosheet Composite for Enhanced NH$_3$-sensing Performance at Room Temperature. **Microchimica Acta**, v. 187, 2020.

41   SUI, J.; ZHANG, L.; PENG, H. Label-free DNA Sensor Construction using Self-assembled Poly(o-methoxyaniline) Hollow Nanospheres. **Eur Polym J**, v. 49, p. 139–146, 2013.

42   DINIZ, M. O. *et al.* Electrical Impedance of V_2O_5/POMA Hybrid Film Deposited by Casting for Application in Ammonia Gas Sensor. **J Electron Mater**, v. 50, p. 450–455, 2021.

43   ÖZMEN, E. N. *et al.* Graphene and Carbon Nanotubes Interfaced Electrochemical Nanobiosensors for the Detection of SARS-CoV-2 (COVID-19) and other Respiratory Viral Infections: a Review. **Materials Science and Engineering C**, v. 129, 2021.

44   SANJAY, S.; PRABAKARAN, K.; BASKAR, K. Epitaxy of Gallium Nitride Pyramids on Few Layer Graphene for Metal-semiconductor-metal based Photodetectors. **Mater Chem Phys**, v. 240, p. 122189, 2020.

45   IZYUMSKAYA, N. *et al.* Emergence of High Quality Sputtered III-Nitride Semiconductors and Devices. **Semicond Sci Technol**, v. 34, 2019.

46   ZHANG, B.; LIU, Y. A Review of GaN-based Optoelectronic Devices on Silicon Substrate. **Chinese Science Bulletin**, v. 59, p. 1251–1275, 2014.

47   ABDALLAH, B.; JAZMATI, A. K.; REFAAI, R. Oxygen Effect on Structural and Optical Properties of ZnO Thin Films Deposited by RF Magnetron Sputtering. **Materials Research**, v. 20, p. 607–612, 2017.

48   JAZMATI, A. K.; ABDALLAH, B. Optical and Structural Study of ZnO Thin Films Deposited by RF Magnetron Sputtering at Different Thicknesses: a Comparison with Single Crystal. **Materials Research**, v. 21, p. 1–6, 2018.

49   DOW, A. B. A. *et al.* Ultra nanocrystalline Diamond-based High-velocity Beam Lithography. **IEEE Trans Nanotechnol**, v. 11, p. 979–984, 2012.

50   BÉNÉDIC, F. *et al.* Surface Acoustic Wave Devices Based on Nanocrystalline Diamond and Aluminium Nitride. **Diam Relat Mater**, v. 13, p. 347–353, 2004.

51   BHUYAN, S.A. et al. Synthesis of Graphene. **Int Nano Lett**, v. 6, p. 65–83, 2016.

52   ZHANG, Y. *et al.* Surface Acoustic Wave-based Ultraviolet Photodetectors: a Review. **Sci Bull (Beijing)**, v. 65, p. 587–600, 2020.

53   MISCHKE, J. *et al.* Direct Growth of Graphene on GaN via Plasma-Enhanced Chemical Vapor Deposition under N_2 Atmosphere. **2D Mater**, v. 7, 2020.

54   BEKDÜZ, B. *et al.* Graphene Growth through a Recrystallization Process in Plasma Enhanced Chemical Vapor Deposition. **Nanotechnology**, v. 29, 2018.

55   ZHANG, X. *et al.* High-quality Graphene Transfer: via Directional Etching of Metal Substrates. **Nanoscale**, v. 11, p. 16001–16006, 2019.

56   ZHANG, G. *et al.* Versatile Polymer-free Graphene Transfer Method and Applications. **ACS Appl Mater Interfaces**, v. 8, p. 8008–8016, 2016.

57   REN, J. *et al.* Solution-Processable Core/Shell Structured Nanocellulose/Poly(o-methoxyaniline) Nanocomposites for Electrochromic Applications. **Cellulose**, v. 27, p. 9467–9478, 2020.

58   DAMASCENO, B. S. *et al.* Recent Improvements on Surface Acoustic Wave Sensors Based on Graphenic Nanomaterials. **Mater Sci Semicond Process**, v. 167, p. 107811, 2023.

59   RAYLEIGH, L. On Waves Propagated along the Plane Surface of an Elastic Solid. **Proceedings of the London Mathematical Society**, v. s1-17, p. 4–11, 1885.

60   DURANI, F. *et al.* Use of Surface Acoustic Wave (SAW) for Thermal Conductivity Sensing of Gases–a Review. **IETE Technical Review**, v. 38, p. 611–621, 2021.

61   DEVKOTA, J.; OHODNICKI, P. R.; GREVE, D. W. SAW Sensors for Chemical Vapors and Gases. **Sensors (Switzerland)**, v. 17, p. 13–15, 2017.

62   GAO, Y.; LI, Y.; DING, X. Acoustofluidic Technology for Cell Biophysics. **In: Micro and Nano Systems for Biophysical Studies of Cells and Small Organisms.** Elsevier, p. 153–171, 2021.

63   HU, B. *et al.* Fabrications of L-band LiNbO$_3$-based SAW Resonators for Aerospace Applications. **Micromachines (Basel)**, v. 10, p. 349, 2019.

64   AHMED, I. *et al.* Super-high-frequency Low-loss Sezawa Mode SAW Devices in a GaN/SiC Platform. **IEEE Trans Ultrason Ferroelectr Freq Control**, p. 1–1, 2023.

65   MUJAHID, A.; DICKERT, F. Surface Acoustic Wave (SAW) for Chemical Sensing Applications of Recognition Layers. **Sensors**, v. 17, p. 2716, 2017.

66   GO, D. B. *et al.* Surface Acoustic Wave Devices for Chemical Sensing and Microfluidics: a Review and Perspective. **Analytical Methods**, v. 9, p. 4112–4134, 2017.

67   WHITE, R. M.; VOLTMER, F. W. Direct Piezoelectric Coupling to Surface Elastic Waves. **Appl Phys Lett**, v. **7**, p. 314–316, 1965.

68   LI, X. *et al.* A High-Sensitivity MoS$_2$/Graphene Oxide Nanocomposite Humidity Sensor based on Surface Acoustic Wave. **Sens Actuators A Phys**, v. 341, p. 113573, 2022.

69   ZIDA, S. I.; LIN, Y. DER.; KHUNG, Y. L. Current Trends on Surface Acoustic Wave Biosensors. **Adv Mater Technol**, v. 6, p. 1–23, 2021.

70   GALLAGHER, M.; MALOCHA, D. C. **Wireless SAW Sensors Having Integrated Antennas.** US20120174678A1, 2015.

71   CUI, L. *et al.* Radio Frequency Identification and Sensing Techniques and Their Applications—A Review of the State-of-the-art. **Sensors**, v. 19, p. 4012, 2019.

72   ZHANG, J. *et al.* A Review of Passive RFID Tag Antenna-based Sensors and Systems for Structural Health Monitoring Applications. **Sensors**, v. 17, p. 265, 2017.

73   GALLAGHER, M. W.; SMITH, W. C.; MALOCHA, D. C. An Integrated SAW Sensor with Direct Write Antenna. **In: 2013 Joint European Frequency and Time Forum & International Frequency Control Symposium (EFTF/IFC).** IEEE, p. 450–453, 2013.

74   GALLAGHER MW, SANTOS BC, MALOCHA DC. Wireless Wideband SAW Sensor-antenna design. In: **2010 IEEE International Frequency Control Symposium.** IEEE, p. 291–296, 2010.

75   DAI X, FANG L, ZHANG C, SUN H. Design of a Novel Passive Wireless Integrated SAW-based Antenna Sensor for Structural Health Monitoring. **J Sens,** v. 2020, p. 1–9., 2020

76   BOLDEIU, G. *et al.* Investigation of Temperature Sensing Capabilities of GaN/SiC and GaN/Sapphire Surface Acoustic Wave Devices. **IEEE Access**, v. 10, p. 741–752, 2022.

77   TANG, H. *et al.* Recent Advances in 2D/Nanostructured Metal Sulfide-based Gas Sensors: Mechanisms, Applications, and Perspectives. **J Mater Chem A Mater**, v. 8, p. 24943–24976, 2020.

78   HAQ, B. U. *et al.* Structural, Electronic, and Optical Properties of the Pressure-Driven Novel Polymorphs of Gallium Nitride: First-principles Investigations. **Int J Energy Res**, v. 46, p. 2361–2372, 2022.

79   FURQAN, C. M.; HO, J. Y. L.; KWOK, H. S. GaN Thin Film: Growth and Characterizations by Magnetron Sputtering. **Surfaces and Interfaces**, v. 26, p. 101364, 2021.

80   LEE, S. H. *et al.* Epitaxially Grown GaN Thin-film SAW Filter with High Velocity and Low Insertion Loss. **IEEE Trans Electron Devices**, v. 48, p. 524–529, 2001.

81   CIPLYS, D. *et al.* Visible-blind Photoresponse of GaN-based Surface Acoustic Wave Oscillator. **Appl Phys Lett,** v. 80, 2020–2022, 2002.

82   CHIVUKULA, V. S. *et al.* Impact of Photocapacitance on Phase Response of GaN/Sapphire SAW UV Sensor. **IEEE Sens J**, v. 10, p. 883–887, 2010.

83   RÝGER, I. *et al.* GaN/SiC Based Surface Acoustic Wave Structures for Hydrogen Sensors with Enhanced Sensitivity. **Sens Actuators A Phys**, v. 227, p. 55–62, 2015.

84   JAAFAR, M. M. *et al.* Surface Acoustic Wave Propagation of GaN/Sapphire Integrated with a Gold Guiding Layer. **Sensors**, v. 23, 2023.

85   CHANG, Y. C.; CHEN, Y. C.; CHENG, C. C. Fabrication of AlGaN High Frequency Bulk Acoustic Resonator by Reactive RF Magnetron Co-Sputtering System. **Materials**, v. 14, 2021.

86   RÖNNBY, K.; PEDERSEN, H.; OJAMAË, L. Surface Structures from NH_3 Chemisorption in CVD and ALD of AlN, GaN, and InN Films. **Journal of Physical Chemistry C**, v. 126, p. 5885–5895, 2022.

87   ZHANG, G. *et al.* Subnanometer-thick 2D Gan Film with a Large Bandgap Synthesized by Plasma Enhanced Chemical Vapor Deposition. **J Mater Chem A Mater**, v. 10, p. 4053–4059, 2022.

88   PANT, R. *et al.* In-Plane Anisotropic Photoconduction in Nonpolar Epitaxial a-Plane GaN. **ACS Appl Mater Interfaces**, v. 10, p. 16918–16923, 2018.

89   JONES, A. C.; WHITEHOUSE, C. R.; ROBERTS, J. S. Chemical Approaches to the Metalorganic CVD of Group-III Nitrides. **Chemical Vapor Deposition**, v. 1, p. 65–74, 1995.

90   ALLEN, M. J.; TUNG, V. C.; KANER, R. B. Honeycomb Carbon: a Review of Graphene. **Chem Rev**, v. 110, p. 132–145, 2010.

91   MIŠEIKIS, V. *et al.* Acoustic Streaming of Microparticles Using Graphene-based Interdigital Transducers. **Nanotechnology**, v. 32, 2021.

92   GÜLER, Ö.; BAĞCI, N. A Short Review on Mechanical Properties of Graphene Reinforced Metal Matrix Composites. **Journal of Materials Research and Technology**, v. 9, p. 6808–6833, 2020.

93   GOYAL, D. *et al.* Graphene: A Two Dimensional Super Material for Sensor Applications. **Mater Today Proc**, v. 43, p. 203–208, 2021.

94   SU, Y. *et al.* Surface Acoustic Wave Humidity Sensor Based on Three-Dimensional Architecture Graphene/PVA/SiO_2 and its Application for Respiration Monitoring. **Sens Actuators B Chem**, v. 308, p. 127693, 2020.

95   YAN, X.; LI, B.; LI, L. Colloidal Graphene Quantum Dots with Well-defined Structures. **Acc Chem Res**, v. 46, p. 2254–2262, 2013.

96   LI, C.; SHI, G. Three-dimensional Graphene Architectures. **Nanoscale**, v. 4, p. 5549–5563, 2012.

97   WU, J. *et al.* Ultrathin Glass-based Flexible, Transparent, and Ultrasensitive Surface Acoustic Wave Humidity Sensor with ZnO Nanowires and Graphene Quantum Dots. **ACS Appl Mater Interfaces**, v. 12, p. 39817–39825, 2020.

98   MISEIKIS, V. *et al.* Acoustically Induced Current Flow in Graphene. **Appl Phys Lett**, v. 100, p. 133105, 2012.

99   POOLE, T.; NASH, G. R. Acoustoelectric Current in Graphene Nanoribbons. **Sci Rep**, v. 7, p.1767, 2017.

100   JI, J. *et al.* An Aptamer-Based Shear Horizontal Surface Acoustic Wave Biosensor with a CVD-grown Single-layered Graphene Film for High-sensitivity Detection of a Label-free Endotoxin. **Microsyst Nanoeng**, v. 6, 2020.

101   ZAVYALOVA, E.; KOPYLOV, A. DNA Aptamer-Based Molecular Nanoconstructions and Nanodevices for Diagnostics and Therapy. **In: Nanostructures for the Engineering of Cells, Tissues and Organs.** Elsevier, p. 249–290, 2018.

102   JI, J. *et al.* Single-Layered Graphene/Au-nanoparticles-based Love Wave Biosensor for Highly Sensitive and Specific Detection of Staphylococcus aureus Gene Sequences. **ACS Appl Mater Interfaces**, v. 12, p. 12417–12425, 2020.

103   YIN, C. *et al.* Enhancing the Sensitivity of Flexible Acoustic Wave Ultraviolet Photodetector with Graphene-quantum-dots Decorated ZnO Nanowires. **Sens Actuators A Phys**, v. 321, p. 112590, 2021.

104   WEI, T. *et al.* Nonvolatile Organic Resistive Switching Memory Based on Poly(o-methoxyaniline) Film. **Microelectron Eng**, v. 162, p. 85–88, 2016.

105   KANG, S. *et al.* Review of Conjugated Polymer Nanoparticles: from Formulation to Applications. **ACS Appl Nano Mater**, v. 5, p. 17436–17460, 2022.

106   HU, C. *et al.* Synthesis and Characterization of a Poly(o-anisidine)-SiC Composite and its Application for Corrosion Protection of Steel. **RSC Adv**, v. 7, p. 11732–11742, 2017.

107   PASSADOR, F. R. *et al.* Thermal, Mechanical and Electromagnetic Properties of LLDPE/PANI Composites. **Polymer Bulletin**, v. 74, p. 2701–2717, 2017.

108   CHRISTINELLI, W. A. *et al.* High-Performance Energy Storage of Poly (o-methoxyaniline) Film Using an Ionic Liquid as Electrolyte. **Energy**, v. 14, p. 1829–1835, 2017.

109 BISCARO, R. S.; REZENDE, M. C.; FAEZ, R. Influence of Doped Polyaniline on the Interaction of PU/PANI Blends and on its Microwave Absorption Properties. **Polym Adv Technol,** v. 19, p. 151–158, 2008.

110 ALESARY, H. F. *et al.* A Comparative Study of the Effect of Organic Dopant Ions on the Electrochemical and Chemical Synthesis of the Conducting Polymers Polyaniline, Poly(o-toluidine) And Poly(o-methoxyaniline). **Chemical Papers**, v. 75, p. 5087–5101, 2021.

111 PINTO, S. DE S.; REZENDE, M. C. Morphological, Electromagnetic, and Absorbing Properties of POMA and PANI/Carbon Black Composites. **J Electron Mater**, v. 46, p. 4939–4947, 2017.

112 BIONDO, M. M. *et al.* Chemically Synthesized Poly(o-methoxyaniline): Influence of Counterions on the Structural and Electrical Properties**. J Mol Struct,** v. 1205, 2020.

113 BIANCHI, R. F.; ONMORI, R. K.; FARIA, R. M. Device Model for Poly(o-methoxyaniline) Field-Effect Transistor. **J Polym Sci B Polym Phys**, v. 43, p. 74–78, 2005.

114 YU, Y. H. *et al.* Covalent Bond–grafted Soluble Poly(o-methoxyaniline)-Graphene Oxide Composite Materials Fabricated as Counter Electrodes of Dye-Sensitised Solar Cells. **Org Electron**, v. 42, p. 209–220, 2017.

115 TSAI, C. H. *et al.* Poly(o-methoxyaniline) Doped with an Organic Acid as Cost-Efficient Counter Electrodes for Dye-sensitized Solar Cells. **Electrochim Acta**, v. 213, p. 791–801, 2016.

116 LINDINO, C. A. *et al*. Poly(o-methoxyaniline) Modified Electrode for Detection of Lithium Ions. **Quim. Nova**, v. 35, p. 449-453, 2012.

117 WANG, W.; XIE, X.; HE, S. Optimal Design of a Polyaniline-coated Surface Acoustic Wave Based Humidity Sensor. **Sensors (Switzerland)**, v. 12, p. 16816–16828, 2013.

118 MEMON, M. M. *et al.* Surface Acoustic Wave Humidity Sensor Based on Hydrophobic Polymer Film. **J Electron Mater**, v. 51, p. 5627–5634, 2022.

119 PRABAKARAN, K. *et al.* A Highly Sensitive Surface Acoustic Wave Sensor Modified with Molecularly Imprinted Hydrophilic PVDF for the Selective Amino Acid Detection. **Sens Actuators A Phys**, v. 341, 2022.

120 WANG, B.; ZHOU, L.; WANG, X. Surface Acoustic Wave Sensor for Formaldehyde Gas Detection Using the Multi-Source Spray-Deposited Graphene/PMMA Composite Film. **Front Mater**, v. 9, 2023.

121 DEPLA, D.; Mahieu, S. Reactive Sputter Deposition. **Springer**, 2008.

122   SMITH, D. L. Thin-film Deposition: Principles and Practice. **McGraw-Hill**, 1995.

123   CHANG, Y. C. *et al.* Improved Frequency Response of the 3.5 GHz SMR Devices using Ga-doped AlN Thin Films as the Piezoelectric Layers. **Modern Physics Letters B**, v. 36, 2022.

124   NICOLOIU, A. *et al.* The Behavior of Gold Metallized AlN/Si- And AlN/Glass-Based SAW Structures as Temperature Sensors. **IEEE Trans Ultrason Ferroelectr Freq Control**, v. 68, p. 1938–1948, 2021.

125   OLIVEIRA, R. S. *et al.* Structural, Morphological, Vibrational and Optical Properties of GaN Films Grown by Reactive Sputtering: The Effect of RF Power at Low Working Pressure Limit. **Materials Research**, v. 25, 2022.

126   SHANG, L. *et al.* The Surface Morphology Evolution of GaN Nucleation Layer During Annealing and its Influence on the Crystal Quality of GaN Films. **Coatings,** v. 11, p. 1-8, 2021.

127   KERBER, S. J. *et al.* The Complementary Nature of X-Ray Photoelectron Spectroscopy and Angle-Resolved X-Ray Diffraction Part I: Background and Theory. **Journal of Materials Engineering and Performance**, v.7, p. 329-333, 1998.

128   SHEN, K-C. *et al.* Pulsed Laser Deposition of Hexagonal GaN-on-Si(100) Template for MOCVD Applications. **Opt Express**, v. 21, p. 26468, 2013.

129   QIN, H. et al. Mechanical, Thermodynamic and Electronic Properties of Wurtzite and Zinc-blende GaN Crystals. **Materials**, v. 10, 2017.

130   LV, H. *et al.* Bulk GaN-based SAW Resonators with High Quality Factors for Wireless Temperature Sensor. **Journal of Semiconductors**, p. 43, 2022.

131   KUMAR, P. *et al.* Magnetic Field Tunable Ferromagnetic Shape Memory Alloy-Based SAW Resonator. **IEEE Electron Device Letters**, v. 43, p. 446–449, 2022.

132   WIERZBICKA, A. *et al.* Arrangement of GaN Nanowires on Si(001) Substrates Studied by X-ray Diffraction: Importance of Silicon Nitride Interlayer. **Appl Surf Sci**, v. 425, p. 1014–1019, 2017.

133   BAE, S. Y. *et al.* III-nitride Core-shell Nanorod Array on Quartz Substrates. **Sci Rep**, v. 7, 2017.

134   WIERZBICKA, A. *et al.* Influence of Substrate Nitridation Temperature on Epitaxial Alignment of GaN Nanowires to Si(111) Substrate. **Nanotechnology,** 2013.

135   BAE, S. Y. *et al.* Selective-area Growth of Vertically Oriented GaN Nanostructures with a Hafnium Pre-orienting Layer. **J Cryst Growth**, v. 468, p. 110–113, 2017.

136 FU, Y. Q. *et al.* Engineering Inclined Orientations of Piezoelectric Films for Integrated Acoustofluidics and Lab-on-a-chip Operated in Liquid Environments. **Lab Chip**, v. 21, p. 254–271, 2021.

137 DRIFT, A. V. DER. Evolutionary Selection, a Principle Governing Growth Orientation in Vapour-deposited Layers. **Philips Res. Rep.**, 1967.

138 ZENG, Y. *et al.* Raman Analysis of E_2 (High) and A_1 (LO) Phonon to the Stress-free GaN Grown on Sputtered AlN/Graphene Buffer Layer. **Applied Sciences (Switzerland),** v. 10, p. 1–12, 2020.

139 KUBALL, M. Raman Spectroscopy of GaN, AlGaN and AlN for Process and Growth Monitoring/Control. **Surface and Interface Analysis,** v. 31, p. 987–999, 2001.

140 HARIMA, H. Properties of GaN and Related Compounds Studied by means of Raman Scattering. **Journal of Physics: Condensed Matter**, v. 14, p. R967–R993, 2002.

141 CHUAH, L. S.; HASSAN, Z.; HASSAN, H. A. Optical Characterization of GaN Thin Film Grown on Si(111) by Radio-frequency Plasma-assisted Molecular Beam Epitaxy. **In: Proceeding Of Malaysia-Japan International Symposium On Advanced Technology.** 1989.

142 HAO, J. *et al.* PL Tunable GaN Nanoparticles Synthesis through Femtosecond Pulsed Laser Ablation in Different Environments. **Nanomaterials**, v. 10, 2020.

143 RODRÍGUEZ-MADRID, J. G. et al. Super-high-frequency SAW Resonators on AlN/diamond. **IEEE Electron Device Letters**, v. 33, p. 495–497, 2012.

144 WANG, L.; WANG, H. Analysis of Propagation Characteristics of AlN/diamond/Si Layered SAW Resonator. **Microsystem Technologies**, v. 26, p. 1273–1283, 2020.

145 KIM, S. K. *et al.* Investigation of Characteristics of SAW Filter using Undoped GaN Epitaxial Layer Grown by MOCVD on Sapphire Substrate. **Proceedings of the IEEE Ultrasonics Symposium**, v. 1, p. 257–260, 2001.

146 ZHANG, D. *et al.* Influence of N_2 Flux on the Improvement of Highly *c*-oriented GaN Films on Diamond Substrates. **Vacuum,** v. 85, p. 725–729, 2011.

147 LEITE, D. M. G. *et al.* Columnar Microstructure of Nanocrystalline $Ga_{1-x}Mn_xN$ Films Deposited by Reactive Sputtering. **J Cryst Growth,** v. 327, p. 209–214, 2011.

148 VAUCHE, L. *et al.* Study of an Al_2O_3/GaN Interface for Normally off MOS-Channel High-electron-mobility Transistors using XPS Characterization: the Impact of Wet Surface Treatment on Threshold Voltage VTH. **ACS Appl Electron Mater**, v. 3, p. 1170–1177, 2021.

149 SANKARANARAYANAN, S. *et al.* Fabrication of Gallium Nitride and Nitrogen Doped Single Layer Graphene Hybrid Heterostructures for High Performance Photodetectors. **Sci Rep**, v. 10, 2020.

150 MISHRA, M. *et al.* Pit Assisted Oxygen Chemisorption on GaN Surfaces. **Physical Chemistry Chemical Physics**, v. 17, p. 15201–15208, 2015.

151 KIM, K. *et al.* Co-doping Characteristics of Si and Zn with Mg in P-type GaN. **MRS Internet Journal of Nitride Semiconductor Research**, v. 5, p. 322-328, 2020.

152 JANG, J-S. Ohmic Contacts to p-type GaN Using a Ni/Pt/Au Metallization Scheme. **Journal of Vacuum Science & Technology B: Microelectronics and Nanometer Structures**, v. 16, p. 3105, 1998.

153 HSIAO, W. H. *et al.* Investigations on the cosputtered ITO-ZnO transparent electrode ohmic contacts to n-GaN. **Applied Sciences (Switzerland)**, v. 6, 2016.

154 JAIN, S. K. *et al.* Impact of Thermal Oxidation on the Electrical Transport and Chemical & Electronic Structure of the GaN Film Grown on Si and Sapphire Substrates. **Applied Surface Science Advances**, v. 5, 2021.

155 MONISH, M. *et al.* Gallium Nitride Films of High n-Type Conductivity Grown by Reactive Sputtering. **Semicond Sci Technol**, v. 35, p. 045011, 2020.

156 JI, X. *et al.* Fabrication and Characterization of One-port Surface Acoustic Wave Resonators on Semi-insulating GaN Substrates. **Chinese Physics B**, v. 28, 2019.

157 DAMASCENO, B. S. *et al.* Flash Graphene and Poly(o-methoxy aniline) for the Composition of a Solvent-based Conductive Ink. **Surfaces and Interfaces,** p. 104427, 2024.

158 WYSS, K. M.; LUONG, D. X.; TOUR, J. M. Large-Scale Syntheses of 2D Materials: Flash Joule Heating and other Methods. **Advanced Materials**, v. 34, 2022.

159 ALGOZEEB, W. A. *et al.* Flash Graphene from Plastic Waste. **ACS Nano**, v. 14, p. 15595–15604, 2020.

160 CHEN, W. *et al.* Heteroatom-doped Flash Graphene. **ACS Nano**, v. 16, p. 6646–6656, 2022.

161 DENG, B. *et al.* Phase Controlled Synthesis of Transition Metal Carbide Nanocrystals by Ultrafast Flash Joule Heating. **Nat Commun**, v. 13, 2022.

162 LUONG, D. X. *et al.* Gram-scale Bottom-up Flash Graphene Synthesis. **Nature**, v. 577, p. 647–651, 2020.

163 WYSS, K. M. *et al.* Synthesis of Clean Hydrogen Gas from Waste Plastic at Zero Net Cost. **Advanced Materials**, v. 35, 2023.

164 FERRARI, A. C. Raman Spectroscopy of Graphene and Graphite: Disorder, Electron-phonon Coupling, Doping and Nonadiabatic Effects. **Solid State Commun**, v. 143, p. 47–57, 2007.

165 KUMAR, K. V. *et al.* Exfoliation of Graphite to Turbostratic Graphene. **2D Mater**, v. 11, 2024.

166 BECKHAM, J. L. *et al.* Machine Learning Guided Synthesis of Flash Graphene. **Advanced Materials**, v. 34, 2022.

167 WYSS, K. M. *et al.* Converting Plastic Waste Pyrolysis Ash into Flash Graphene. **Carbon,** v. 174, p. 430–438, 2021.

168 ADVINCULA, P. A. *et al.* Flash Graphene from Rubber Waste. **Carbon**, v. 178, p. 649–656, 221.

169 XU, Y. *et al.* Liquid-Phase Exfoliation of Graphene: an Overview on Exfoliation Media, Techniques, and Challenges. **Nanomaterials**, v. 8, p. 942, 2018.

170 SHALLCROSS, S. *et al.* Electronic Structure of Turbostratic Graphene. **Phys Rev B**, v. 81, p. 165105, 2010.

171 NEGISHI, R. *et al.* Turbostratic Stacking Effect in Multilayer Graphene on the Electrical Transport Properties. **Physica Status Solidi (B)**, p. 257, 2020.

172 GARLOW, J. A. *et al.* Large-Area Growth of Turbostratic Graphene on Ni(111) via Physical Vapor Deposition. **Sci Rep**, v. 6, p. 19804, 2016.

173 CAO, Y. *et al.* Unconventional Superconductivity in Magic-angle Graphene Superlattices. **Nature**, v. 556, p. 43–50, 2018.

174 JEONG, H. K. *et al.* Evidence of Graphitic AB Stacking order of Graphite Oxides. **J Am Chem Soc**, v. 130 p. 1362–1366, 2008.

175 CHEN, W. *et al.* Ultrafast and Controllable Phase Evolution by Flash Joule Heating. **ACS Nano**, v. 15, p. 11158–11167, 2021.

176 SZKLARCZYK, M. *et al.* Electrochemical and in situ TM-AFM Studies of the Polymerization Conditions on Poly(o-methoxyaniline) Film Morphology. **Electrochim Acta**, v. 51, p. 1036–1043, 2005.

177 da SILVA, J. M. S. *et al.* Poly(o-methoxyaniline) Chain Degradation Based on a Heat Treatment (HT) Process: Combined Experimental and Theoretical Evaluation. **Molecules**, v. 27, p. 3693, 2022.

178   CHRISTINELLI, W. AP.; TRENCH, A. B.; PEREIRA, E. C. Electrochromic Properties of Poly(o-methoxyaniline)-poly(3-thiophene acetic acid) Layer by Layer Films. **Solar Energy Materials and Solar Cells**, v. 157, p. 703-708, 2016.

179   da SILVA, J. P. *et al.* Poly(o-methoxyaniline) Modified by the Biphasic Ceramic System $Na_2Ti_3O_7$/$Na_2Ti_6O_{13}$. **J Inorg Organomet Polym Mater**, v. 33, p. 1381-1387, 2023.

180   SANCHES, E. A. *et al.* Structural and Morphological Characterization of Chloride Salt of Conducting Poly(o-methoxyaniline) obtained at Different Time Synthesis. **J Mol Struct**, v.1039, p. 167-173, 2013.

181   JAMAL, R. *et al.* Comparative Atudies of Solid-state Synthesized Poly(o-methoxyaniline) Doped with Organic Sulfonic Acids. **Journal of Polymer Research,** v. 15, p. 75-82, 2008.

182   PIMPIN, A.; SRITURAVANICH, W. Reviews on Micro- and Nanolithography Techniques and their Applications. **Engineering Journal,** v. 16, p. 37-55, 2012.

183   ALTISSIMO, M. E-beam Lithography for Micro-/nanofabrication. **Biomicrofluidics**, v. 4, 2010.

FOLHA DE REGISTRO DO DOCUMENTO

1. CLASSIFICAÇÃO/TIPO	2. DATA	3. REGISTRO N°	4. N° DE PÁGINAS
TD	17 de junho de 2024	DCTA/ITA/TD-019/2024	110

5. TÍTULO E SUBTÍTULO:

Fabrication graphene enhanced GaN for surface acoustic waves sensor applications

6. AUTOR(ES):

Barbara Souza Damasceno

7. INSTITUIÇÃO(ÕES)/ÓRGÃO(S) INTERNO(S)/DIVISÃO(ÕES):

Instituto Tecnológico de Aeronáutica - ITA

8. PALAVRAS-CHAVE SUGERIDAS PELO AUTOR:

1. Heterostructure. 2. Gallium nitride. 3. Graphene. 4. Poly(o-methoxyaniline). 5. Surface acoustic wave device.

9.PALAVRAS-CHAVE RESULTANTES DE INDEXAÇÃO:

Filmes finos; Nitreto dde gálio; Grafeno; Dispositivos de onda acústica superficial; Tratamento de superfície; Física de plasmas; Física.

10. APRESENTAÇÃO: (X) Nacional ( ) Internacional

ITA, São José dos Campos. Curso de Doutorado. Programa de Pós-Graduação em Engenharia Aeronáutica e Mecânica. Área de Materiais, Manufatura e Automação. Orientador: Prof. Dr. Douglas Marcel Gonçalves Leite; coorientador: Prof. Dr. André Luis de Jesus Pereira. Defesa em 28/05/2024. Publicada em 2024.

11. RESUMO:

This thesis aims to enable the development of a heterostructure composed of gallium nitride (GaN) thin films and carbon black-derived flash graphene (CBFG) and/or poly(o-methoxyaniline) (POMA), with the intention of utilizing it in sensing applications. This work includes the deposition of GaN thin films through sputtering on Si(100) and glass substrates, the synthesis of CBFG and POMA powders via flash Joule heating (FJH) system and oxidative polymerization, respectively, and the fabrication and optimization of an ink containing CBFG, POMA, or both. In surface acoustic wave (SAW) devices, GaN film can be used as the piezoelectric substrate, and the ink can be applied as the sensing layer in the sensor's active area. The results showed successful deposition of GaN films on Si and glass by sputtering. X-ray diffraction (XRD), Raman spectroscopy measurements, and transmission electron microscopy (TEM) image confirmed that the GaN films are polycrystalline and exhibit wurtzite crystal structure with preferential orientation in the c-direction. The values of H/λ (thickness/wavelength) obtained using the thickness measured by scanning electron microscopy (SEM) (2h $\rightarrow$ H = 329 ± 17 nm, λ = 1000 nm $\rightarrow$ H/λ = 0.33 | 4h $\rightarrow$ H = 569 ± 30 nm, λ = 1000 nm $\rightarrow$ H/λ = 0.57 | 6h $\rightarrow$ H = 1162 ± 36 nm, λ = 1000 nm $\rightarrow$ H/λ = 1.16) showed that the GaN sample grown for 6 hours, even though exhibiting a high root mean square (RMS) roughness measured by atomic force microscopy (AFM), should still demonstrate the best performance in SAW applications. An ohmic contact between the interdigitated transducers (IDTs) and GaN film was observed, which is beneficial for SAW device applications. SAW devices were produced and optimized using the deposited GaN on Si films. Pure turbostratic CBFG was successfully synthesized using the FJH system, as confirmed by XRD, SEM, and TEM images. Porosimetry analysis showed CBFG's surface area around 293 m² g⁻¹. As a result, CBFG proved to be a promising adsorbent for methylene blue (MB) removal, which is an intriguing property for enhancing the sensitivity of the device. POMA was successfully synthesized through oxidative polymerization, as supported by XRD and XPS results. Fourier transform infrared spectroscopy (FTIR) data showed amine and imine units on the polymer chain of POMA, consistent with XPS analysis. SEM images depicted material with a globular morphology, while the porosimetry presented a surface area around 4 m² g⁻¹. Despite its low surface area in comparison to CBFG, POMA remains a potential material for composing a conductive ink due to its chemical surface, and dispersibility, facilitating the ink production process and retaining the electron conductivity (EC) properties. CBFG and POMA powders were combined in various ratios to form an ink with suitable EC. The highest EC value of 0.768 S m⁻¹ was achieved using concentrations of 40.0 mg L⁻¹ CBFG, 2.0 mg L⁻¹ POMA, and 4.0 mg L⁻¹ binder. This result suggests that the ink can be effectively utilized as a sensing layer in the active area of a SAW device.

12. GRAU DE SIGILO:

(X) OSTENSIVO ( ) RESERVADO ( ) SECRETO